MONTAN UNIVERSITÄT
WWW.UNILEOBEN.AC.AT

Chair of Materials Physics

Master's Thesis

Synchrotron-Based Characterization of Bulk Metallic Glasses

David Rovira Ferrer

May 2023

MONTANUNIVERSITÄT LEOBEN
www.unileoben.ac.at

AFFIDAVIT

I declare on oath that I wrote this thesis independently, did not use other than the specified sources and aids, and did not otherwise use any unauthorized aids.

I declare that I have read, understood, and complied with the guidelines of the senate of the Montanuniversität Leoben for "Good Scientific Practice".

Furthermore, I declare that the electronic and printed version of the submitted thesis are identical, both, formally and with regard to content.

Date 30.05.2023

Signature Author
David Rovira Ferrer

Contents

1. Introduction

Understanding the world around us has always been a concern of mankind. The philosophy of matter initiated the search for the description and behaviour of reality with some of its greatest thinkers in ancient Greece. Aristotle's work in "Metaphysics", which separates substance from properties, strongly dominated the concept of reality right up to the Modern Age. Over the years, philosophy and science diverged in their frameworks and methods, but both still share the same driving force. Contributing to the growth of science is working towards the increasing unity of humanity, towards the description of the common space that we occupy and that at the same time constitutes us.

There is a clear link between modern crystallography and Democritus' assumption that matter consists of atoms and Pythagoras' perception of nature in a harmonic way through numbers and geometry. R.J. Haüy, W.H. Miller and A. Bravais lay the foundations for the structural description of crystalline solids (1). This exact prediction of the atomic arrangement in a crystal allows a good understanding of its properties and behaviour.

However, this perfect relationship between atomic planes by means of whole number ratios fails to explain the second large family of solids: the amorphous state. With the development of urban societies in Egypt and Mesopotamia, and the mastery of furnaces capable of reaching 1000 ºC (2), amorphous materials began their role in human history. Since then, their technological importance has continued to grow, from window and tableware glass to, more recently, amorphous semiconductors (3,4) and metallic glasses (5). The development and diversification of new production techniques is what enabled this technological growth. The high increase in cooling rates from the liquid melt, or the invention of bottom-up techniques such as vapour deposition or sputtering, made it easier to obtain amorphous phases in materials like metals that are typically crystalline.

Despite its long history, the full knowledge of the amorphous state remains unclear. The random distribution of its atomic arrangement clashes with the fractional representation of crystalline solids and requires the use of a more probabilistic approach. During the 1960s, JD Bernal and GD Scott laid the

foundations for modern research into the way atoms are arranged (6,7). Various approaches have been proposed to describe liquid-solid and glass transitions, such as the density wave approach of T.V. Ramakrishnan (8) or the Potential Energy Landscape (PEL) of J.H. Gibbs and E.A. DiMarzio (9). DeGiuli's Field Theory (10) and the Free Volume Model (11,12) emerged to explain the fluctuating state of the glass and its mechanical properties.

However, there is still a lot of work to be done to achieve a complete and unified picture of the amorphous state. In this sense, recognising the relationship between structure and properties is crucial to tailoring their functionalities and ensuring the correct performance of devices. In-situ characterization can play a key role in this goal. Compared to ex-situ measurements, where only a static image of the final glassy state is obtained after a thermal or stress history, in-situ allows the evolution of the system to be followed. By recording the physical state of the glass during temperature programmes or load application, the mechanisms behind its relaxation and crystallisation kinetics can be identified. The result will be the determination of their macroscopic properties.

X-ray diffraction (XRD) is one of the most powerful tools to study structural phase transformations in solids and liquids (13). In order to obtain beams that retain sufficient intensity after diffraction with the metallic samples and that have a high spatial resolution to detect microscopic heterogeneities, synchrotron X-rays are required (14,15). However, the radiation properties that allow a good characterisation of the amorphous material can also change it. Observation requires the sample to interact with the stimuli. When using these high-energy and collimated X-rays, it is possible that they modify the glassy state kinetics.

In this thesis, a master alloy of $Pt_{57.5}Cu_{14.7}Ni_{5.3}P_{22.5}$ was prepared by suction-casting under a vacuum atmosphere. In-situ and ex-situ characterizations were conducted at a synchrotron facility. Fast Differential Scanning Calorimetry (FDSC) was used to produce Continuous Heating Transformation (CHT) diagrams to compare the thermal transitions taking place in both conditions. This work aims to provide a better understanding of the synchrotron X-ray diffraction (SXRD) effect on bulk metallic glasses through the study of phase crystallisation during scanning calorimetry.

2. Theoretical Foundations

2.1. First insight into metallic glasses

In nature, metals display an ordered and translational crystalline structure consisting of a discrete lattice of points translated by a set of vectors. They can therefore be regarded as a periodic repetition of a unitary packing structure. W.H. Miller, A. Bravais and A. Schönflies laid the foundations for today's well-studied and comprehended crystallography theory (1).

However, a new family of materials was catalogued in the 1960s when Duwez synthesised an Au-Si alloy with no observable crystallinity (16). This was referred to as "metallic glass" and no sharp peaks were detected in its X-ray diffraction (XRD) pattern, but rather a broad and diffuse peak. This signal is characteristic of amorphous materials and is referred to as "amorphous halo".

Freezing the liquid structure of the molten metal through a rapid solidification rate (around $-10^6\,K\cdot s^{-1}$) enabled Duwez to achieve the amorphous microstructure. The method behind this high cooling rate was later called "gun technique" and consisted of projecting a small droplet of the molten alloy tangentially onto a conductive copper substrate. The forces acting on the as it encounters the substrate cause it to spread, producing a thin sheet of liquid. This increased contact surface allows the substrate to rapidly extract heat from the liquid, freezing it into an amorphous solid. Pure metals quenched at slow rates experience a sudden decrease in the free volume at the melting (or liquidus) temperature as they fall to the crystalline equilibrium state (Figure 1). For multicomponent alloys, melting often takes place in a range of temperatures (starting from the melting temperature and finishing at the liquidus) due to the formation of several crystalline phases. However, during quenching of alloys susceptible to glass formation, the molten liquid passes to a metastable state and remains in liquid form below its equilibrium melting temperature. In this regime, called "super-cooled liqud" (SCL) state, the volume decrease monotonically with temperature until the atomic mobility is confined and the liquid vitrifies to the glassy state. Here, the slope of the volume change with temperature is reduced. The glass transition temperature (T_g) is defined as the crossing of the liquid and

glassy state. During this transition, a change in the specific heat and viscosity is expected.

As shown in Figure 1, the glass transition temperature depends on the cooling rate. The glassy state is metastable, and its structure depends on the amount of structural relaxation achieved. For high cooling rates, an earlier glass transition will occur, and a less relaxed glass state will be generated. This will have a significant amount of free volume and will eventually relax into the "ideal" glass.

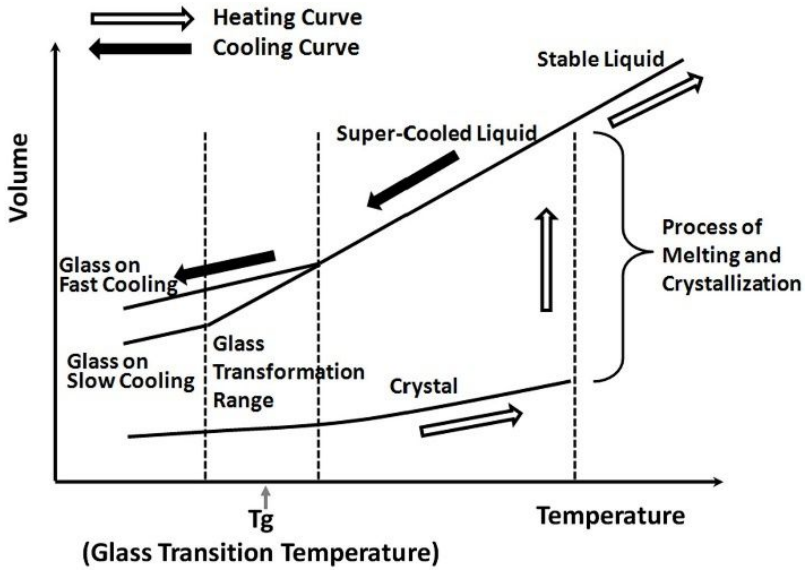

Figure 1. Comparison between volume evolution during glass formation and crystallization (17).

Formally, one should do a distinction between amorphous and glassy materials. The first one refers to any material without crystallinity while the second is more specific. Two conditions must be met for an amorphous solid to be considered a "glass": it must be continuously cooled from the liquid state and, exhibit a glass transition temperature.

Since the discovery of metallic glasses, a large variety of alloys have been found to be susceptible to glass formation. In terms of chemical composition, they can be classified into "metal-metalloid" and "metal-metal". In the first stages of the field, binary alloys with compositions close to the eutectic points such as Ni-Zr (18), Ti-Be (19) or Fe-B (20) systems were mainly reported. Later, multicomponent alloys containing mainly transition metals and metalloids were found to show excellent glass formability (21). This is explained by the greater number of configurational states in the liquid system as the number of

components in the alloy increases. Thus, the entropic part of the Gibbs free energy dominates and stabilise the supercooled liquid in front of the crystalline phase. Through this strategy, low critical cooling rates and samples with bulk sizes (diameters above 1 mm) were achieved. Those systems were named as "bulk metallic glasses" (BMG).

In contrast to crystalline materials, there is no precise topological definition of amorphous materials. They are typically described as a random packing of elements but a theory describing this arrangement of atoms is still missing. However, glasses vary from amorphous solids as they do not lay in the ideal amorphous state. Then, they contain higher amounts of free volume and retain some localized order. A short- and medium-range order is found. For example, in metal-metalloid alloys trigonal prisms are formed due to covalent bonds of the transition metal around the metalloid in the short range. Similarly, Shechtaml et al. reported the existence of a solid possessing long-range order without translational symmetry, "quasicrystals" (22).

2.2. Classical theory of metallic glasses

Over the years, many experimental and simulation studies have been carried out to develop a model for the nature of the glassy state. Although the lack of a simplified model due to the non-ordered arrangement of atoms, two approaches have mainly introduced the basis for understanding the thermodynamics, kinetics, and properties of glasses. The theory proposed by Gibbs – DiMarzio (23) and highly elaborated by Stillinger (24,25) studies the glassy state from a statistical mechanic point of view through the concept of "Potential Energy Landscapes" (PELs). In contrast, Cohen and Turnbull (26,27) introduced the atomistic theory of Free-Volume.

2.2.1. Potential energy landscape (PEL)

The Gibbs-DiMarzio theory postulates that glass formation takes place when the configurational entropy difference between glassy and supercooled liquid state becomes zero. Being the configuration entropy, the term related to the spatial arrangement of atoms and separated from the temperature-dependent vibrational entropy that describes their movement. However, this only apply when thermodynamic equilibrium is achieved in all stages of cooling.

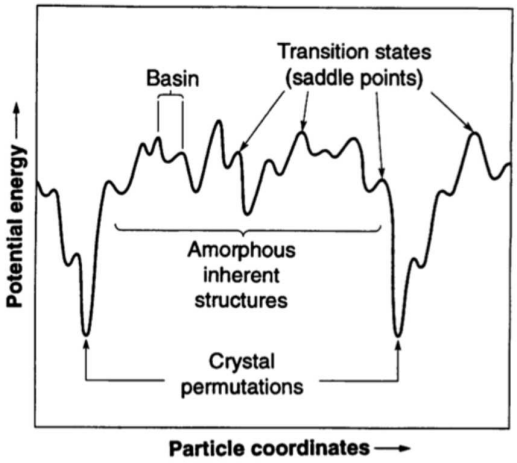

Figure 2. Schematic of the PEL (25)

To know the number of possible configurations in a system during time evolution, one must know the governing interactions between constituent particles. These are determined by the "topographic" view of the potential energy landscape (25). This function depends on the spatial location of each particle and live in a 3N-dimensional space (being N the number of particles in the system) where each point corresponds to one configuration arrangement. Figure 2 shows a simplified representation of the configurational phase space for a glass. Each local minimum in the PEL corresponds to a stable atomic arrangement where every constituent experience null force and torque. These minima are normally called "inherent states" of the PEL. As we can see, there exists a great variety of depths and width for the "valley" surrounding each minima. These domains are referred to as "basin of attraction" and contains those configurations that will evolve to the configuration of the inherent state.

The inherent state in which the system is found depends on the solidification conditions. For high cooling rates, a low relaxed structure freezes and the system encounters on the well's wall of some superficial inherent state. Thus, by temporal evolution the system will fall downhill to the local minima if it is below T_g. And like Gibbs-DiMarzio, Stillinger argued that to reach the ideal glassy state, the system must be allowed to explore the entire PEL. Thus, it is only accessible when sufficiently low cooling rates are employed. However, when annealing above T_g, the thermal energy is enough to produce inter-basin hopping and allows the change of amorphous state (relaxation transitions).

Finally, the total potential of the system obtained from PEL is used in statistical mechanics to determine the different thermodynamic state variables, such as entropy.

2.2.2. Free-Volume model

This model assumes that the behaviour of an amorphous material is governed by the excess space between atoms. It is especially useful in explaining the mechanical properties of metallic glasses, such as their flow curves, but it is less successful in predicting thermodynamic functions.

One can express the free volume, v_f, as:

$$v_f = v - v_c\,, \quad v > v_c \qquad Eq.1$$

being v the volume of the cage formed by the nearest neighbours of the molecule and v_c a critical value, normally approximated to the molecular volume v_m.

Fox and Glory (28–30) were the first to associate the decrease in free volume with the glass transition and sustained it with four simple assumptions:

a) Each molecule has associated a local volume, v.
b) The excess volume when v is above a critical value v_c can be considered as free (Equation 1).
c) Free volume redistribution grows void size until a critical value, v^*, from which molecular transport starts.
d) The abovementioned free volume redistribution occurs without the need to provide free energy.

One can calculate the system's free energy as the summation of each atom subjected to its neighbours' mean potential. This will have two main contributions: the negative work to remove the molecule from its cage and the work to expand the cage in front of the neighbourhood (27). The latter will depend quadratically with the volume until the critical volume is reached and the excess volume reduces the molecule interaction with its neighbours. At that point, the quadratic dependence with volume will decay to a linear one. For a sufficiently dense material, was able to write the system's diffusivity or fluidity in terms of free volume (31):

$$D = D_0\, e^{-\gamma v_m / v_f} \qquad Eq.2$$

Accordingly, system's rigidity is reduced when v_f increases.

2.2.3. Kinetics – Relaxations

Recalling the PEL model, we try to explain in more detail here the transitions between inherent states that govern the kinetics of a glassy system before crystallization events.

Supercooling the liquid phase below the melting temperature, T_m, avoids the fall to the deep crystalline basins and the system remains in the higher amorphous inherent structures (quasi-equilibrium states). However, thermal fluctuations and external perturbations will promote transitions between inherent structures. These transitions can be classified in three categories (25,32):

- Primary relaxation (α). They correspond to irreversible rearrangement of atomic clusters and produce inter-basin hopping in the PEL (Figure 3)
- Secondary relaxation (β). Their rearrangements only involve a reduced number of particles in structural heterogeneities of higher free volume. A substantial location shift of neighbouring atoms take place. In the PEL, these lower energy transitions are represented as intra-basin hopping between shallower local minima within a larger basin.
- Brittle-to-ductile transition (γ or β' relaxation). This transition take place in cryogenic temperatures and are characterized by a homogenous strain (affine) that can promote stress-driven non-affine relaxations such as β. Some authors correlate them to stress inhomogeneities at cryogenic temperatures that relax for low-frequency actuations (33,34).

Therefore, when the system enters the supercooled liquid state, it can switch from one quasi-equilibrium basin to another through α-relaxations. The time between transitions is defined as the mean relaxation time, τ(T), and typically follows the Vogel-Tammann-Fulcher (VTF) equation:

$$\tau(T) = \tau_0 e^{A/(T-T_0)} \qquad Eq.3$$

where A and T_0 are positive constants. An increase in relaxation times is obtained with decreasing temperatures as the distance between the deeper basins in the

PEL widen. Thus, the relaxation time will exceed the experimental time scale at some point and the system will not be able to undergo primary relaxations. However, as β-relaxations only involve localized rearrangements with low activation energies, they remain accessible by thermal fluctuations. This α,β-bifurcation occur at T_g.

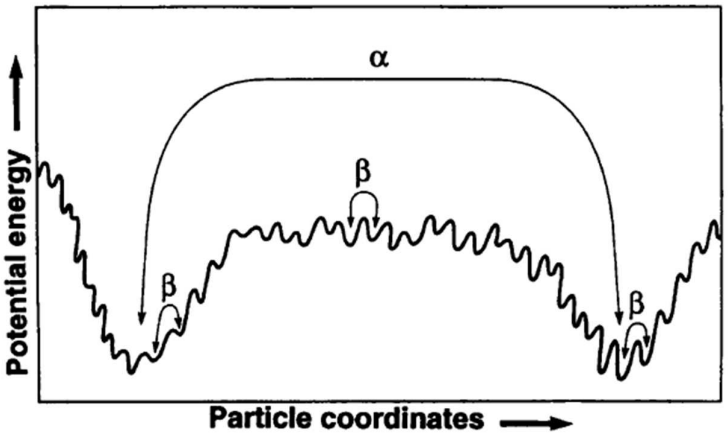

Figure 3. Schematin of α- and β-relaxations in the PEL (25).

2.2.4. Crystallization and Glass Forming Ability (GFA)

The stability of a glassy state is determined by the resistance of the system to crystallize. Therefore, it becomes necessary to have a deep understanding of the nature behind crystallization. Under equilibrium conditions, a crystalline phase forms when its free energy is less than in the glassy configuration. Thus, the driving force for crystallization is the free energy difference between the crystalline phase and the corresponding glass with same composition.

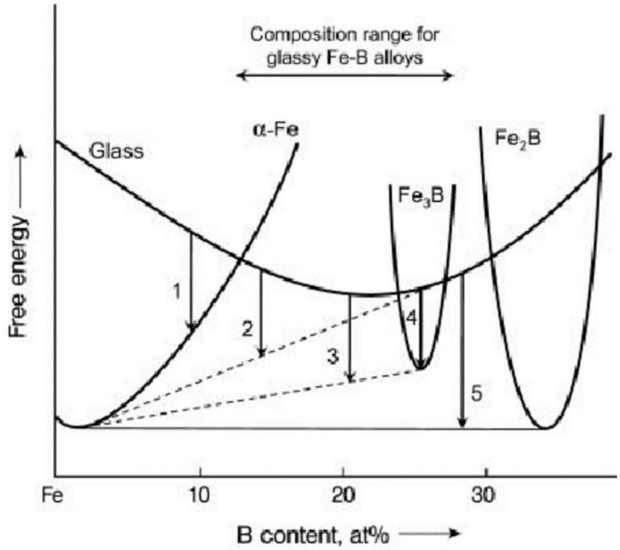

Figure 4. Free energy-composition curves for Fe-B system. Solid tangent line indicates the equilibrium state between ***α-Fe and Fe_2B. Dashed tangent lines indicate metastable equilibriums*** (35).

Three main modes of crystallization can be distinguished depending on whether in the initial stages of decomposition, the phases formed are metastable or equilibrium (35):

- Polymorphous crystallization. This mode is only observed when the composition is near the pure elements or compounds. It consists of the crystallization of a single phase that could be stable, metastable (reaction 4 in Figure 4) or supersaturated (reaction 1 in Figure 4).
- Eutectic crystallization. Two crystalline phases emerge simultaneously from the glassy matrix (reaction 5). In the glass-crystal interface, the two phases separate and leave the surrounding amorphous material with the same composition.
- Primary crystallization. In the first stage of crystallization, a supersaturated solid solution is formed. In order to evolve to the equilibrium state, the crystallite reject solute atoms to the glassy matrix. This process of crystal growth and glass enrichment continues until a metastable equilibrium is reached between both (reaction 2). At the crystallization front a concentration gradient is generated. Thus, to increase the crystal size more atoms must diffuse through the depleted interface. The growth rate will tend to a parabolic behaviour:

$$r = \alpha\sqrt{D \cdot t} \qquad Eq.4$$

being r the radii of a spherical crystal, D the diffusion coefficient, t the annealing time, and α a dimensionless parameter that introduces the dependency on interface and bulk concentrations.

Even though the crystalline phase is more stable in the free energy diagram when temperature falls below T_l, it last long times to crystallize and may require a higher supercooling of the liquid. The introduction of a liquid-solid interface rises the Gibbs free energy of the system, producing the reabsorption of crystallization events if they are too small (i.e., if the surface tension exceeds the energy decrease provided by the new crystalline volume).

The free energy change introduced by the formation of a crystalline cluster in the liquid system will take the next form:

$$\Delta G = -V_s \Delta G_f(T) + A_{LX}\gamma_{LX} \qquad Eq.5$$

being V_s the solid cluster volume, A_{LX} the interface area, γ_{LX} the interfacial energy and ΔG_f the volumetric Gibbs free energy of fusion. For a spherical particle of radius r the above equation becomes:

$$\Delta G = -\frac{4}{3}\pi r^3 \Delta G_f(T) + 4\pi r^2 \gamma_{LX} \qquad Eq.6$$

Thus, an effective nucleus will form when the reduction in free energy due to the formation of a crystalline cluster equalizes the surface tension contribution. In other words, when ΔG experiences a local maximum with r:

$$\frac{d\Delta G}{dr} = 0 \rightarrow r^* = \frac{2\gamma_{LX}}{\Delta G_f(T)} \qquad Eq.7$$

Where r^* is the critical nucleus radius. Considering a small undercooling ($\Delta T < 100\ K$), Turnbull approximation (36) applies and the critical radius can be expressed in terms of ΔT[1]:

$$r^* = \frac{2\gamma_{LX}T_l}{\Delta H_f \Delta T} \qquad Eq.8$$

[1] The difference in Gibbs free energy between the solid and liquid phase is given by $\Delta G = \Delta H - T\Delta S$, with $\Delta H = \Delta H_f - \int_T^{T_l} \Delta C_p dT$ and $\Delta S = \Delta S_f - \int_T^{T_l} \Delta C_p /T\ dT = \frac{\Delta H_f \Delta T}{T_l} - \int_T^{T_l} \Delta C_p /T\ dT$. Where $\Delta T = T_l - T$. Linearly approximating the difference in specific heats between both phases as $\Delta C_p \approx 0$, one gets $\Delta G = \frac{\Delta H_f \Delta T}{T_l}$.

Inserting Equation 8 into Equation 6 one obtains the nucleation activation energy:

$$\Delta G^* = \frac{16\pi {\gamma_{LX}}^3 {T_l}^2}{3{\Delta H_f}^2 \Delta T^2} \qquad Eq.9$$

Using Boltzmann statistics, one can estimate the number of clusters reaching the critical size:

$$n_r^* = n_0 exp\left(\frac{\Delta G^*}{k_B T}\right) \qquad Eq.10$$

being k_B Boltzmann's constant, and n_0 the total number of atoms in the system.

Assuming that the transport of an atom from the liquid to the crystalline cluster requires atomic diffusion and that diffusion depends on the vibration frequency of the atoms, one can use Stokes-Einstein relation:

$$D(T) = \frac{k_B T}{6\pi\eta(T) a_0} \qquad Eq.11$$

where $\eta(T)$ is the viscosity of the liquid and a_0 the average atomic diameter, to obtain the expression for the nucleation rate (37):

$$I_v(T) = \frac{A_v}{\eta(T)} \exp\left(-\frac{16\pi {\gamma_{LX}}^3}{k_B T \Delta {G_f}^2}\right) \qquad Eq.12$$

with A_v being a constant. Thus, more undercooling leads to higher nucleation rates, while it is reduced for higher viscosities. Also, for high surface tensions the nucleation rate will decrease as it is more difficult to reach the critical radius.

Following the nucleation, the velocity at which the crystal-liquid interface advances should be considered. This growth rate, u, can be expressed as:

$$u(T) = \frac{100 f}{\eta}\left[1 - exp\left(-\frac{\Delta T_r \Delta H_f}{RT}\right)\right] \qquad Eq.13$$

Where f is the fraction of sites at the crystal surface where atomic attachment can occur.

For the case in which the nucleation and growth rate are constant with time, the crystallized volume fraction, x, at a time t can be estimated as (38):

$$x = \frac{\pi}{3} I_v(T) u(T)^3 t^4 \qquad Eq.14$$

From this expression, a "time-temperature-transformation" (TTT) *diagram* can be computed (Figure 5). In addition, the critical cooling rate, R_c. to obtain the glassy phase and avoid the nucleation of crystalline phases can be obtained from the TTT diagram by:

$$R_c = \frac{T_l - T_n}{t_n} \qquad Eq.15$$

being T_l the liquidus temperature, T_n and t_n the temperature and time at the nose of the TTT curve (Figure 5). This is called as the "nose method".

It has been observed, however, that the nose method overestimates R_c as it assumes homogeneous crystallization when for most compositions devitrification occurs through a surface crystallization mechanism. At medium cooling rates, nucleation precursors are formed in the glassy matrix. This significantly modifies the critical cooling rate. Schawe and Löffler called these amorphous glasses "self-doped glass" (SDG), whereas the so-called "chemically homogeneous glass" (CHG) has no quenched in nuclei (39). A modified equation for the critical cooling rate, considering the continuous cooling conditions, was proposed by Barandiarán and Colmenero (40):

$$lnR = A - \frac{B}{(T_l - T_{xc})^2} \qquad Eq.16$$

Where R is the cooling rate, A and B are constants, and T_{xc} is the onset solidification temperature of the melt at a cooling rate R. The critical cooling rate will be obtained extrapolating the experimental values fitting to Equation 16.

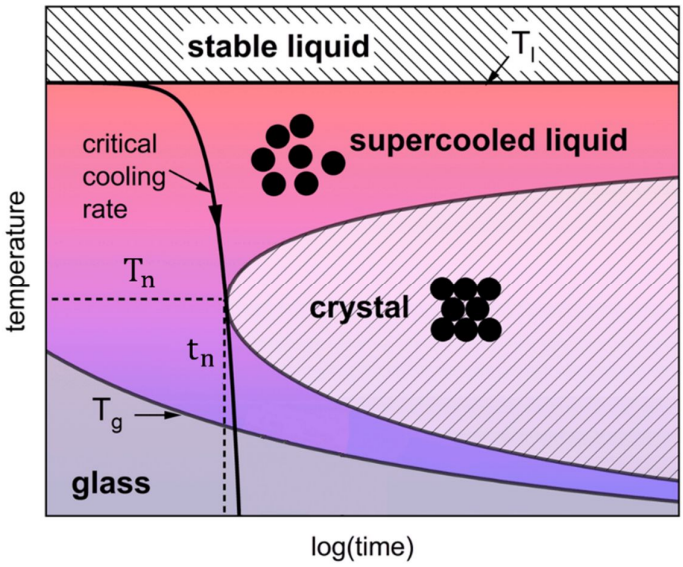

Figure 5. Schematic TTT diagram (41).

As the shape and position of the crystallization nose is determined by the nucleation and growth rates, the "glass forming ability" (GFA) will depend on the viscosity, interfacial energy, and fusion free energy of the alloy. In this sense, liquids with viscosities that increase at fast rates when temperature is reduced will show more stability of the amorphous phase as the long-range atomic rearrangements necessary to crystallize are hindered. Regarding the interfacial energy, it affects the exponential term of the nucleation rate to the power of three. This fact leads to reductions of tens orders of magnitude in $I_v(T)$ with just mJ/m^2 changes in the interfacial energy. Some studies suggest that γ_{LX} is mainly determined by the fusion entropy, ΔS_f, due to the densely packed structures in the solid-liquid interface.

Increasing ΔS_f will simultaneously reduce the driving force for crystallization (ΔG_f) and increase the interfacial energy, shifting the crystallization nose to longer times (high GFA). The main strategy to obtain such increases in ΔS_f is to involve high number of components in the alloy, explaining why bulk metallic glasses are typically multicomponent systems (42).

Many criteria have been proposed to experimentally estimate the GFA by means of thermal transitions, without involving the performance of many experiments at different cooling rates. One of the most widely employed criteria is the reduced glass transition temperature (T_{rg}). Proposed by Turnbull, the ratio between the glass transition temperature, T_g, and the liquidus temperature of the alloy, T_l, is a good indicator of GFA (43). The reason behind this selection is that T_{rg} highly correlate with the alloy's viscosity. The higher the T_{rg}, the higher the viscosity and the better the GFA. For T_{rg} values greater than 2/3, Turnbull predicted the suppression of homogeneous nucleation.

Following the T_{rg} criterion, lowering the liquidus temperature should improve the GFA of the alloy. Therefore, systems that show deep eutectic reactions where the liquidus curve is below the melting points of the individual components would be good forming alloys.

Differently, Egami and Waseda (44) proposed a topological criterion based on lattice strain. By alloying, crystal lattice strains are introduced, and the systems

destabilize. In a glassy phase the total strain energy and local stress fluctuations appear to be practically independent of the solute concentration. However, for solid solution a linear relation between strain energy and solute concentration was obtained. Egami and Waseda suggested that a critical concentration exist in which the glassy phase becomes energetically more favourable than the crystalline one. In binary solutions, this critical concentration, C_B^{min}, was found to be inversely proportional to the atomic mismatch:

$$\left|\frac{V_A - V_B}{V_A}\right| C_B^{min} = 0.1 \qquad Eq.17$$

Where V_A and V_B are the atomic volume of the solvent and solute, respectively. In systems with higher number of components, the determination of the critical solute concentration will be extremely complex since each element contributes differently to the volumetric strain. Therefore, Inoue formulated an empirical criterion for BMGs consisting of three rules (45):

a) To form a glass, a minimum of three components must be present in the alloy. The higher the number of components, the easier the glass formation.
b) An atomic mismatch above 12% should exist between the main constituent elements of the alloy.
c) The heat of mixing between participating elements should be negative.

2.3. Properties of bulk metallic glasses

BMGs exhibit some interesting features, such as high thermal stability, good corrosion resistance, high saturation magnetization, low coercivity, ductility at temperature close to T_g, high mechanical strength, etc. In this section we summarize some of the most important properties of BMGs.

The two main physical properties characterizing a metallic glass are its density and viscosity. As mentioned in previous sections, the glassy phase is a metastable state with increased free volume when compared with the equilibrium crystalline phase. Thus, glasses will have lower densities compared to their crystalline counterparts. However, Chen showed that these changes are mainly

anecdotal (46). Even slighter density differences are obtained with the crystalline phase in BMGs, since they can be synthesized with lower cooling rates.

In the supercooled liquid state, it is observed that viscosity is temperature and strain-rate dependent. For high strain-rates the Newtonian behaviour of the alloy breaks and the viscosity starts to increase (47).

Regarding their mechanical properties, bulk metallic glasses are characterized by high inherent strength (close to the theoretical one) and elastic strain due to their lack of plasticity. These properties highlight them as promising candidates for structural materials. However, the lack of plasticity also leads to shearing-off failure, which reduces its safety. As they do not possess slip systems, dislocation-plasticity is not possible and in yielding the deformation will be highly localized in thin shear bands. Although the local deformation within these shear bands is extremely high and may suffer a sharp drop in viscosity, the total plastic deformation in the whole body will be limited. However, at high temperatures BMGs show an homogenous flow. The supercooled liquid state is reached and the shear is spread across the whole volume. This fact forms the basis for the "thermoplastic formation" (TPF) of BMG that enables its nanopatterning (48,49).

Few studies have been conducted on the electrical properties of bulk metallic glasses. However, high electrical resistivities above 200 μΩcm (50) are expected due to their less packed structured. In Zr-based BMGs, Haruyama found a decrease in electrical resistivity with increasing temperatures below T_g. On the contrary, above the T_g the opposite evolution was observed until crystallization occurred (51).

From Herzer's theory (52), the excellent soft magnetic properties of BMGs can be understood. Herzer postulated that magnet-crystalline anisotropies in a polycrystalline material average out (i.e., reduces) when the grain size is smaller than the magnetic domain wall. Therefore, as metallic glasses have no grain boundaries, minimal resistance to coherent domain motion is exhibited when an external field is applied. The coercivity in these systems is especially low.

2.4. Synthesis methods of bulk metallic glasses

In the early stages of metallic glass production where binary and ternary alloys with low GFA were mainly studied, high cooling rates were needed. Therefore, only wires and sheets with limited thicknesses in the range of tens of micrometres were accessible. However, the development of bulk metallic glasses reduced the complexity of the synthesis as they require lower cooling rates. We present in this section three different techniques for synthesizing BMGs.

2.4.1. Melt-spinning

This technique emerged from the modification made by Chen and Miller (53) of Pond and Maddin's initial design. From this, a continuous cast of metal filaments in the glassy state is possible thanks to the good thermal contact of the melt with the substrate. It consists of ejecting a jet of the molten alloy from a nozzle onto the surface of a cold and thermally conductive wheel that spins at high rotational speeds.

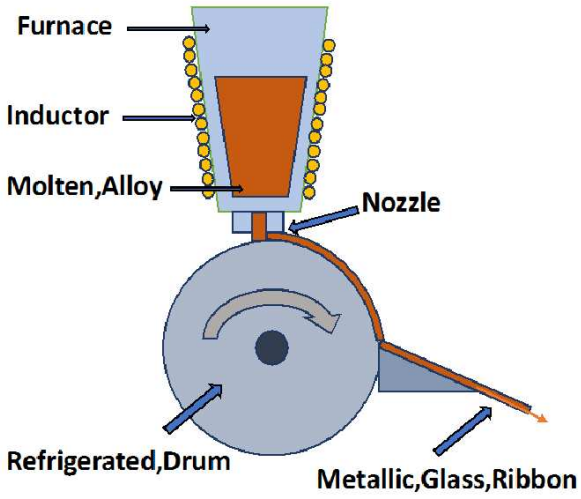

Figure 6. Schematic of a single roller melt-spinning method (54).

Induction heating equipment supplied by a high frequency generator melts the alloy in the crucible. An inert gas applies pressure to the melt to force it out to the nozzle. When the melt contacts the wheel's surface it solidifies rapidly, and it is lifting of as a thin ribbon.

2.4.2. Arc melting and suction-casting

In this method the molten alloy is sucked into a metallic mould with high thermal conductivity thanks to the pressure difference between the melting chamber and the mould. The alloy ingot is placed in a crucible connected to the mould by an orifice. The sample is then melted by an arc-current transfer from a tungsten electrode. Following, the orifice connecting both chambers opens when the pressure in the mould is small enough to suck the liquid. Normally, an Ar-gas flux is introduced to the melting chamber to minimise impurities.

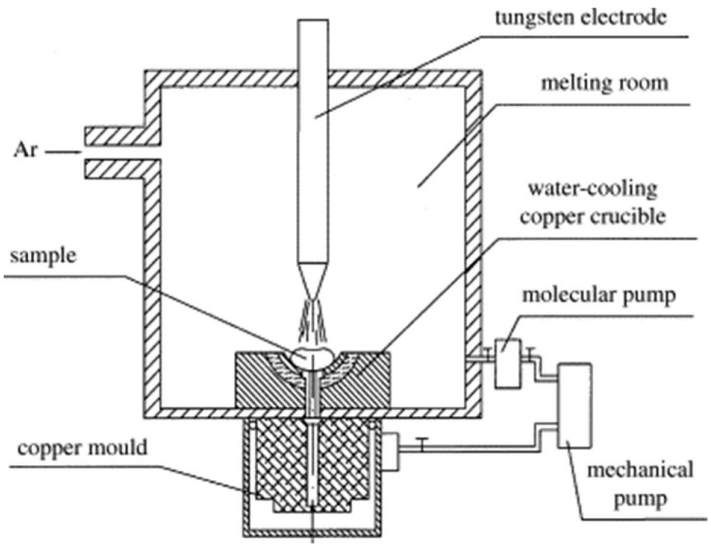

Figure 7. Schematic of the suction-casting method (55).

2.4.3. Additive manufacturing

The additive manufacturing approach consists of continuously melting the alloy (normally in powder form) by the scanning of an energy source (e.g., laser beam). This allows to overcome the limited sizes in conventional BMG synthesis techniques, and print layer-by-layer complex samples. Some examples are direct metal deposition (DMD), selective laser melting (SLM), laser foil printing (LFP), and electron beam melting (EBM) (56).

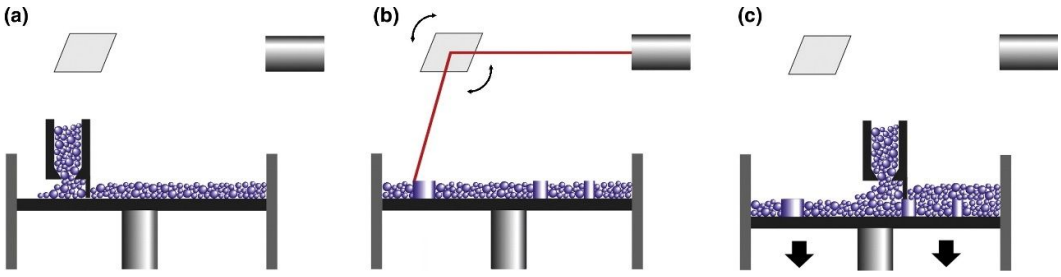

Figure 8. Schematic of the SLM operation (57).

However, the microstructure obtained with this strategy is far from being homogenous. An alternating distribution of melt pools (MPs) and heat-affected zones (HAZs) is obtained.

2.5. Applications

As introduced in the previous sections that BMGs meet the right properties for various applications. Their high yield strength, low Young's modulus or their formability in the supercooled liquid state makes of them attractive candidates for specialized structural applications. For example, the combination of high yield strength and elastic strain limit allows to use slimmer wires and reduce the number of loops in a spring without altering its performance.

The outstanding formability and plasticity of BMGs in the supercooled liquid state, as well as its negligible volume shrinkage provides an economic approach to nano-fabricate metallic materials for nano-machines and MEMS (58). Traditionally, the nanopatterns and structures needed in such applications were fabricated through lithography or ion etching. Therefore, they were generally limited to semiconductor technology.

In biomedical applications, corrosion resistances and biocompatibility are two of the most relevant properties to consider in the material selection. Thanks to the homogeneous microstructure without grain boundaries or defects, BMGs are less prone to develop intergranular corrosion or stress-corrosion cracking (59).In addition, the low Young's modulus of BMGs facilitates the compatibility with the surrounding bone in implants.

Finally, the extraordinary soft magnetic properties of BMGs have been exploited, among other applications, in pulse transformers and magnetic cores for power transformers. Especially successful are the amorphous alloys on the basis of Fe-B, as they are industrially produced for different trademarks (METGLAS or VITROVAK) (60).

2.6. Pt-based BMGs

Pt-based bulk metallic glasses are characterized by their high glass-forming ability, thermoformability and relatively low glass transition temperature.

Rheological studies (61) showed that Pt-based metallic glasses exhibit a strong temperature dependence in the supercooled liquid. The drop in viscosity with temperature was more pronounced than in Pd- or Zr-based alloys.

The wide range of temperatures for the supercooled liquid state allow the synthesis of Pt-based BMGs in the size order of 20 mm (62). In addition, its high noble behaviour prevents its oxidation and embrittlement during its synthesis and processing in air. The main field of application for this family of BMGs is in biomedical implants and jewellery goods (63).

3. Experimental

3.1. Arc-melting/Suction-casting

Master ingots with nominal composition $Pt_{57.5}Cu_{14.7}Ni_{5.3}P_{22.5}$ (at.%) were produced from pure elements by suction casting in an Arc Melter AM from Edmund Bühler GmbH (Germany). The equipment employed is shown in Figure 9. These ingots have been cast under conditions of vacuum and purification by means of a Ti-gettered Ar atmosphere.

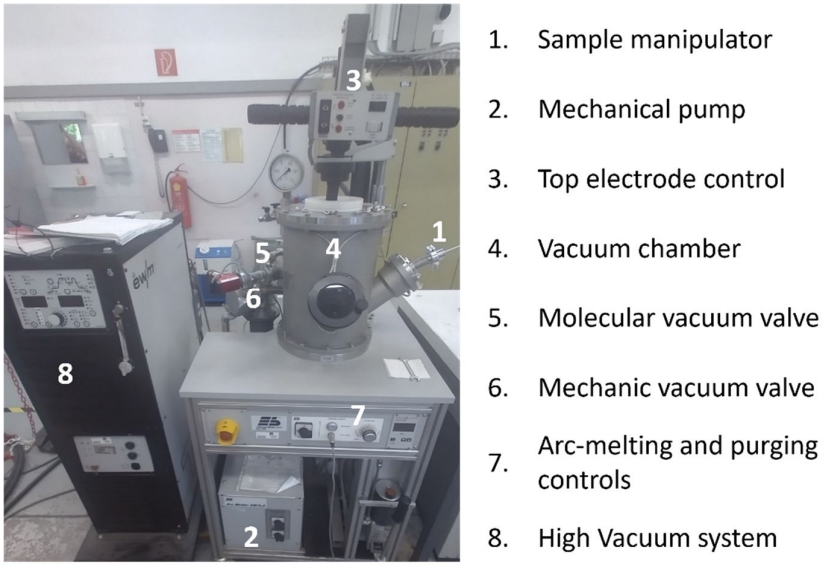

Figure 9. Instrumental setup of the arc-melting/suction-casting equipment used in this work.

3.2. Differential Scanning Calorimetry (DSC)

The goal of this technique is to measure the heat exchange in a material from which physical transitions, structure, kinetics, and other transformations can be obtained. Various approaches are available for DSC, with heat-flux and power compensation among the most prominent. They have in common that the signal measured is proportional to a heat flow rate, allowing the detection of thermal transition's time dependences.

In heat flux DSC, both reference and sample's crucibles are contained in the same furnace. A defined exchange of heat is well-defined to the system (normally through a thermoresistance) and the temperature difference between reference and sample due to their different heat capacities is measured in a thermocouple

(Figure 10.a). Therefore, the signal that one detects is in the form of a potential difference.

In power-compensated DSC, sample and reference crucibles are placed in two identical and independent microfurnaces (Figure 10.b). In the beginning of the measurement, the same heating power is supplied to both microfurnaces by an adjustable Joule's heater. If some thermal mismatch is present between the sample and the reference, the temperatures measured by their corresponding resistance thermometers will differ. Such difference is used to supply additional heat power to the sample furnace until it is completely compensated.

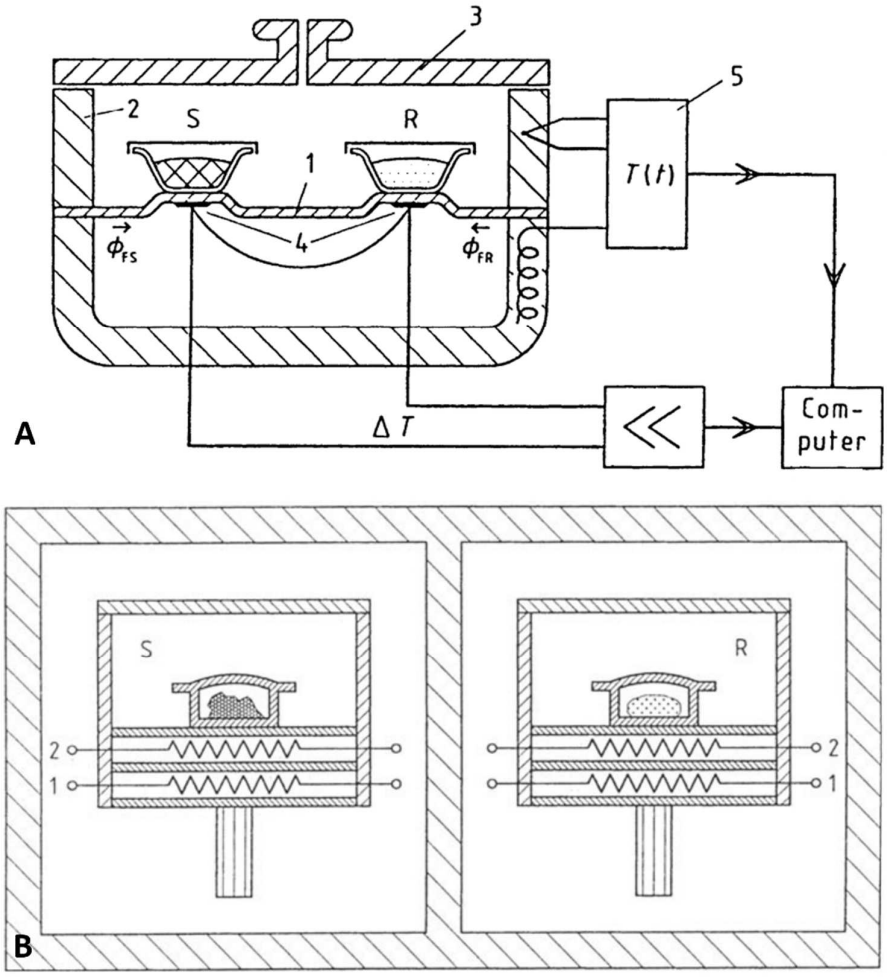

Figure 10. Schematic of the (a) heat-flux and (b) power compensator DSC systems (64).

3.3. Flash DSC

To properly study metallic glasses in a DSC measurement with heating segments above the melting temperature, high cooling rates must be employed. However,

conventional DSC instruments are limited to scanning rates up to 300 K/min. As a result, Flash DSC (also abbreviated as FDSC) emerged to address this issue.

To reach high heating rates with respect to the furnace, both calorimeter and sample must have small heat capacities. Thus, nano- or microgram weight samples should be considered. Similarly, the calorimeter must consist of thin dielectric membranes, like Si or SiN, with low thermal conductivity. This is necessary to accurately transport the heat from the heaters to the sample without losses through the integrated circuit printed in the membrane (65).

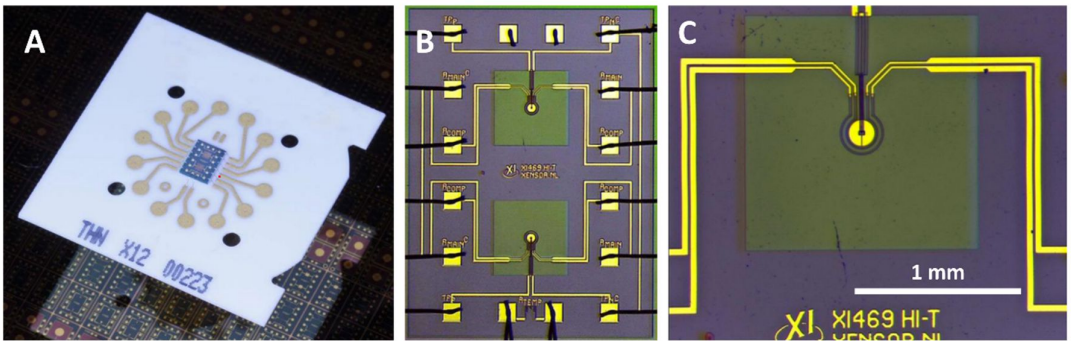

Figure 11. (a) High temperature nanocalorimeter ceramic chip with gold interconnections. (b) Magnified picture of sample and reference membranes. Each membrane has two concentric heaters and two thermocouples. (c) Close up of chip centre (66).

The FDSC measurements in the present work were performed on the power compensated system Flash DSC 2+ from Mettler Toledo. High temperature sensor chips (Figure 11) from Mettler Toledo were employed. To remove internal stresses and to correct the thermocouple signal of the chip, conditioning and correction of the same were carried out following the producer indications.

The samples were prepared by scraping off the Pt-based BMG disk obtained in the arc-melting system. Those samples with sizes fitting in the chip centre were selected to ensure the direct heating of the whole volume. With the help of an electrostatic manipulator, the samples were placed in the chip centre before closing the measuring cell and insulator lids (Figure 12.c and 12.d). A continuous Ar-flow of 80 ml/min was established during the measurements to prevent oxidation.

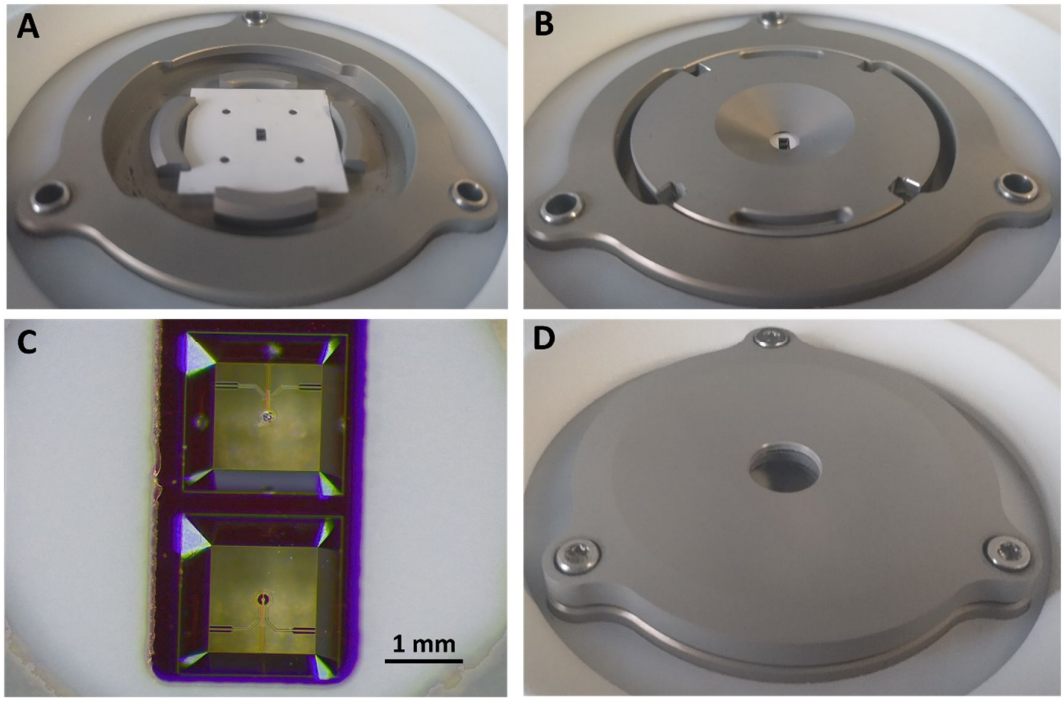

Figure 12. FDSC assembly steps: placement of (a) chip in the measuring cell, (b) clamping plate, (c) sample in chips membrane, and (d) measuring cell lid.

3.4. In-situ SRXD

When charged particles are accelerated, they emit radiation as an attempt to rearrange their electric field. For relativistic electrons, the energy loss rate (radiated power) when gyrating in a magnetic field will be as follows:

$$P_r = -\left(\frac{dE_e}{dt}\right) = \frac{\gamma^4 e^2}{6\pi\varepsilon_0 c^3}|a_\perp|^2 \qquad Eq.18$$

being e the electron's charge, ε_0 the vacuum permittivity, c the speed of light, γ the Lorentz's factor ($\gamma = (1 - v^2/c^2)^{-1/2}$), and $a_\perp$ the electron's acceleration normal to the magnetic field given by the equation of motion:

$$\gamma m_0 \frac{d\bar{v}}{dt} = ze(\bar{v} \times \bar{B}) \qquad Eq.19$$

From Equation 18, high energetic radiation can be obtained if very relativistic particles are generated. In addition, the relativistic aberrations between the frames of reference of the particle and of the observer beam directs the radiation tangentially to the particle's velocity. The radiation emitted from a relativistic particle will be concentrated into a small cone of $1/\gamma$ opening angle. Thus, very

relativistic particles are needed to obtain both, high energetic and collimated radiation. It is in the generation of such particles where synchrotron facilities play a prominent role.

In synchrotron facilities, electrons are first accelerated to MeV in a linear accelerator before entering a booster for even greater acceleration (up to GeV). They are then transferred to a storage ring where they are obliged to follow a circular trajectory by the bending magnets distributed along the installation. Several openings in the vacuum chamber allow a small amount of radiation to be guided to experimental stations at the end of so-called beam lines (Figure 13). Due to the ring's geometry, electrons will emit a fixed spectrum of radiation when accelerated in the bending magnets. Moreover, these will show a wide broadband. Different magnetic insertions are necessary to generate specialized photon beams with high collimation. These insertions are introduced before the beamlines openings and provides of sinusoidal transverse motion to the electrons.

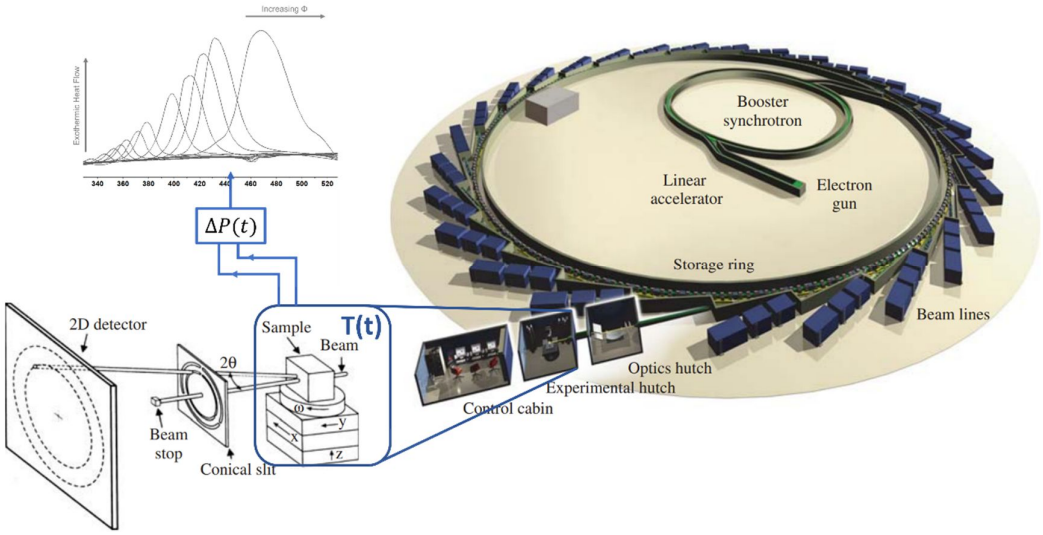

Figure 13. Schematic of a synchrotron radiation facility and in-situ FDSC with SXRD measurement (67).

At the end, an intense, high collimated, brilliance, tuneable and well-defined radiation is obtained. These properties make synchrotron radiation perfect to study small samples with fast structural changes unobservable on a lab-based source. An increased sensitivity and resolution of diffraction peaks in the X-ray diffraction pattern is achieved. Therefore, the combination of synchrotron X-ray

diffraction (SXRD) with other techniques such as FDSC or synthesis procedures allows the analysis in situ and in real time of the mechanisms that take place.

The SXRD measurements and in-situ FDSC were performed in the European Synchrotron Radiation Facility (ESRF). More precisely, it's Extremely Brilliant Source (EBS) was used on the beamline ID 13. A beam of 13.0 keV wavelength and 30 µm in diameter was used. The high photon flux obtained from the focus beam allowed the collection of high-quality diffraction patterns. A Dectris Eiger 4 M detector with a continuous readout that enables high frame rates (up to 750 frames per second) was used and placed at 0.1091 m from the sample. An Al_2O_3 reference (NIST 674a) was used to calibrate the diffraction patterns. The azimuthal integration for the acquisition of the geometric information of the sample was carried out with the pyFAI software (68).

4. Results and Discussion

4.1. In-situ characterization: Simultaneous measurement of SXRD during FDSC experiments

In this chapter the results of the synchrotron-based characterization of the Pt-based BMG are shown. This alloy was prepared as a master alloy from industrial grade material and suction cast under a high purity argon atmosphere. An alloy sample weighed in nanograms was set in a gold chip (see example of Figure 11 in Experimental section) for Flash Digital Scanning Calorimetry (FDSC) experiments. The sample was then placed in the synchrotron beamline to perform in-situ and ex-situ FDSC measurements. The method employed in the FDSC consisted of a continuous cycle of heating and quenching segments separated by short isotherms to ensure thermal equilibration. The first segment consists of a long isotherm at 25ºC, during 1 s. Then, the temperature cycles are carried out. They first consist of a heating ramp from the initial room temperature (RT) until the top temperature of 700 ºC. Next, an isotherm at this temperature during 0.1 s is performed before the quenching at -50000 K/s that will lead the temperature again to the initial 25 ºC. It will remain at RT during 0.1 s before starting the next cycle, which will have the same shape but with a different heating rate. In global, the temperature program has fourteen cycles with the following heating rates: 10000, 7500, 5000, 4000, 3000, 2000, 1000, 750, 500, 400, 300, 200, 100, and 50 K/s. The complete temperature program is shown in Figure 14.a.

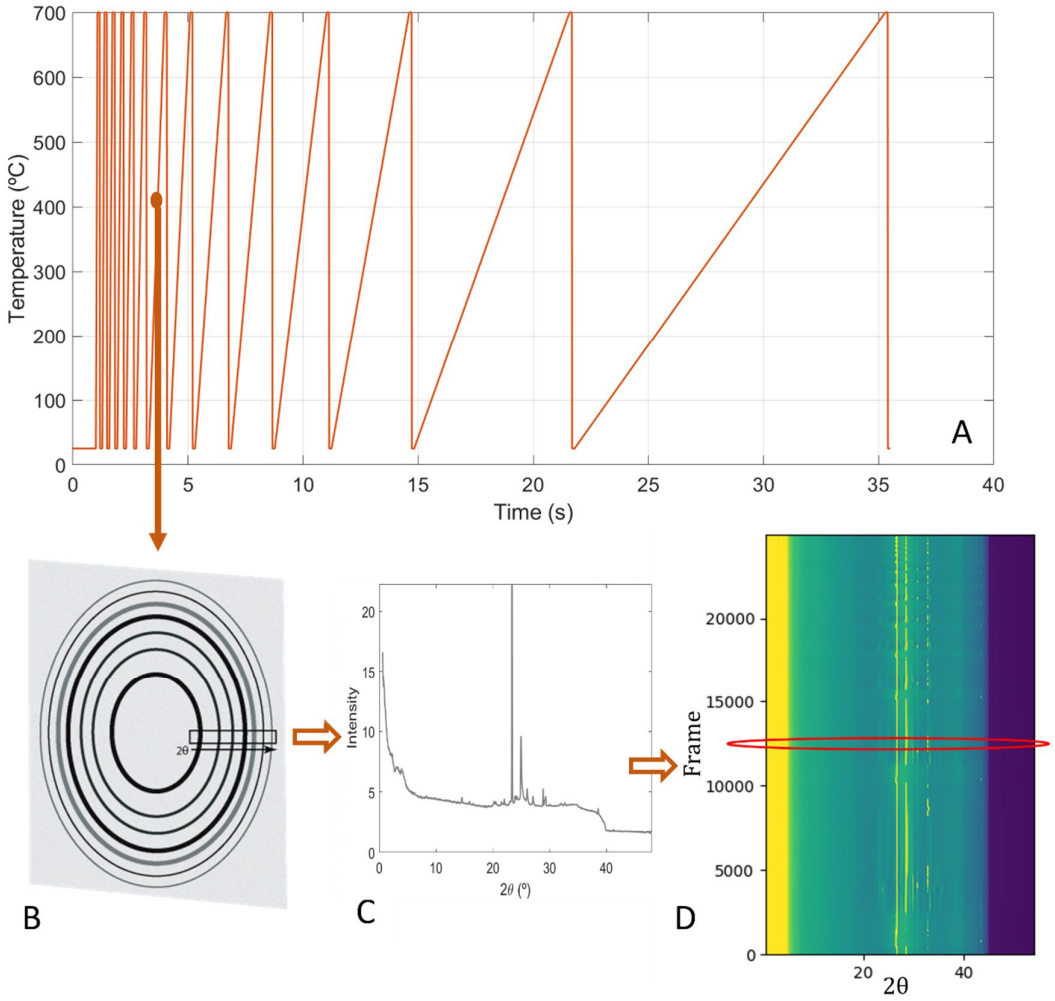

Figure 14. a) Temperature program for FDSC measurements. b) XRD diffraction screen for a single frame. c) Integrated diffraction pattern for a single frame. d) Intensity map of the integrated diffraction pattern for all the frames in the in-situ temperature program.

During the in-situ measurement, the sample is irradiated by X-ray photons of 13.1 keV wavelength. The diffraction pattern from the sample's interaction with the X-rays is continuously recorded during the FDSC experiment. A framerate of 714 Hz was employed for the XRD pattern detection. Integrating the diffraction signal of the detector (Figure 14.b) the one-dimensional (1-D) diffraction pattern at each frame is obtained and saved (Figure 14.c and 14.d). With that, the alloy's phases evolution during the temperature treatments can be known.

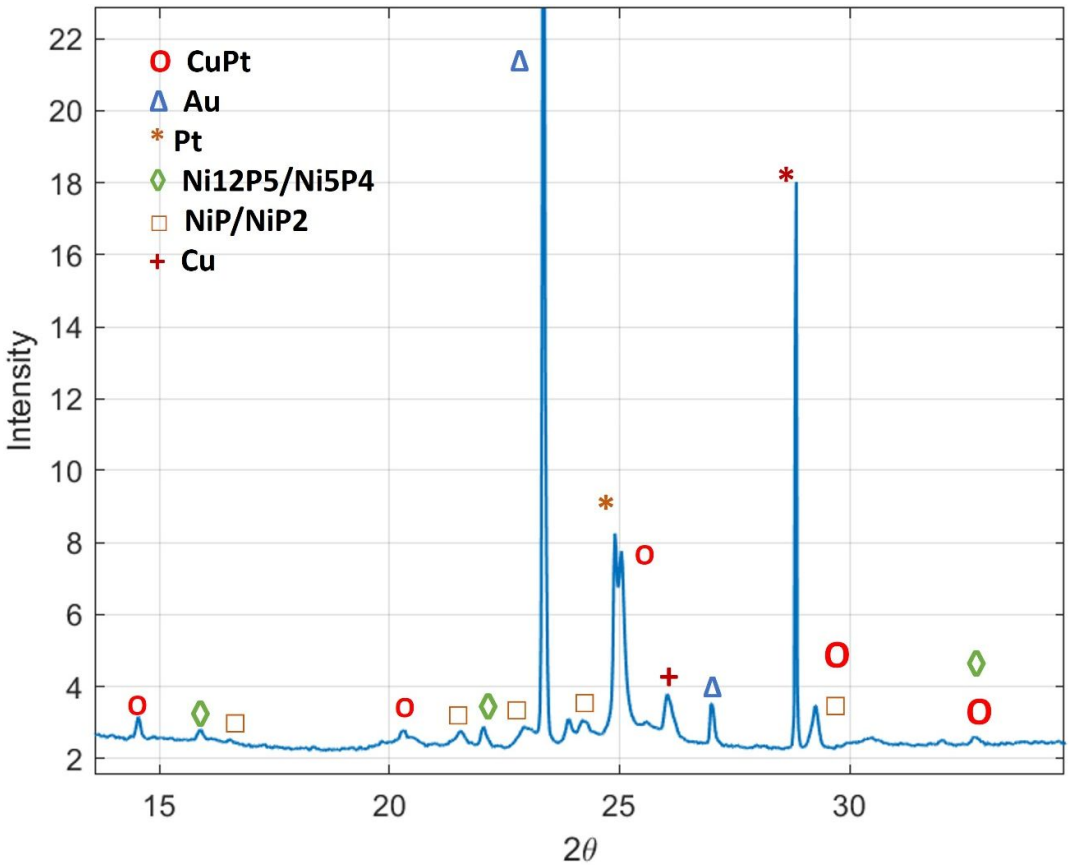

Figure 15. XRD profile (1-D) and phase identification of one frame corresponding to the dynamic segment of the FDSC method at heating rate 100K/s.

One can take the XRD profile of one of the frames in the central range of a heating ramp, e.g., the 100 K/s dynamic segment, to identify the distinct phases and partial ordering that nucleate in the sample. This delimitation is selected because the integrated intensity in this range of temperatures shows the highest number of peaks (Figure 14.d.). Using the Inorganic-Crystallographic Open Database (Inorganic-COD) and the software Match! from Crystal Impact, phase identification of the intensity peaks in the XRD profile can be performed. Figure 15 shows the peaks identification of one frame's XRD profile.

As one can appreciate from the XRD profile, multiple crystalline grains with chemical heterogeneity are found during the heating of the metallic glass. It has been possible to identify six different phases. Two metallic compounds, Pt and Cu, and two binary phases with different chemical composition depending on the temperature.

In addition, the gold (1 1 1) and (2 0 0) peaks are detected. These correspond to the chip' signal and show the most prominent signal in the diffraction pattern, at $2\theta = 23.45\,°\ and\ 27.1\,°$. Moreover, it can be seen in Figure 14.d that the chip signal is present in all the frames. Thus, one can use the change in the chip's peak angle over the course of FDSC measurement to calculate the actual temperature of the sample.

4.1.1. Determination of sample's temperature during in-situ measurements

From the XRD patterns, the position of the Au (1 1 1) peak for all frames is saved and plotted against time. Figure 16 superimpose the shift of the scattered radiation with the temperature program set in the FDSC experiments. The wavevector dependence with temperature can be calculated from Bragg's Law. The wavevector for a crystallographic plane is defined as follows (1):

$$q_{hkl} = \frac{4\pi}{\lambda}\sin\theta_{hkl} \qquad Eq.20$$

Where θ_{hkl} are the scattered angles of the waves interfering constructively, i.e., when the phase difference between two beams that scatter off two neighbouring planes is equal to an integer multiple of the incident wavelength (Bragg's Law):

$$n\lambda = 2d_{hkl}\sin\theta_{hkl} \qquad Eq.21$$

Being d_{hkl} the interplanar spacing for the plane family (h k l). For a cubic crystal, such as metallic Au, the interplanar spacing takes the next form:

$$d_{hkl} = \frac{a}{\sqrt{h^2 + k^2 + l^2}} \qquad Eq.22$$

Being a the lattice parameter. The temperature dependence of the lattice parameter can be studied, in first approximation, through a linear thermal expansion:

$$a = a_0[1 + \alpha(T - T_0)] \qquad Eq.23$$

Where a_0 is the reference lattice parameter at the temperature T_0, and α is the linear temperature expansion coefficient with units of $°C^{-1}$. Thus, combining and

simplifying the relations above, one gets that the wavevector depends inversely on temperature as:

$$q_{hkl} = \frac{2\pi}{a_0[1+\alpha(T-T_0)]}\sqrt{h^2+k^2+l^2} \qquad Eq.24$$

Therefore, in the heating and quenching segments of the FDSC, the wavevector of the chip should decrease and increase, respectively. Additionally, it should stay constant in the isothermal segments. However, when superimposing the temperature program of the FDSC with the wavevector shift along the experiment, important mismatches are found (Figure 16). First, the XRD pattern has a time lag with respect to the FDSC temperature program. The beginning of the first heating segment appears before the 1 s isotherm of the FDSC finishes. This is attributed to the asynchronization between the heat control system in the FDSC and the X-ray trigger. Thus, the trigger that allows the X-rays to reach the sample last some time to open after the start of the isothermal segment by the FDSC.

To correct this time difference, the exact frame in which the first cooling starts is determined. The last frame with a wavevector smaller than $26.6\,nm^{-1}$ was considered as the starting point for the cooling segments (see insert in Figure 16). Then, taking the difference between the corresponding time of the cooling starting frame in the XRD with the time in the DSC temperature program, one obtains a lag for the X-ray trigger of $t_{shift} = 0.7544 \pm 0.0014\,s$.

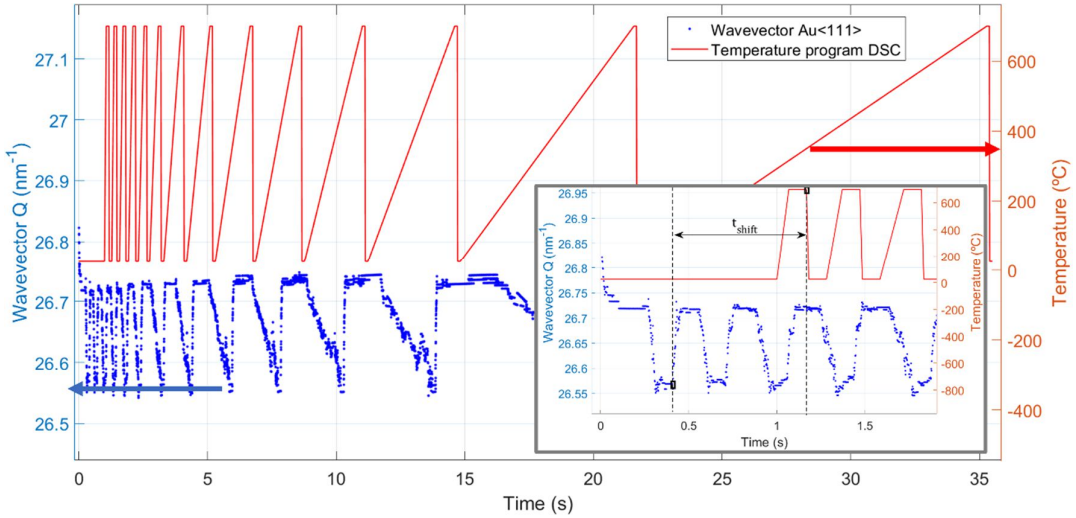

Figure 16. Comparison of the temperature program introduced in the FDSC method with Au (1 1 1) wavevector evolution. Insert with zoom at short times and calculation of trigger time shift.

The second mismatch that one can observe is the duration of the bottom isotherms (25 ºC). While in the temperature program of the DSC all the isothermal segments have the same duration, $0.1\ s$, in the wavevector data these isotherms show an increasing duration when reducing the heating rate. The most prominent example of this occurs in the last temperature cycle, where the isothermal segment in the wavevector has a duration close to $5.5\ s$ instead of $0.1\ s$. These differences can be attributed to the fact that the actual temperature of the lowest isotherm during in-situ conditions differs from the room temperature set in the FDSC program. The X-rays interaction with the sample heat it up, preventing the cooling to lower temperatures. Then, as the FDSC employed is a power compensation machine (see Section 3.3), when heating, it would not provide heat to the sample until the reference temperature do not reach this annealing temperature. Thus, the duration of the actual isotherm depends on the heating rate employed for the FDSC as follows:

$$\Delta t_{in-situ} = \Delta t_{25°C} + \frac{T_{iso}^{in-situ} - 25}{\Phi} \qquad Eq.25$$

Where $\Delta t_{25ºC}$ is the isothermal duration set in the FDSC program ($0.1\ s$), Φ is the heating rate employed in the cycle under consideration, and $T_{iso}^{in-situ}$ the actual temperature of the bottom isotherm under the influence of X-rays. The actual temperature of the bottom isotherm is determined analysing the exact duration of the isotherm in the last temperature cycle ($\Phi = 50\ K/s$). Taking as isothermal segment all the points with a wavevector above $26.72\ nm^{-1}$ (shadowed segment in Figure 17) one obtains a value of $\Delta t_{in-situ} = 5.5042\ \pm 0.0014\ s$. Replacing this value in Equation 25, we get a $T_{iso}^{in-situ} = 295.21\ °C$. As shown in Figure 17, after correcting the bottom isotherm temperature and the time lag introduced by the X-ray trigger, the temperature program matches satisfactorily with the wavevector shape.

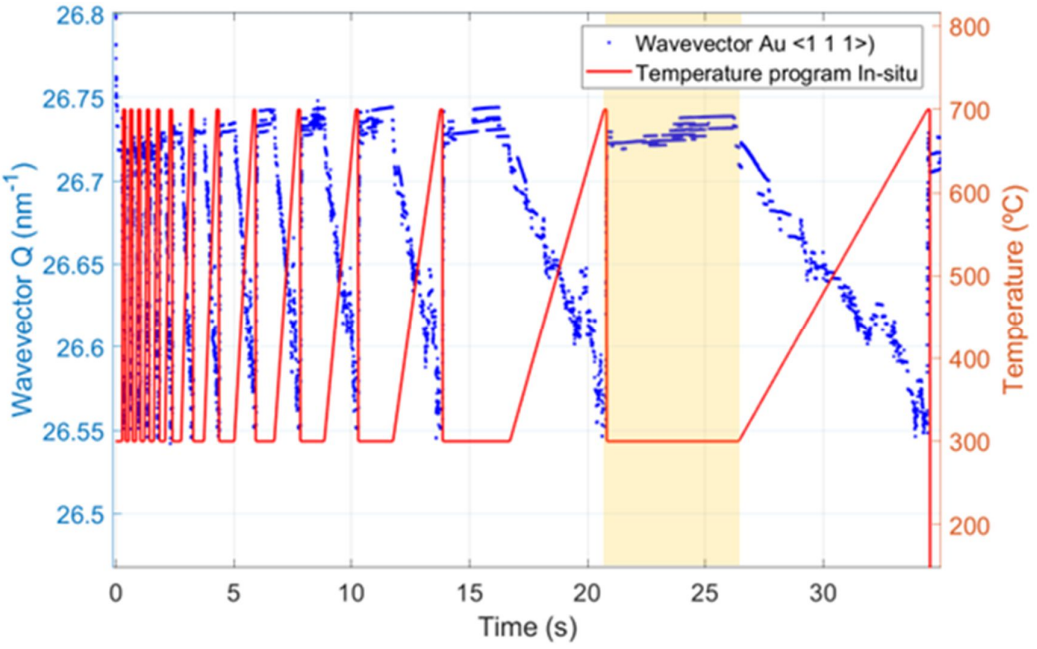

Figure 17. Superposition of corrected temperature program and Au (1 1 1) wavevector evolution.

Once the correct times and segments of the in-situ characterization are known, one can determine the exact temperature of the chip, i.e., of the sample, by converting the wavevector to temperature through Equation 24. To do so, one needs first to estimate the thermal expansion coefficient of gold.

For the reference state (a_0, T_0) in Equation 24 the first isotherm of the experiment is considered, before any heating or cooling segment take place. It is in this isotherm where one can be more confident regarding being in thermal equilibrium. During this period the same conditions of X-ray radiation and FDSC inactivity (as the sample is already heated by the X-rays no-heat will be introduced by the power compensator) are hold. Thus, $T_0 = 295°C$ and $a_0 = \frac{2\pi}{\langle q^0_{111} \rangle}\sqrt{3}$ are considered, being $\langle q^0_{111} \rangle$ the average value of the wavevector in the first isotherm. Calculating one obtain a reference lattice parameter of $a_0 = 0.4073\ nm$, in very good agreement with literature, 4.08 Å (69,70).

Then, the linear fitting of the normalized lattice parameter with temperature, Equation 23, is performed. In the first iteration of the linear fitting, the corrected temperature program of the FDSC is used as data, while the reference temperature, T_0, and the thermal expansion coefficient, α, are independent

variables (not constants) of the fitting. As shown in Figure 18.a., the use of the corrected temperature program of the FDSC as the temperature to fit, generate a dispersion of the data points. However, a clear linear relation is obtained and reliable values for α and T_0 can be extracted: $1.303 \times 10^{-5}\ °C^{-1}$ $(1.295 \times 10^{-5} \mid 1.310 \times 10^{-5})$ and $296\ °C$ $(294.9 \mid 297.1)$, respectively.

With these new variables and isolating temperature in Equation 24, one can generate the new temperature profile of the chip (Figure 18.b). With this fitting one obtain a thermal expansion coefficient in good agreement with literature (69), and the actual sample's temperature along the in-situ measurements.

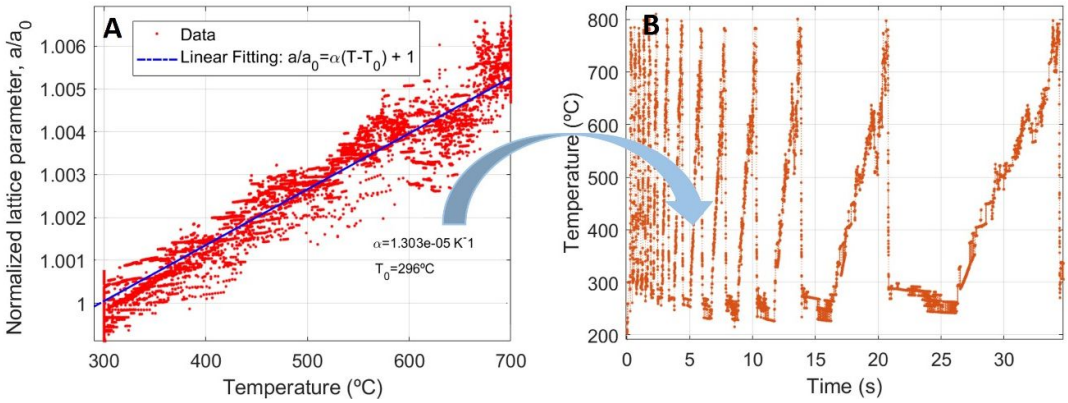

Figure 18. (a) Fitting of the normalized lattice parameter of chip with the corrected temperature program of the FDSC. (b) Extraction of gold thermal expansion coefficient and conversion of chip's wavevector to temperature.

4.1.2. Crystallization and melting of phases

The measured FDSC curves for the heating ramps of the in-situ characterization are shown in Figure 19. As one can observe, for temperatures lower than 296 ºC no heat flow is detected. This agrees with the longer isothermal segments found when analysing the chip's wavevector. This constant annealing around 296 ºC due to the irradiation of photons have two important consequences. First, it prevents the detection of the alloy's glass transition temperature, T_g, as it is known to be around 230 ºC (71,72). Second, the power compensation system experiences a transient state just after reaching 296 ºC. This translates into a noisier signal for low heating rates and to the appearance of an endothermic peak for higher heating rates.

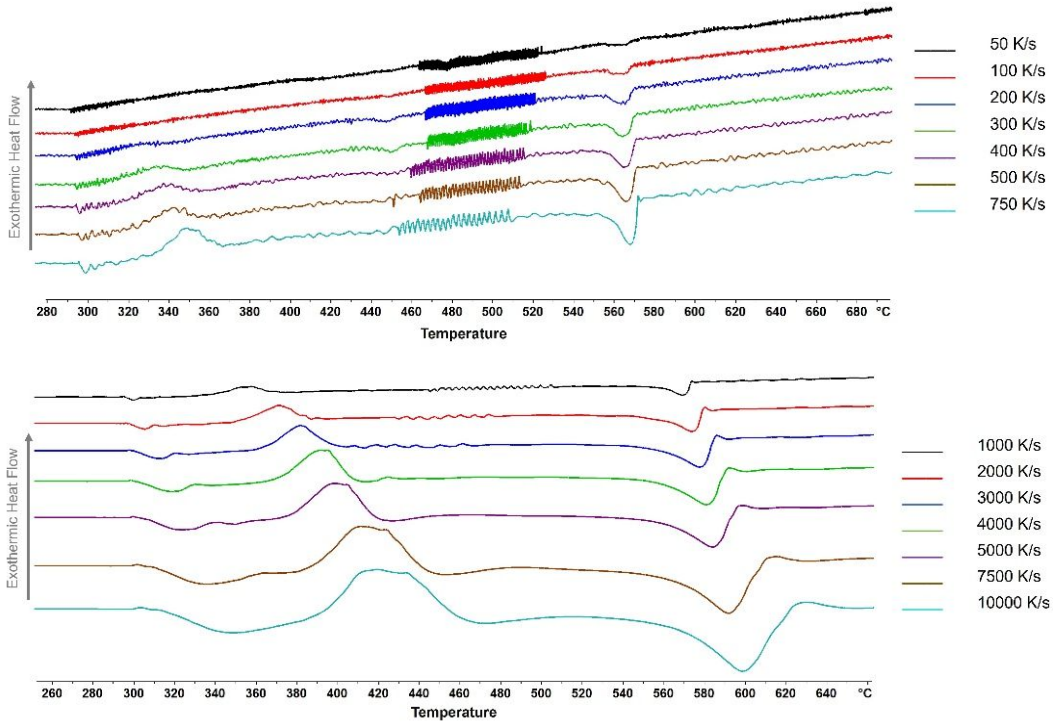

Figure 19. In-situ flash DSC measurements of $Pt_{57.5}Cu_{14.7}Ni_{5.3}P_{22.5}$ with heating rates of 50 - 10000 Ks^{-1}.

In all heating rates we observe a pronounced crystallization peak. Thus, the alloy is partly amorphized after each quenching cycle. In addition, the crystallization temperatures rise with higher heating rates, broadening the supercooled liquid region ($\Delta T_x = T_x - T_g$). If one inspects in more detail this primary crystallization peak may conclude that it is an overlap of different populations. Through deconvolution of gaussians, one finds that four different phases crystallize in this range of temperatures. These deconvoluted peaks are shown as T_{x2}, T_{x3} , T_{x4} and T_{x5} in Figure 20.

Before this primary crystallization, one can see that for low heating rates, where the transient state shadows a shorter range of temperatures, an earlier crystallization peak is present in the signal (indicated as T_{x1} in Figure 20). By increasing the temperature, two melting transitions are found in the heat flow curves. The first one, with its onset temperature named as T_{m1}, is found at lower temperatures and has smaller enthalpies. In contrast, the second melting peak, with its onset and liquidus named as T_{m2} and T_{l2}, shows a broad range of temperatures and a high enthalpy, similar to the primary crystallization. Thus, it would be the superposition of several melting processes. However, due to its

smoother profile, with non-perceptible multimodal shape, a reliable deconvolution is not possible. All characteristic temperatures for each heating rates are summarized in Table 1.

Table 1. Summarized peak temperatures of the different crystallizations and, melting and liquidus temperatures of the endothermic peaks of $Pt_{57.5}Cu_{14.7}Ni_{5.3}P_{22.5}$ in in-situ measurements.

$\boldsymbol{Heating\ rate\ (K \cdot s^{-1})}$	$\boldsymbol{T_{x1} \pm 1\ (K)}$	$\boldsymbol{T_{x2} \pm 1\ (K)}$	$\boldsymbol{T_{x3} \pm 1\ (K)}$	$\boldsymbol{T_{x4} \pm 1\ (K)}$	$\boldsymbol{T_{x5} \pm 1\ (K)}$	$\boldsymbol{T_{m1} \pm 1\ (K)}$	$\boldsymbol{T_{l1} \pm 1\ (K)}$	$\boldsymbol{T_{m2} \pm 1\ (K)}$	$\boldsymbol{T_{l2} \pm 1\ (K)}$
10000		408	421	434	441			550	617
7500		406	412	423	434			552	605
5000	330	390	400	405	409			551	594
4000	325	375	390	395	397	439	461	552	590
3000	316	372	380	383	388			553	586
2000	315	352	362	373	384			556	582
1000	311	343	353	358	362			560	576
750								559	575
500								560	574
400						453	457	559	574
300						446	464	551	574
200						445	458	566	572
100								560	573
50								559	572

The low signal-to-noise ratio for heating rates lower than 1000 K/s prevents a reliable deconvolution of the primary crystallization peak. Also, T_{x1} is only distinguishable in five heating rates as for the others it is shadowed by the transient state of the heat flow. Similarly, T_{m1} is shadowed by the primary crystallization peak or by low signal-to-noise ratios in most of the heating rates.

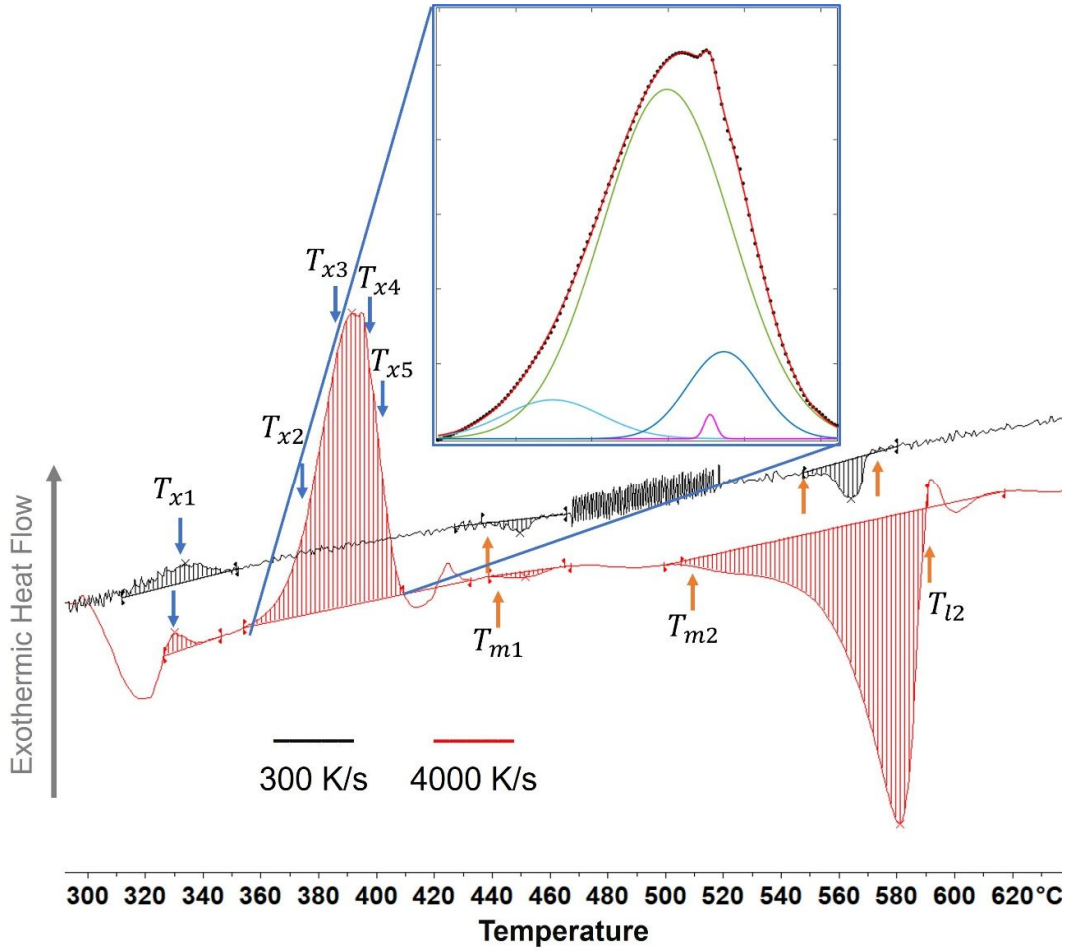

Figure 20. *In-situ FDSC measurement of $Pt_{57.5}Cu_{14.7}Ni_{5.3}P_{22.5}$ at 4000 (red) and 300 (black) Ks^{-1} with marked points of crystallization temperatures T_x, melting temperature T_m, and liquidus temperature T_l. Insert with gaussian deconvolution of the primary crystallization peak.*

With the values in Table 1 and knowing the relative time for each temperature with respect to the start of the corresponding heating ramp, one can draw the continuous heating transformation (CHT) diagram of the crystalline phases (Figure 21). As indicated in the diagram, the first phase to crystallize has its nose shifted to lower times and has a thinner region of existence compared with the phases of the primary crystallization peak.

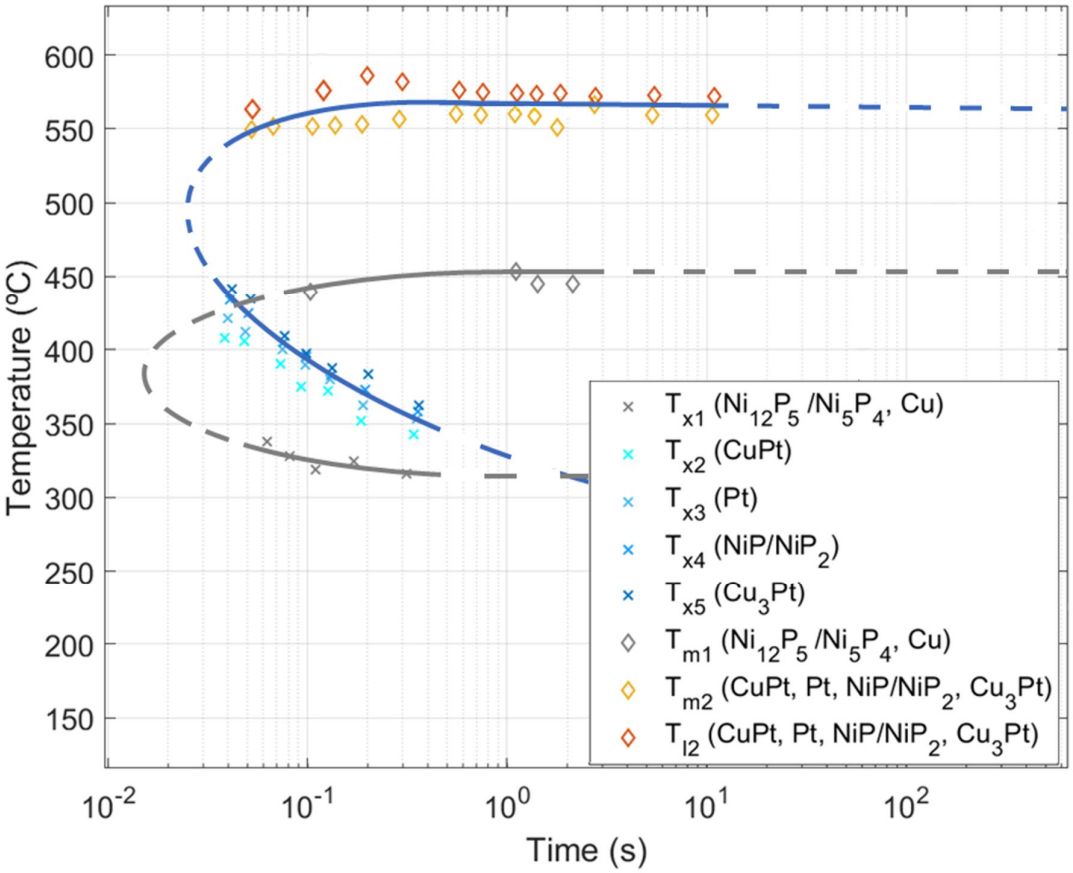

Figure 21. CHT diagram of $Pt_{57.5}Cu_{14.7}Ni_{5.3}P_{22.5}$ in in-situ conditions

The next step is to correlate the crystalline phases identified in the XRD pattern shown in Figure 14 with the transitions measured during FDSC experiments. In a first approach, one can study the evolution of the diffraction pattern with temperature in the heating ramp. To do so, we plot in Figure 22 the diffraction patterns of four different frames in a same heating cycle (e.g., 100 K/s).

In the as-quenched frame, a broad intensity peak in the range of $2\theta = [22\,, 28]°$ is found. It is attributed to the amorphous matrix of the alloy. In addition, some sharp peaks are superimposed to the amorphous halo. As mentioned, the peaks with scattering angles of $23.45\,°$ and $27.1\,°$ correspond to the metallic gold chip. However, the signals at $24.85\,°$ and $28.75\,°$ correspond to the (1 1 1) and (2 0 0) planes of metallic platinum. Thus, the sample is not completely amorphized in the quenching, but it contains some crystalline clusters in the amorphous matrix.

One can check the crystallization of metallic Pt during quenching by plotting the intensity of the scattered X-rays in the plane (1 1 1) for each frame i.e., for each timestep in the FDSC program. As shown in Figure 23, the intensity of the peak

at $2\theta = 24.85$ ° drops to zero in the final stages of the heating ramp ($T_{m,Pt}$), but it rapidly reappears when the quenching begins ($T_{x,Pt}$, from cooling). Thus, our sample will have a non-zero crystalline fraction before the heating ramps, explaining why the enthalpies of the melting transitions are higher than the ones of the crystallization in the FDSC curves.

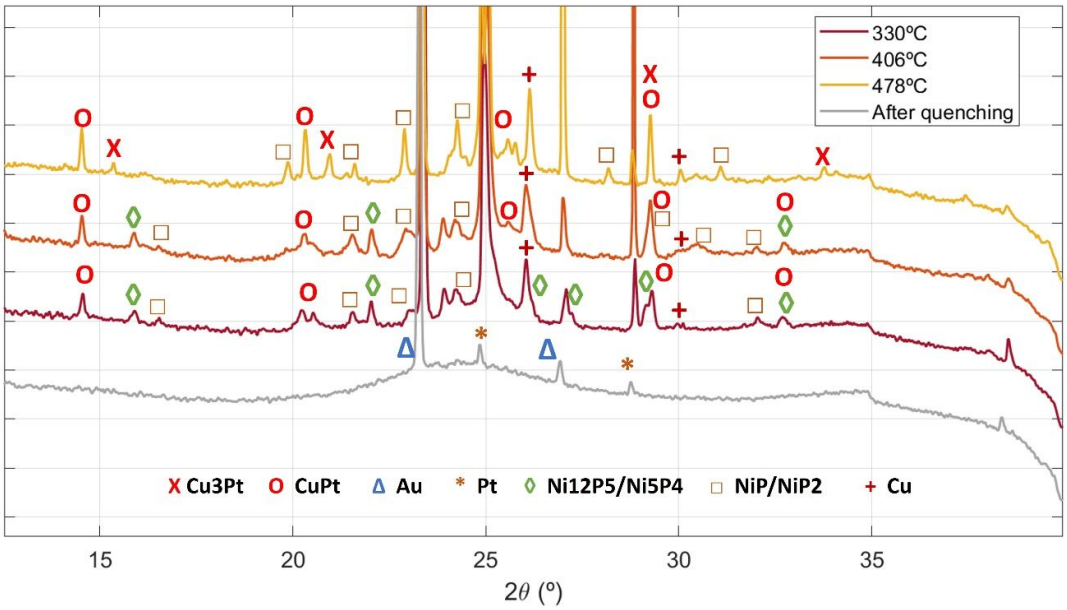

Figure 22. SXRD curves of the $Pt_{57.5}Cu_{14.7}Ni_{5.3}P_{22.5}$ sample at several temperatures of the100 Ks^{-1} heating segment.

In Figure 22, when the temperature starts to rise, new discrete peaks emerge from the amorphous halo. For low temperatures, just above the crystallization point T_{x1} in the FDSC, the diffraction pattern shows a rich population of Ni-P systems. Especially important are those systems with low P-content, such as $Ni_{12}P_5$ or Ni_5P_4. To a lower extent, one can observe the presence of some peaks corresponding to $CuPt$ and Cu. However, it is at higher temperatures when these Cu-systems turns out to be more prominent. Also, a transition in the Ni-P systems takes place during the heating. Those phases with lower P-content present in low temperatures are gradually replaced for P-richer phases like $NiP\ or\ NiP_2$. This behaviour is also observed in the synthesis of nickel phosphide nanoparticles, where phases with higher P/Ni ratios demand higher temperatures and times to nucleate (73,74). A similar thing happens for the Cu-Pt systems. At low temperatures it starts crystallizing CuPt thanks to the lower surface energy of this phase compared with Cu_3Pt (75). However, the nucleation of the Cu-rich phase

will begin to compete with CuPt at higher temperatures as the surface energy weight in the kinetics is reduced. In addition, from Figure 22 one can observe how the intensity of the metallic Pt experiences a significant increase between 406 ºC and 478 ºC. This indicates the growth of Pt crystalline phases formed during quenching and the nucleation of new crystallites. In consequence, the availability of Pt atoms is reduced, favouring the crystallization of Cu_3Pt over CuPt.

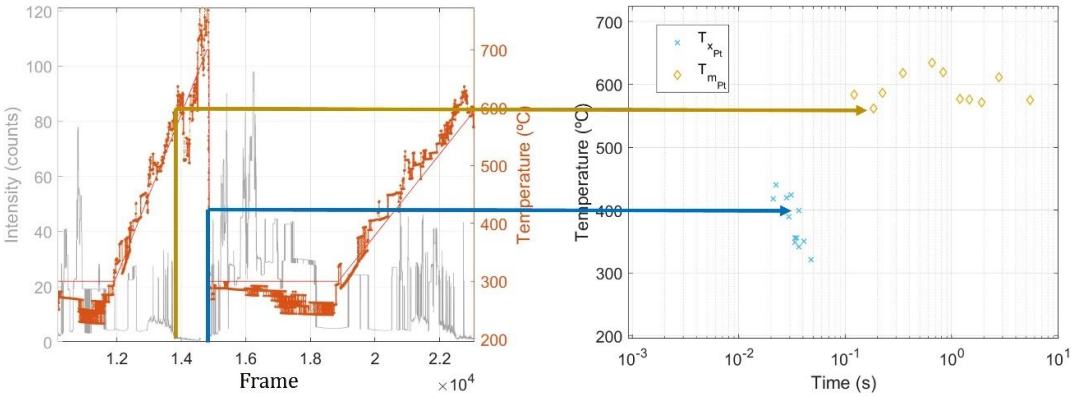

Figure 23. (Left) XRD intensity of $2\theta = 24.85°$ peak and chip's temperature versus frames. (Right) CHT diagram for the $2\theta = 24.85°$ peak.

With the overview provided by Figure 22, one can reduce the number of possible phases attributable to each transition in the FDSC. For example, one can consider that the first crystallization and melting transitions in FDSC measurements correspond to Ni-P systems with low P-content as their signal in the XRD are the first one in disappear. Similarly, as the peaks corresponding to Cu_3Pt are the last ones in being detected during the heating in Figure 22, one could assume that it is the responsible phase for T_{x5} in FDSC curves.

A more precise assignation of phases to thermal transitions can be performed by inspecting characteristic peaks' intensity in the XRD along time. Then, knowing the frames at which the intensity tends to zero (melting of the phase) and at which it starts to increase again (crystallization), one can elaborate its CHT diagram. It is the same procedure as the one done in Figure 23 for Pt phase. We select those scattering angles with higher intensities for each phase, i.e., $2\theta = 20.3\,° \; and \; 14.53\,°$ for CuPt, $2\theta = 19.8\,°$ for NiP, $2\theta = 21°$ for Cu_3Pt, $2\theta = 15.92\,° \; and \; 22\,°$ for $Ni_{12}P_5$, and $2\theta = 26.1°$ for Cu.

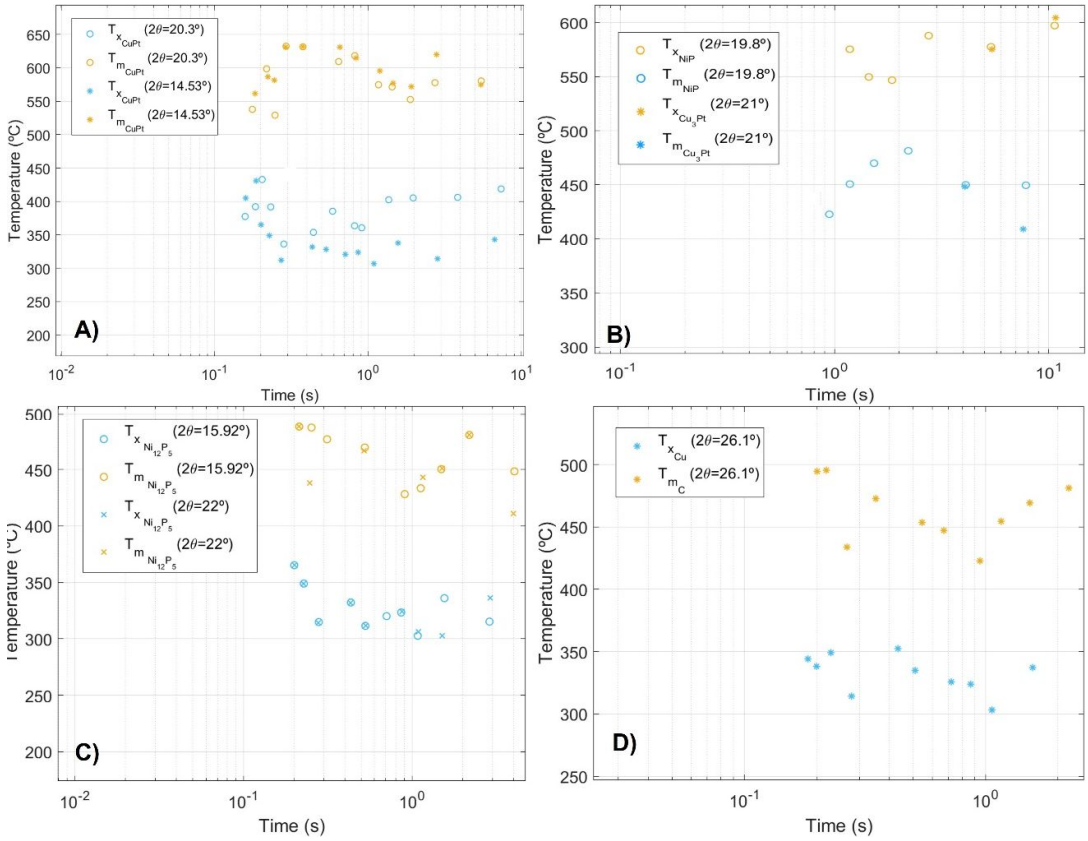

Figure 24. CHT diagrams of (a) CuPt, (b)Cu_3Pt, (c) $Ni_{12}P_5$ and (d) Cu phases obtained from XRD intensities.

As shown in Figure 24. c) and d), Ni-P systems with lower P-content have the lowest crystallization and melting temperatures, closely followed by Cu. Both phases present crystallization temperatures between 300 ºC and 350 ºC and melting temperatures around 450 ºC, matching with T_{x1} and T_{m1} in FDSC curves.

In contrast, the rest of phases present higher values of crystallization and melting temperatures. In the time range close to 10^{-1} s, when in the FDSC curves is possible to proceed to deconvolution, CuPt and Pt phases show crystallization temperatures around 400 ºC, being the first one with lower values. In contrast, NiP and Cu_3P, even thought it was only possible to distinguish their signal from the background at low heating rates, show higher crystallization temperatures compared to the rest (around 450 ºC). Thus, one can associate T_{x2} to CuPt, T_{x3} to Pt, T_{x4} to NiP/NiP_2, and T_{x5} to Cu_3Pt.

As the sample is subjected to non-isothermal methods of constant heating rates, one can study the phases kinetics through Kissinger equation (76). With this, the

activation energy (in kJ units) of a physical or chemical process, e.g., nucleation and growth of crystals, can be estimated as the slope of the straight line obtained when plotting $-ln\left(\Phi/T_p^2\right)$ versus $1000/RT_p$ (Kissinger plot). Being R the universal gas constant ($R = 8.315\, J \cdot K^{-1} \cdot mol^{-1}$), T_p the peak or onset temperatures (to find the growth or nucleation activation energy, respectively), and Φ the heating rate.

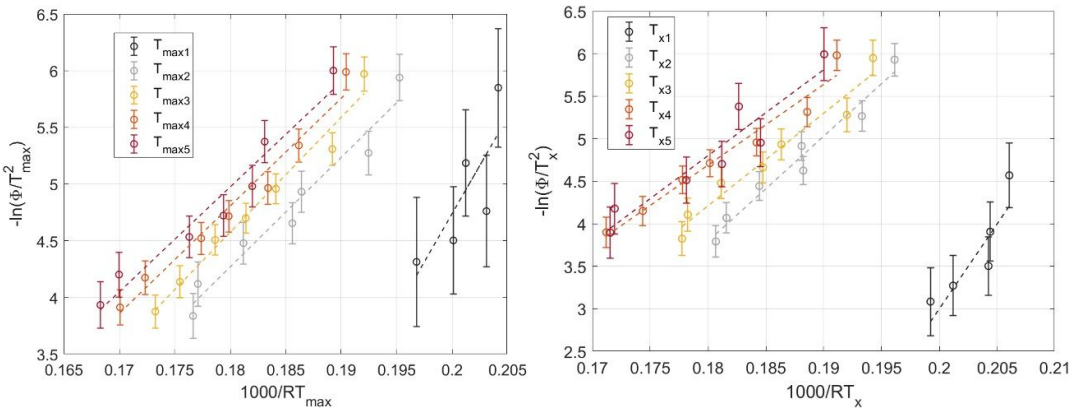

Figure 25. Kissinger plot for evaluating the different crystallizations energy of $Pt_{57.5}Cu_{14.7}Ni_{5.3}P_{22.5}$ in in-situ FDSC measurements, using the maximum (left) and onset (right) temperatures of the peaks.

The Kissinger plots for the peak and onset temperatures of each crystalline phase in the alloy are shown in Figure 25. These method leads to a nucleation activation energy of 199.69 ± 0.53 kJ/mol, 123.48 ± 0.35 kJ/mol, 108.83 ± 0.38 kJ/mol, 94.94 ± 0.33 kJ/mol, and 101.07 ± 0.57 kJ/mol for the phases $Ni_{12}P_5$, CuPt, Pt, NiP/NiP_2, and Cu_3Pt, respectievely. Similarly, we obtain a growth activation energy of 169.84 ± 0.74 kJ/mol, 96.55 ± 0.38 kJ/mol, 101.35 ± 0.27 kJ/mol, 94.88 ± 0.29 kJ/mol, and 92.51 ± 0.38 kJ/mol for the same phases.

As one can see, in every phase, the activation energy for nucleation is higher than the one for crystal growth. This indicates that the crystallization process is controlled by nuclei formation. This can be explained through the high heating and cooling rates employed, which reduce the absolute time for crystallization, and the small weight of the sample (in the order of nanograms). As the sample' size approaches the mean distance between nucleis, it would contain a reduced number of nucleation events (77).

In addition, these values could explain why $Ni_{12}P_5$ phase is not formed during quenching despite the fact that it shows the most displaced crystallization nose to short times in the CHT diagram (Figure 21). It is easy to notice that the activation energies for this phase practically double the others. Thus, a slow kinetics is associated to $Ni_{12}P_5$ phase, limiting the effective number of nucleation events in high cooling rates. In contrast, the low activation energy for Pt phase and its high element concentration in the alloy may result in a higher number of nucleation points that increases the probability of grow some crystallite even at high cooling rates (quenching).

4.2. Ex-situ FDSC experiments

The measured FDSC curves for four heating ramps in ex-situ conditions are shown in Figure 26. As we can observe, when no radiation is impinging, a continuous heat flow is measured by the FDSC device. This indicates that under these conditions the sample can cool to room temperature in quenching and follows the temperature program of Figure 14.a.

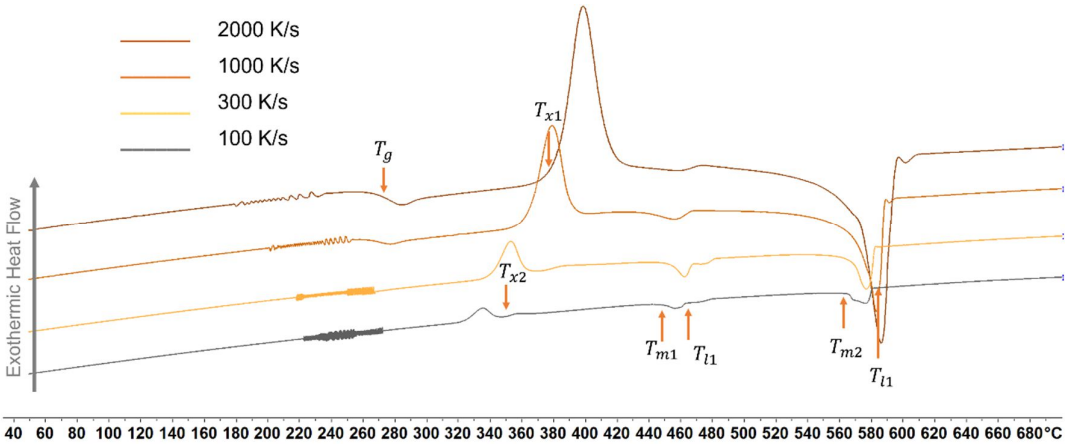

Figure 26. Ex-situ FDSC measurement of $Pt_{57.5}Cu_{14.7}Ni_{5.3}P_{22.5}$ at 2000, 1000, 300 and 100 Ks-1 with marked points of the glass transition temperature Tg, crystallization temperatures Tx, melting temperature Tm, and liquidus temperature Tl.

By direct analysis of Figure 26, a glass transition temperature is observed at temperatures near 270 ºC. After reaching the supercooled liquid state, the alloy experiences a crystallization phenomenon with high enthalpies for all heating rates. Then, a second crystallization peak is observed at 15-20 ºC above the first exothermic signal. This second crystallization will have a minor representation in the crystalline fraction of the metallic glass due to its small area in the heat flow

curve. In addition, for high heating rates its signal is practically overlapped with its melting peak, of onset and liquidus temperature denoted as T_{m1} and T_{l1} in Figure 26 (i.e., being close to its nose in the CHT diagram). Finally, at temperatures near 600 ºC one can observe a second endothermic peak corresponding to the melting of the primary phase. All characteristic temperatures for each heating rate are summarized in Table 2.

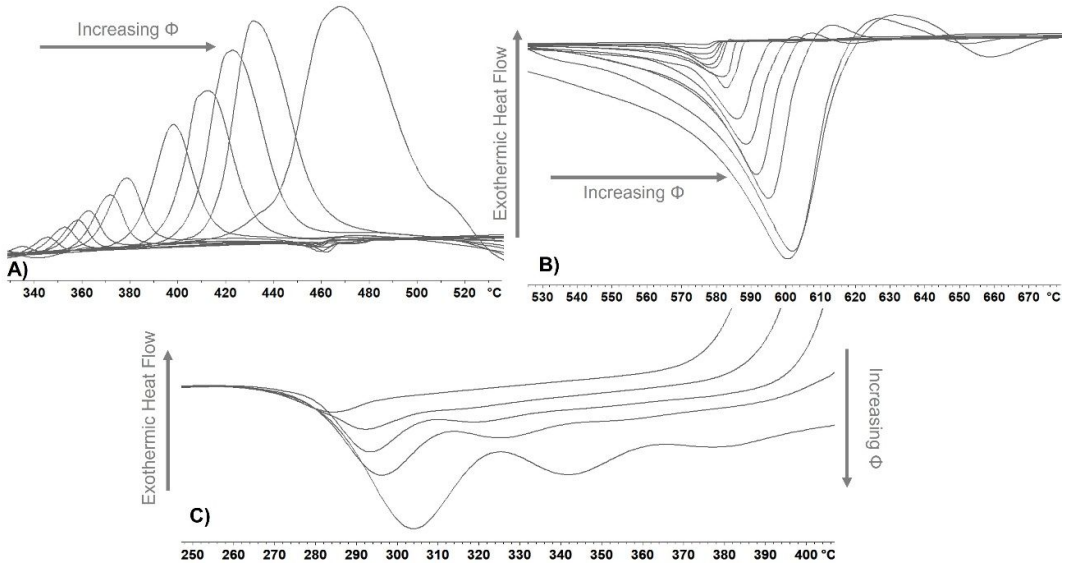

Figure 27. Overview of the ex-situ (a) crystallization, (b) melting peaks, and (c) glass transition of $Pt_{57.5}Cu_{14.7}Ni_{5.3}P_{22.5}$ for heating rates Φ between 50 - 10000 Ks^{-1}.

Figure 27 zooms in on the primary melting and crystallization peaks, as well as the glass transition temperature. Only one peak is observed in the crystallization (Figure 27.a), indicating the formation of a single crystalline phase. In addition, crystallization temperature increases with higher heating rates, broadening the super-cooled liquid region. In contrast, melting and glass transition temperatures appear to remain almost constant with heating rates. An enthalpy relaxation is found just after the glass transition temperature for all heating rates. Thus, the glassy state may fall to a more relaxed metastable valley in the potential landscape during heating below T_g. Then, when entering to the supercooled liquid state it absorbs heat in order to recover the initial state. A wave-like signal shadows this enthalpy relaxation at high heating rates. This is a common effect in FDSC experiments. By increasing the heating rate, the chip control has less accuracy when following the heat flow to the sample due to the dissipation/conduction of heat to the whole sample's thermal mass when it is too big. In addition, one should take into account that the jump of the sample from

the chip is also a common problem at high heating rates due to the accentuated thermal shock and thermal expansion of the chip's membrane.

Table 2. Summarized glass transition temperature, onset and peak temperatures of the different crystallizations and, melting and liquidus temperatures of the endothermic peaks of $Pt_{57.5}Cu_{14.7}Ni_{5.3}P_{22.5}$ *in ex-situ measurements.*

$\boldsymbol{Heating\ rate\ (K \cdot s^{-1})}$	$\boldsymbol{T_g \pm 1\ (K)}$	$\boldsymbol{T_{x1} \pm 1\ (K)}$	$\boldsymbol{T_{max1} \pm 1\ (K)}$	$\boldsymbol{T_{x2} \pm 1\ (K)}$	$\boldsymbol{T_{max2} \pm 1\ (K)}$	$\boldsymbol{T_{m1} \pm 1\ (K)}$	$\boldsymbol{T_{l1} \pm 1\ (K)}$	$\boldsymbol{T_{m2} \pm 1\ (K)}$	$\boldsymbol{T_{l2} \pm 1\ (K)}$
10000	286	426	457					556	606
7500	287	435	463					562	609
5000	286	414	430					566	602
4000	285	406	422					567	599
3000	287	398	413					567	597
2000	279	384	400					568	594
1000	272	367	381			439	468	574	590
750	258	361	375			438	467	568	588
500	261	353	366			438	467	569	586
400	264	349	362			449	465	569	585
300		346	356			457	471	569	584
200		339	350	367	377	455	470	569	584
100		329	339	355	361	451	467	567	583
50		327	330	342	348	458	466	567	581

With the values in Table 2 and knowing the relative time for each temperature with respect to the start of the corresponding heating ramp, one can draw the CHT diagram of the crystalline phases (Figure 28). As mentioned above, the glass transition temperature is mainly independent of the heating rate. The two crystalline phases that form during heating have their "C" curves one contained in the other. Thus, the T_{m1} will belong to the melting of a metastable phase that forms at lower heating rates.

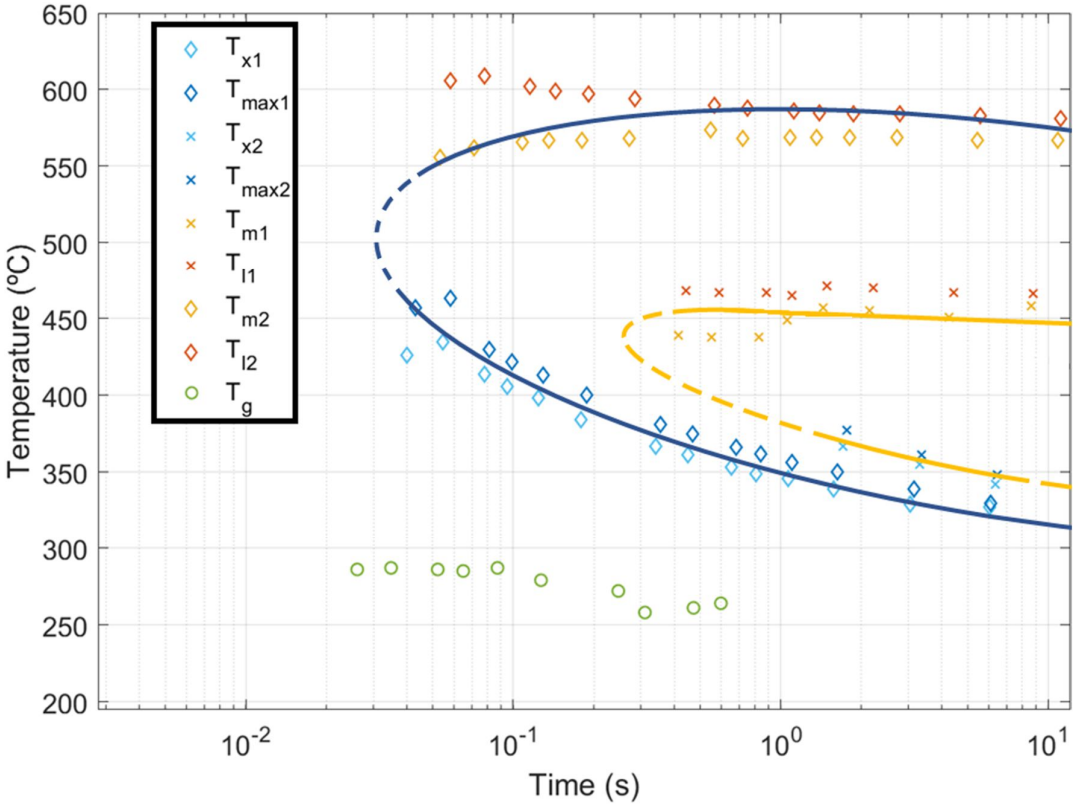

Figure 28. CHT diagram of $Pt_{57.5}Cu_{14.7}Ni_{5.3}P_{22.5}$ in ex-situ conditions.

In the same way as in the in-situ case, we can perform Kissinger plots to estimate the nucleation and growth activation energies of these two phases (Figure 29). This method leads to a growth activation energy of 129.70 ± 1.02 kJ/mol, and 149.61 ± 0.03 kJ/mol for the primary and metastable phases, respectievely. Similarly, we obtain a nucleation activation energy of 145.62 ± 1.11 kJ/mol, and 170.92 ± 0.04 kJ/mol for the same phases. As the activation energies for nucleation are higher than the ones for growth, the crystallization process would be controlled by nuclei formation.

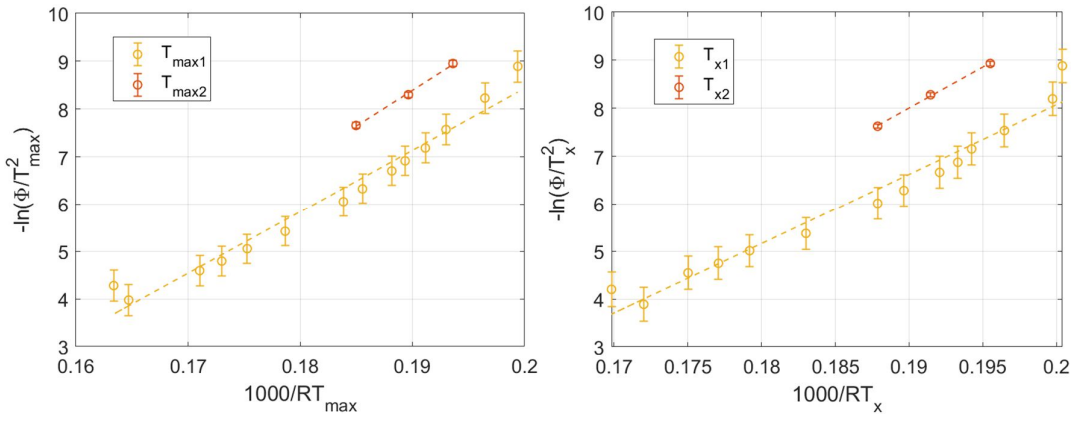

Figure 29. Kissinger plot for evaluating the primary (T_{max1}) and metastable (T_{max2}) crystallizations energy of $Pt_{57.5}Cu_{14.7}Ni_{5.3}P_{22.5}$ in ex-situ measurements, using the maximum (left) and onset (right) temperatures of the peaks.

4.3. Comparison between in-situ and ex-situ conditions. Effect of synchrotron radiation

After exposing the results obtained in the in-, and ex-situ FDSC, one can compare them in order to discern which is the effect of the beam. First, analysing the thermal transitions measured in both conditions during FDSC experiments, two main differences are found. Under the influence of X-rays, the crystallisation temperatures decrease compared to the ex-situ data, while the melting temperatures appear to remain unchanged. This causes the shift of the crystallization nose to lower times in in-situ measurements and decreases the Glass Forming Ability (GFA) of the alloy. The CHT diagrams for both in-situ and ex-situ measurements are shown together in Figure 30 to facilitate the comparison. A similar conclusion is extracted from the activation energies obtained through Kissinger method. In ex-situ measurements a higher growth activation energy is found compared with in-situ results. This agrees with the decrease in peak crystallization temperatures when X-rays are present in the thermal measurements.

Secondly, the most important difference between the two conditions is the detection of a more heterogeneous chemistry when X-rays are turned on. A total of six different crystalline phases were identified in the XRD pattern of the alloy during in-situ measurements and it was possible to assign each one of these to a thermal transition in the FDSC curves. In contrast, for ex-situ measurements only two phases were observed as unimodal crystallization peaks were measured in the heat flow curves of FDSC.

To explain the above results, we propose the next hypothesis. During in-situ measurements, X-rays are highly absorbed by the gold chip. This is heated and in turn prevents the sample from cooling to temperatures below T_g. This aging in the supercooled liquid state, allows atomic rearrangements and relaxation of internal stresses that facilitate the system to explore different minima in the potential landscape and to nucleate new metastable phases depending on the local chemistry.

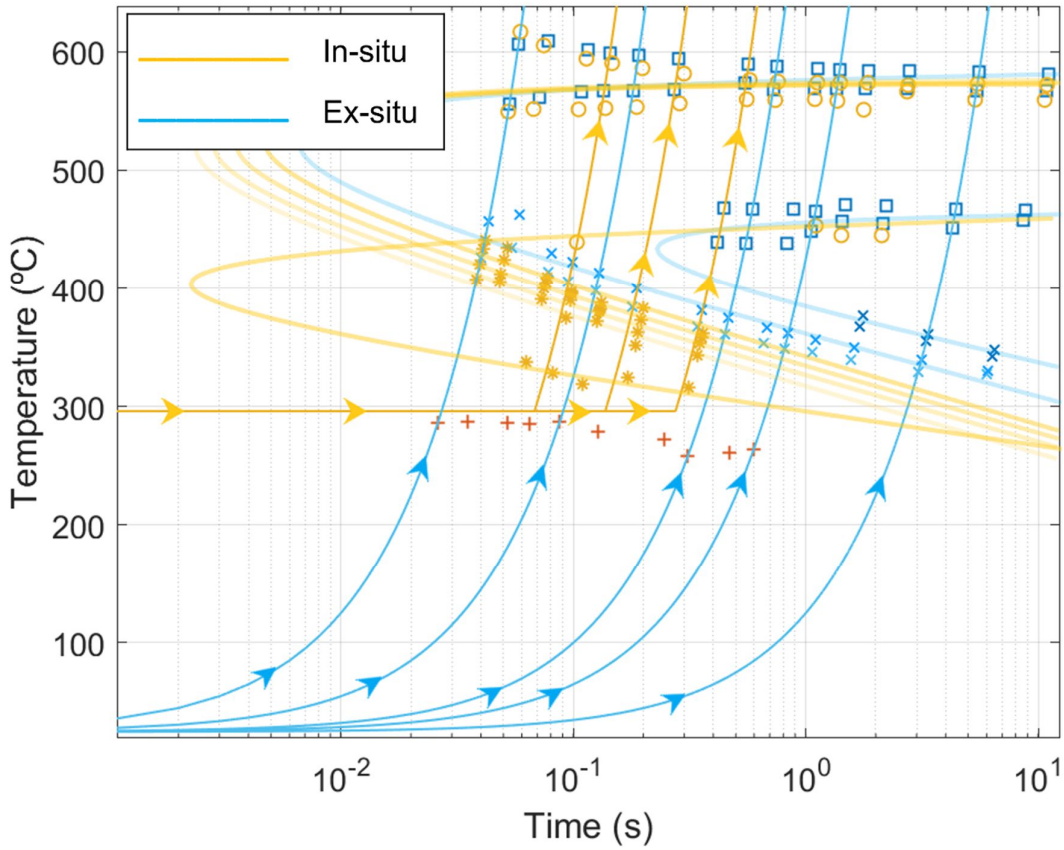

Figure 30. Complete CHT for of $Pt_{57.5}Cu_{14.7}Ni_{5.3}P_{22.5.}$ Yellow asterisks and circles correspond to crystallization and melting of phases in in-situ conditions. Blue crosses and squares correspond to crystallization and melting of phases in ex-situ conditions. Translucid lines represent the "C" shape curves for each phase. Solid lines with arrows indicate different heating segments. For in-situ segments, they have a prior isothermal close to 296 ºC. Red crosses correspond to glass transition temperature, obtained in ex-situ measurements.

The first fact that contributes to the veracity of this theory is the good agreement between gold's wavevector evolution and the modified temperature program with the heating segments starting not from room temperature but from a temperature around 296 ºC (Figure 30). With this, one can assume that the sample is being somehow heated by the X-rays. If one checks the absorption spectrum of gold (Figure 31) one may notice that the X-ray wavelength of 13.1 keV employed during in-situ measurements lays in the L-edge region, between L_{II} (13733.6 ± 0.3 eV), and L_{III} (11918.7 ± 0.3 eV) (78). Thus, it can be assumed that this heating is caused by the absorption of X-rays by the chip and the subsequent conduction of heat from the chip to the sample, rather than by the direct absorption of radiation by the sample.

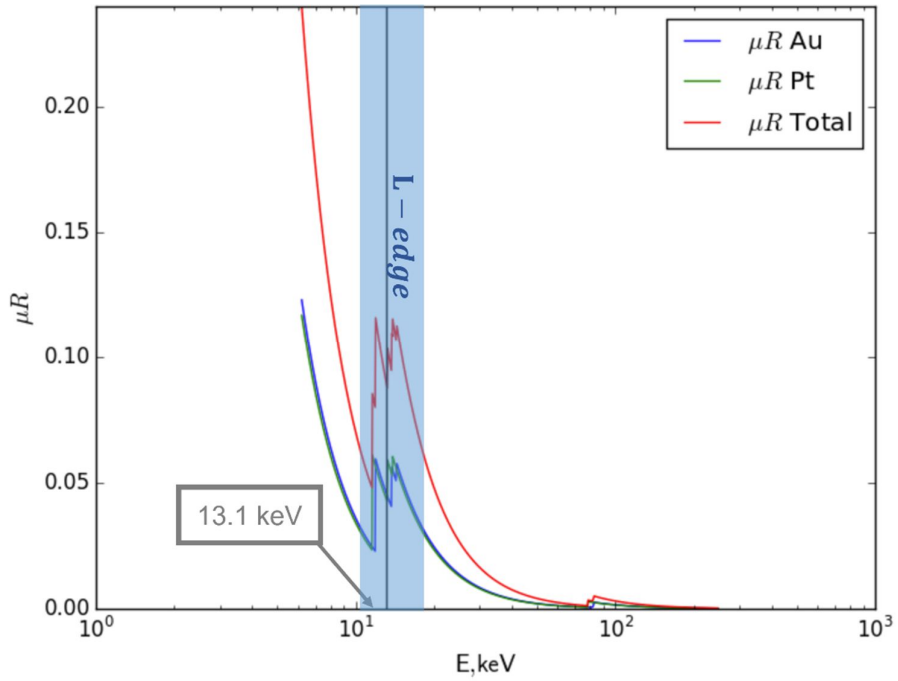

Figure 31. X-ray absorption for gold and platinum as function of photon energy. The x-ray beam of 13.1 keV employed in characterization lay in the chips L-edge energies. Data extracted from Argonne National Laboratory (79).

In order to determine whether the X-ray effect was simply the annealing of the sample by absorption of the chip, or whether there was some other effect resulting from the direct interaction between the photons and the alloy, the modified temperature programme is repeated with isotherms at 296ºC in the FDSC, but this time without X-ray exposure.

As shown in Figure 32, when the heating step starts from an isotherm at 296ºC, above the calorimetric glass transition temperature, a higher number of crystallization and melting events occur compared with the flow curves of the tests without annealing steps. For example, in the heating rate of 4000 Ks^{-1} a pronounced melting at T_m=552 ºC is measured for the annealed sample while it is practically negligible for the as-quenched one. In addition, one can see how for all heating rates, the peaks in the annealed samples are broader and more pronounced than in the as-quenched measurements. Moreover, a shift of the onset of crystallisation to lower temperatures is observed in the experiments where pre-annealing is carried out. This indicates that the annealing above T_g facilitates the crystallization from the supercooled liquid state. However, unimodal crystallization peaks are mainly displayed in this test, contrary to the in-situ

results, where the primary crystallization peak clearly show rich phase diversity. This fact suggests that exposing the sample to energetic X-rays has another effect apart from annealing.

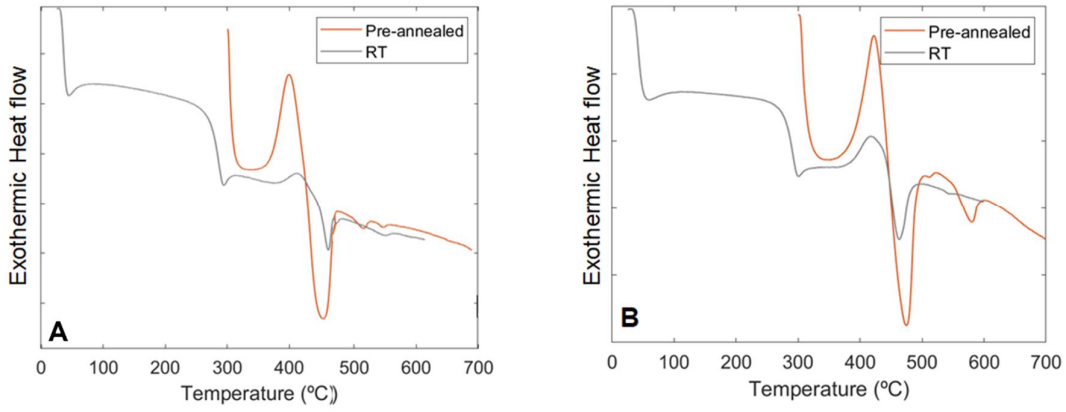

Figure 32. FDSC curves of $Pt_{57.5}Cu_{14.7}Ni_{5.3}P_{22.5}$ starting from RT (grey curves) or after an annealing at 296 ºC (red curves). Heating rates of (a) 2000 and (b) 4000 Ks^{-1}.

Some authors studied the effect of X-ray exposition over metallic glasses and amorphous solids. Even thought, X-ray and ion irradiation have been insufficient to induce crystallization in most of the cases, they appear to be able to increase the disordering in the glassy state. Thompson et al. irradiated Zr-Ni-Al metallic glass with 12 MeV Ni^{4+} ions observing a significant contraction of the material attributed to the radiation induced liquid-like flow of the glass (80). In another study, Feldman et al. considered the influence of X-rays during the crystallization process of amorphous $BaTiO_3$ (81). They observed an increase in the number of crystallization nucleation sites, resulting into a finer grain size distribution. This was firstly explained due to the increase in atomic vibrational amplitudes when radiation is involved. Thanks to the increased mobility of the elements that make up the metallic glass, the diffusion of light atoms is promoted and the probability of the formation of a supercritical nucleus is increased. In addition, the formation of dangling bonds and free radicals, mainly in the sample' surface, increases the migration of atomic species and reduces the crystallization activation energy during heating.

From Equation 12 we know that the nucleation rate is inversely proportional to the viscosity and to the exponential of the cubic surface energy. Thus, the increase in disordering introduced by the X-rays will lead to a higher number of

nucleation events in the supercooled liquid state. Moreover, this vibrational effect reduces the entropy difference between the supercooled liquid state and the crystalline phase as for liquids the entropy is mainly contribution of the configurational states while for crystals it comes from vibrational modes: $\Delta S_f \sim S_{liq}^{conf} - S_{liq}^{vib}$. Both effects will shift the CHT nose to lower times and temperatures.

Thus, the radiation interaction with the alloy increases element diffusivities and heterogeneity of phases during the crystallization process. However, the annealing coming from the chip also contribute to the crystallization of the supercooled liquid before it can reach the metastable equilibrium. It has been observed that annealing generates the relaxation of internal stresses and the loss of thermal memory. This will derive in the system's fall to the upper equilibrium curve. In contrast, if the system is continuously heated, the available time for atomic rearrangement is reduced and the glass meets its corresponding metastable equilibrium at higher temperatures. The relaxation process is considered to involve an avalanche-like microcollapse of particle groups (82).

The above-mentioned dynamics could be explained by Mode Coupling Theory (MCT) and the Entropy Catastrophe. The loss in excess entropy (or fusion entropy, ΔS_f) upon approaching the glass transition temperature is one of the most relevant features during undercooling. Kauzmann showed that this entropy could turn negative above a temperature T_k, having a greater entropy for the equilibrium crystal than for its liquid. This is known as Kauzmann's entropy catastrophe paradox. To prevent such paradox, Kauzmann proposed that the supercooled liquid should crystallize at temperatures below T_k, since the activation energy for nucleation tends to be similar to that for structural relaxation. However, the liquid can equilibrate when one considers the effect atomic diffusion. This is because of the highly collective atomic diffusion in the supercooled liquid, where atoms are trapped in cages formed by their neighbours and leads to the freezing of a liquidlike motion (83). In other words, the crystallization time exceeds the structural relaxation time. However, this assumption is only valid when Stokes-Einstein (S-E) equation (Equation 11) applies, i.e., when relaxation time is determined only by translational diffusion. S-E equation breakdown is well-known in the supercooled liquid regime for heavy

components that may form slow subsystems. Thus, a component decoupling is observed. Light elements will dominate diffusion and crystallization timescales, while slowest regions will control structural relaxation and viscous flow. In consequence, the crystallization process is shifted to shorter times and intersects the structural relaxation time above T_k, at the "lower limit of metastability". Then, annealing a metallic glass below this limit temperature prevents the supercooled liquid to reach the metastable equilibrium and initiates its crystallization.

To sum up, when performing in-situ measurement one should consider the influence of the synchrotron radiation and do not interpret the results as "real" but as "radiation-influenced". Also, when one is aware of the implications of exposing nanosized samples to X-rays, they can be used to its advantage. For nanostructured samples that follows the criteria of "the smaller the better" (84) in metallic glasses, one can introduce radiation-induced disordering to reduce strain localization and promote liquid-like behaviour of the material under loading.

5. Summary

- Flash DSC measurements of $Pt_{57.5}Cu_{14.7}Ni_{5.3}P_{22.5}$ were performed under in-situ and ex-situ conditions. No heat flow is observed below 296 ºC under in situ conditions, but multimodal crystallisation events are observed at higher temperatures. The glass transition temperature is observed to be around 270 ºC in ex-situ measurements and unimodal peaks predominate, indicating the reduced number of crystalline phases compared to in-situ experiments.

- A script for the evaluation of synchrotron data was developed. The chip' signal was identified and used to determine the actual temperature profile in in-situ measurements.

- Synchrotron X-ray diffraction patterns show the crystallisation of six distinct phases under in-situ conditions. Metallic Pt phase observed even after quenching from liquid state. Within FDSC cycles, an incompletely amorphous sample is achieved. At higher temperatures the matrix becomes depleted of Cu and P as phases with higher contents of these elements nucleate.

- Thermal transformations in ex-situ measurements show higher onset temperatures and activation energies compared to in-situ conditions.

- The synchrotron measurements combined with FDSC clearly show annealing steps in front of the heating segments when X-rays are switched on. By replicating these temperature conditions, it was shown that in addition to the heating of the chip, the X-ray interaction with the BMG modifies its crystallisation kinetics.

6. Conclusions

In this work, the effects of synchrotron radiation during in-situ flash DSC experiments on $Pt_{57.5}Cu_{14.7}Ni_{5.3}P_{22.5}$ alloys have been studied. The metallic glass was produced by suction casting and small samples were scraped off and placed in high-temperature chips for measurement in the FDSC. These FDSC measurements were performed in a synchrotron facility to study the phase evolution of the alloy during the temperature programs. During the influence of X-rays, the samples showed an enriched chemical heterogeneity and a nun-heat flow for temperatures below 296 °C. This was in contrast to the ex-situ FDSC, which showed a higher activation energy for the crystallisation events. New FDSC measurements were performed in a Flash DSC 2+ instrument to clarify the effect of X-rays.

With the results obtained from the different characterisations, we observe a non-negligible effect of X-rays on the kinetics of the alloy. Our hypothesis is that the interaction between the synchrotron radiation and the sample is twofold. Firstly, because the radiation wavelength is in the L-edge of the chip's membrane (gold coating) and is highly focused, it heats the membrane and prevents the metallic glass from cooling to temperatures below 296 °C during quenching. The result is an anneal in the supercooled liquid state of the alloy between the heating segments of the FDSC program. Secondly, the X-rays increase the vibrational amplitudes of the elements of the alloy in this supercooled liquid, reducing its viscosity. The combination of these two effects leads to increased mobility of light elements and relaxation of internal stresses in the alloy, facilitating crystallisation events in the amorphous matrix.

Results obtained from in-situ characterisation using high energy beams on samples of reduced weight should be considered as "radiation-influenced".

7. References

1. Kittel C. Introduction to Solid State Physics. 8th ed. John Wiley & Sons; 2004. ISBN: 9780471415268.

2. Colomban P. Glass , pottery and enamelled objects : identification of their technology and origin To cite this version : HAL Id : hal-03622849. 2022.

3. Chittick RC, Alexander JH, Sterling HF. The Preparation and Properties of Amorphous Silicon. J Electrochem Soc [Internet]. 1969;116(1):77. Available from: https://dx.doi.org/10.1149/1.2411779

4. Adler D. Amorphous semiconductors. C R C Crit Rev Solid State Sci [Internet]. 1971;2(3):317–465. Available from: https://doi.org/10.1080/10408437108243545

5. Duwez P. Metallic glasses — a new class of materials: their scientific and industrial importance. Proc Indian Acad Sci Sect C Eng Sci [Internet]. 1979;2(1):117–32. Available from: https://doi.org/10.1007/BF02899759

6. BERNAL JD. A Geometrical Approach to the Structure Of Liquids. Nature [Internet]. 1959;183(4655):141–7. Available from: https://doi.org/10.1038/183141a0

7. Scott GD, Charlesworth AM, Mak MK. On the Random Packing of Spheres. J. Chem. Phys. 1965 Jan; 40(2):611-612. Available from: https://doi.org/10.1063/1.1725176

8. Ramakrishnan TV. Liquid to Solid Transition. Mater Sci Forum. 1985;3:57–68. Available from: https://doi.org/10.4028/www.scientific.net/MSF.3.57

9. Gibbs JH, Dimarzio EA. Nature of the Glass Transition and the Glassy State. J. Chem. Phys. 1958;28(3):373-383. Available from: https://doi.org/10.1063/1.1744141

10. Degiuli E. Field Theory for Amorphous Solids. Phys Rev Lett [Internet]. 2018;121(11):118001. Available from: https://doi.org/10.1103/PhysRevLett.121.118001

11. Falk ML, Langer JS. Dynamics of viscoplastic deformation in amorphous solids. Phys Rev E [Internet]. 1998 Jun;57(6):7192–205. Available from: https://link.aps.org/doi/10.1103/PhysRevE.57.7192

12. Cohen MH, Turnbull D. Molecular Transport in Liquids and Glasses. J Chem Phys [Internet]. 2004;31(5):1164–9. Available from: https://doi.org/10.1063/1.1730566

13. Gonon M. Case Studies in the X-ray Diffraction of Ceramics. In: Pomeroy M, editor. Encyclopedia of Materials: Technical Ceramics and Glasses [Internet]. Oxford: Elsevier; 2021. p. 560–77. Available from: https://doi.org/10.1016/B978-0-12-818542-1.00005-9

14. Sharma A, Hesterberg D. 9 - Synchrotron radiation-based spatial methods in environmental biogeochemistry. In: Duarte RMBO, Duarte AC, editors. Multidimensional Analytical Techniques in Environmental Research [Internet]. Elsevier; 2020. p. 231–65. Available from: https://doi.org/10.1016/B978-0-12-818896-5.00009-0

15. Rathmann T, Petersen H, Reichle S, Schmidt W, Amrute AP, Etter M, et al. In situ synchrotron x-ray diffraction studies monitoring mechanochemical reactions of hard materials: Challenges and limitations. Rev Sci Instrum [Internet]. 2021;92(11). Available from: https://doi.org/10.1063/5.0068627

16. KLEMENT W, WILLENS RH, DUWEZ POL. Non-crystalline Structure in Solidified Gold–

Silicon Alloys. Nature [Internet]. 1960;187(4740):869–70. Available from: https://doi.org/10.1038/187869b0

17. Fulchiron R, Belyamani I, Otaigbe JU, Bounor-Legaré V. A simple method for tuning the glass transition process in inorganic phosphate glasses. Sci Rep [Internet]. 2015;5(1):8369. Available from: https://doi.org/10.1038/srep08369

18. Altounian Z, Guo-hua T, Strom-Olsen JO. Crystallization characteristics of Ni-Zr metallic glasses from Ni20Zr80 to Ni70Zr30. J Appl Phys [Internet]. 1983;54(6):3111–6. Available from: https://doi.org/10.1063/1.332465

19. Tanner LE, Ray R. Metallic glass formation and properties in Zr and Ti alloyed with Be—I the binary Zr-Be and Ti-Be systems. Acta Metall [Internet]. 1979;27(11):1727–47. Available from: https://doi.org/10.1016/0001-6160(79)90087-7

20. Hasegawa R, Ray R. Iron-boron metallic glasses. J Appl Phys [Internet]. 2008;49(7):4174–9. Available from: https://doi.org/10.1063/1.325328

21. Inoue A. Stabilization of metallic supercooled liquid and bulk amorphous alloys. Acta Mater [Internet]. 2000;48(1):279–306. Available from: https://doi.org/10.1016/S1359-6454(99)00300-6

22. Shechtman D, Blech I, Gratias D, Cahn JW. Metallic Phase with Long-Range Orientational Order and No Translational Symmetry. Phys Rev Lett [Internet]. 1984 Nov;53(20):1951–3. Available from: https://link.aps.org/doi/10.1103/PhysRevLett.53.1951

23. Gibbs JH, DiMarzio EA. Nature of the Glass Transition and the Glassy State. J Chem Phys [Internet]. 2004;28(3):373–83. Available from: https://doi.org/10.1063/1.1744141

24. Stillinger FH, Weber TA. Hidden structure in liquids. Phys Rev A [Internet]. 1982 Feb;25(2):978–89. Available from: https://doi.org/10.1103/PhysRevA.25.978

25. Stillinger FH. A Topographic View of Supercooled Liquids and Glass Formation. Science (80-) [Internet]. 1995;267(5206):1935–9. DOI: 10.1126/science.267.5206.1935

26. Cohen MH, Turnbull D. Molecular transport in liquids and glasses. J Chem Phys. 1959;31(5):1164–9. Available from: https://doi.org/10.1063/1.1730566

27. Cohen MH, Grest GS. Liquid-glass transition, a free-volume approach. 1979;20(3):1077–98. Available from: https://doi.org/10.1103/PhysRevB.20.1077

28. Fox TGJ, Flory PJ. Further Studies on the Melt Viscosity of Polyisobutylene. J Phys Chem [Internet]. 1951 Feb 1;55(2):221–34. Available from: https://doi.org/10.1021/j150485a010

29. Fox Thomas G. J, Flory PJ. Second-Order Transition Temperatures and Related Properties of Polystyrene. I. Influence of Molecular Weight. J Appl Phys [Internet]. 2004;21(6):581–91. Available from: https://doi.org/10.1063/1.1699711

30. Argon AS, Kuo HY. Plastic flow in a disordered bubble raft (an analog of a metallic glass). Mater Sci Eng [Internet]. 1979;39(1):101–9. Available from: https://doi.org/10.1016/0025-5416(79)90174-5

31. Doolittle AK. Studies in Newtonian Flow. III. The Dependence of the Viscosity of Liquids on Molecular Weight and Free Space (in Homologous Series). J Appl Phys [Internet]. 2004 Jun 15;23(2):236–9. Available from: https://doi.org/10.1063/1.1702182

32. Spieckermann F, Daniel Ş, Soprunyuk V, Kerber MB, Bednar J, Schökel A, et al. Structure-

dynamics relationships in cryogenically deformed bulk metallic glass. 2022;1–9. Available from: https://doi.org/10.1038/s41467-021-27661-2

33. Küchemann S, Maaß R. Gamma relaxation in bulk metallic glasses. Scr Mater [Internet]. 2017;137:5–8. Available from: https://doi.org/10.1016/j.scriptamat.2017.04.034

34. Wang Q, Liu JJ, Ye YF, Liu TT, Wang S, Liu CT, et al. Universal secondary relaxation and unusual brittle-to-ductile transition in metallic glasses. Mater Today [Internet]. 2017;20(6):293–300. Available from: https://doi.org/10.1016/j.mattod.2017.05.007

35. Suryanarayana C, Inoue A. Bulk Metallic Glasses. 2nd ed. CRC Press. Available from: https://doi.org/10.1201/9781315153483

36. Turnbull D. Kinetics of Heterogeneous Nucleation. J Chem Phys [Internet]. 2004;18(2):198–203. Available from: https://doi.org/10.1063/1.1747588

37. Herlach DM. Non-equilibrium solidification of undercooled metallic metls. Mater Sci Eng R Reports [Internet]. 1994;12(4):177–272. Available from: https://doi.org/10.1016/0927-796X(94)90011-6

38. Uhlmann DR. A kinetic treatment of glass formation. J Non Cryst Solids [Internet]. 1972;7(4):337–48. Available from: https://doi.org/10.1016/0022-3093(72)90269-4

39. Schawe JEK, Löffler JF. Existence of multiple critical cooling rates which generate different types of monolithic metallic glass. Nat Commun [Internet]. 2019;10(1):1337. Available from: https://doi.org/10.1038/s41467-018-07930-3

40. Barandiarán JM, Colmenero J. Continuous cooling approximation for the formation of a glass. J Non Cryst Solids [Internet]. 1981;46(3):277–87. Available from: https://doi.org/10.1016/0022-3093(81)90006-5

41. Gross O. Precious metal based bulk glass-forming liquids. 2018. DOI: 10.22028/D291-27993

42. Takeuchi A, Inoue A. Classification of Bulk Metallic Glasses by Atomic Size Difference, Heat of Mixing and Period of Constituent Elements and Its Application to Characterization of the Main Alloying Element. Mater Trans. 2005;46(12):2817–29. Available from: https://doi.org/10.2320/matertrans.46.2817

43. Turnbull D. Under what conditions can a glass be formed? Contemp Phys [Internet]. 1969;10(5):473–88. Available from: https://doi.org/10.1080/00107516908204405

44. Egami T, Waseda Y. Atomic size effect on the formability of metallic glasses. J Non Cryst Solids [Internet]. 1984;64(1):113–34. Available from: https://doi.org/10.1016/0022-3093(84)90210-2

45. INOUE A. Stabilization of Supercooled Liquid and Opening-up of Bulk Glassy Alloys. Proc Japan Acad Ser B. 1997;73(2):19–24. Available from: https://doi.org/10.2183/pjab.73.19

46. Chen HS. Glassy metals. Reports Prog Phys. 1980;43(4):353–432. DOI: 10.1088/0034-4885/43/4/001

47. Kawamura Y, Nakamura T, Kato H, Mano H, Inoue A. Newtonian and non-Newtonian viscosity of supercooled liquid in metallic glasses. Mater Sci Eng A [Internet]. 2001;304–306:674–8. Available from: https://doi.org/10.1016/S0921-5093(00)01562-8

48. Padmanabhan J, Kinser ER, Stalter MA, Duncan-Lewis C, Balestrini JL, Sawyer AJ, et al. Engineering Cellular Response Using Nanopatterned Bulk Metallic Glass. ACS Nano

[Internet]. 2014 May 27;8(5):4366–75. Available from: https://doi.org/10.1021/nn501874q

49. Bera S, Sarac B, Balakin S, Ramasamy P, Stoica M, Calin M, et al. Micro-patterning by thermoplastic forming of Ni-free Ti-based bulk metallic glasses. Mater Des [Internet]. 2017;120:204–11. Available from: https://doi.org/10.1016/j.matdes.2017.01.080

50. Inoue A, Takeuchi A. Recent Progress in Bulk Glassy Alloys. Mater Trans. 2002;43(8):1892–906. DOI: 10.2320/matertrans.43.1892

51. Haruyama O, Kimura HM, Inoue A. Thermal Stability of Zr-Based Glassy Alloys Examined by Electrical Resistance Measurement. Mater Trans JIM. 1996;37(12):1741–7. Available from: https://doi.org/10.2320/matertrans1989.37.1741

52. Herzer G. Grain size dependence of coercivity and permeability in nanocrystalline ferromagnets. IEEE Trans Magn. 1990;26(5):1397–402. Available from: http://dx.doi.org/10.1109/20.104389

53. Chen HS, Miller CE. Centrifugal spinning of metallic glass filaments. Mater Res Bull [Internet]. 1976;11(1):49–54. Available from: https://doi.org/10.1016/0025-5408(76)90213-0

54. Liang X, Chen J, Mora M, Urdaneta J, Zeng Q. Effect of Precipitation on the Hardness of Ternary Metallic Glass. Adv Mater Phys Chem. 2017;07:255–62. DOI: 10.4236/ampc.2017.76020

55. Huang L, Wang HY, Qiu F, Jiang QC. Synthesis of dense ceramic particulate reinforced composites from Ni–Ti–C, Ni–Ti–B, Ni–Ti–B4C and Ni–Ti–C–B systems via the SHS reaction, arc melting and suction casting. Mater Sci Eng A [Internet]. 2006;422(1):309–15. Available from: https://doi.org/10.1016/j.msea.2006.02.019

56. Lashgari HR, Ferry M, Li S. Additive manufacturing of bulk metallic glasses: Fundamental principle, current/future developments and applications. J Mater Sci Technol [Internet]. 2022;119:131–49. Available from: https://doi.org/10.1016/j.jmst.2021.09.068

57. Pauly S, Löber L, Petters R, Stoica M, Scudino S, Kühn U, et al. Processing metallic glasses by selective laser melting. Mater Today [Internet]. 2013;16(1):37–41. Available from: https://doi.org/10.1016/j.mattod.2013.01.018

58. Chen M. A brief overview of bulk metallic glasses. NPG Asia Mater [Internet]. 2011;3(9):82–90. Available from: https://doi.org/10.1038/asiamat.2011.30

59. Morrison ML, Buchanan RA, Leon R V., Liu CT, Green BA, Liaw PK, et al. The electrochemical evaluation of a Zr-based bulk metallic glass in a phosphate-buffered saline electrolyte. J Biomed Mater Res - Part A. 2005;74(3):430–8. DOI: 10.1002/jbm.a.30361

60. Russew K, Stojanova L, Russew K, Stojanova L. Production, Properties and Applications of Glassy Metals. Springer; 2016. Available from: https://doi.org/10.1007/978-3-662-47882-0

61. Saotome Y, Imai K, Shioda S, Shimizu S, Zhang T, Inoue A. The micro-nanoformability of Pt-based metallic glass and the nanoforming of three-dimensional structures. Intermetallics [Internet]. 2002;10(11):1241–7. Available from: https://doi.org/10.1016/S0966-9795(02)00135-8

62. Schroers J, Johnson WL. Highly processable bulk metallic glass-forming alloys in the Pt–

Co–Ni–Cu–P system. Appl Phys Lett [Internet]. 2004;84(18):3666–8. Available from: https://doi.org/10.1063/1.1738945

63. Schmitt LY, Neuber N, Eisenbart M, Cifci L, Gross O, Klotz UE, et al. Study on technical parameters and suitability of Pt-based metallic glasses for jewellery applications. Vol. 44, Johnson Matthey Technology Review. 2022. 0–36 p. Available from: https://doi.org/10.1595/205651323X16577027080875

64. Höhne, GWH; Hemminger, WF; Flammersheim H. Differential scanning calorimetry. Springer Berlin, Heidelberg. Springer; 2003. Available from: https://doi.org/10.1007/978-3-662-06710-9

65. Schick, Christoph ; Mathot V. Fast Scanning Calorimetry. 1st ed. Springer Cham; 2016. ISBN: 978-3319313276

66. Xensor Integration. Calorimeter Chips [Internet]. [cited 2023 May 22]. Available from: https://xensor.nl/products/calorimeter-chips

67. Schajer GS. Practical residual stress measurement methods. John Wiley & Sons; 2013. ISBN: 9781118342374

68. Ashiotis G, Deschildre A, Nawaz Z, Wright JP, Karkoulis D, Picca FE, et al. The fast azimuthal integration Python library: {\it pyFAI}. J Appl Crystallogr [Internet]. 2015;48(2):510–9. Available from: https://doi.org/10.1107/S1600576715004306

69. Keshavlal Patel V. Lattice constants, thermal expansion coefficients, densities, and imperfections in gold and the alpha-phase of the gold-indium system. 1967; Available from: http://scholarsmine.mst.edu/masters_theses/6876

70. Uddin J. Terahertz multispectral imaging for the analysis of gold nanoparticles' size and the number of unit cells in comparison with other techniques. Int J Biosens Bioelectron. 2018;4(3):159–64. DOI: 10.15406/ijbsbe.2018.04.00118

71. Ketkaew J, Chen W, Wang H, Datye A, Fan M, Pereira G, et al. Mechanical glass transition revealed by the fracture toughness of metallic glasses. Nat Commun [Internet]. 2018;9(1):3271. Available from: https://doi.org/10.1038/s41467-018-05682-8

72. Davoodi E. The influence of loading on crystallization behavior of bulk metallic glasses. Texas Tech University; 2017. Available from: http://hdl.handle.net/2346/72652

73. Li D, Senevirathne K, Aquilina L, Brock SL. Effect of Synthetic Levers on Nickel Phosphide Nanoparticle Formation: Ni5P4 and NiP2. Inorg Chem [Internet]. 2015 Aug 17;54(16):7968–75. Available from: https://doi.org/10.1021/acs.inorgchem.5b01125

74. J.N. B, Rajam KS. Electroless deposition and characterization of high phosphorus13; Ni-P-Si3N4 composite coatings. Int J Electrochem Sci. 2007;2.

75. Schurmans M, Luyten J, Creemers C, Declerck R, Waroquier M. Surface segregation in CuPt alloys by means of an improved modified embedded atom method. Phys Rev B [Internet]. 2007 Nov;76(17):174208. Available from: https://link.aps.org/doi/10.1103/PhysRevB.76.174208

76. Kissinger HE. Variation of peak temperature with heating rate in Differential Thermal Analysis. J Res Natl Bur Stand (1934). 1956;57(4):217. Available from: http://dx.doi.org/10.6028/jres.057.026

77. Sohn S, Xie Y, Jung Y, Schroers J, Cha JJ. Tailoring crystallization phases in metallic glass nanorods via nucleus starvation. Nat Commun [Internet]. 2017;8(1):1980. Available

from: https://doi.org/10.1038/s41467-017-02153-4

78. BEARDEN JA, BURR AF. Reevaluation of X-Ray Atomic Energy Levels. Rev Mod Phys [Internet]. 1967;39(1):125–42. Available from: https://link.aps.org/doi/10.1103/RevModPhys.39.125

79. Argonne National Laboratory. X-ray Absorption [Internet]. [cited 2023 May 22]. Available from: https://11bm.xray.aps.anl.gov/absorb/absorb.php

80. Thompson RL, Wang YQ, Greer JR. Irradiation enhances strength and deformability of nano-architected metallic glass. Adv Eng Mater. 2018;20(4):1–11. Available from: https://doi.org/10.1002/adem.201701055

81. Feldman Y, Lyahovitskaya V, Leitus G, Lubomirsky I, Wachtel E, Bushuev VA, et al. X-ray initiation of nonthermal growth of single crystal pyramids in amorphous barium titanate. Appl Phys Lett [Internet]. 2009;95(5). Available from: https://doi.org/10.1063/1.3200231

82. Ruta B, Chushkin Y, Monaco G, Cipelletti L, Pineda E, Bruna P, et al. Atomic-Scale Relaxation Dynamics and Aging in a Metallic Glass Probed by X-Ray Photon Correlation Spectroscopy. Phys Rev Lett [Internet]. 2012 Oct;109(16):165701. Available from: https://link.aps.org/doi/10.1103/PhysRevLett.109.165701

83. Bartsch A, Rätzke K, Meyer A, Faupel F. Dynamic Arrest in Multicomponent Glass-Forming Alloys. Phys Rev Lett [Internet]. 2010 May;104(19):195901. Available from: https://link.aps.org/doi/10.1103/PhysRevLett.104.195901

84. Kumar G, Desai A, Schroers J. Bulk metallic glass: The smaller the better. Adv Mater. 2011;23(4):461–76. DOI: 10.1002/adma.201002148

Appendix

Recording of XRD peaks vs. frame (through Python 3)

In [2]:

```
import matplotlib.pyplot as plt
import numpy as np
import statistics
import scipy
from scipy import signal
from scipy import sparse
from scipy.sparse.linalg import spsolve
import csv
import h5py
import os
import sys
import glob
from scipy.signal import find_peaks
```

In [3]:

```
filename="./data/PtBMG_1_CHT_proc.h5"
```

In [4]:

```
with h5py.File(filename, "r") as f:
    # Print all root level object names (aka keys)
    # these can be group or dataset names
    print("Keys: %s" % f.keys())
    # get first object name/key; may or may NOT be a group
    a_group_key = list(f.keys())[0]

    # get the object type for a_group_key: usually group or dataset
    print(type(f[a_group_key]))

    # If a_group_key is a group name,
    # this gets the object names in the group and returns as a list
    data = list(f[a_group_key])
    print(data)
    Iq=np.array(f.get('integrate1d/Iq'))
    q=np.array(f.get('integrate1d/q'))
```

```
Keys: <KeysViewHDF5 ['integrate1d']>
<class 'h5py._hl.group.Group'>
['Iq', 'q']
```

In [5]:

```
plt.subplots()
plt.imshow(Iq,vmin=0,vmax=5,aspect=1/300, extent=(q[0],q[-1],0,Iq.shape[0]-1))
plt.savefig('2d_integrated_XRD_PtBMG_25000frames.png')
```

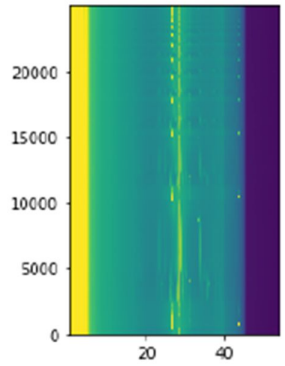

In [6]:

```
def _1gaussian(x_array, amp1,cen1,sigma1):
    return amp1*(1/(sigma1*(np.sqrt(2*np.pi))))*(np.exp((-1.0/2.0)*(((x_array-cen1)/sig
ma1)**2)))
```

In [7]:

```
def baseline_als(y, lam, p, niter=10): #function to obtain the baseline of the spectrum
and improve then the peak fitting
  L = len(y)
  D = sparse.diags([1,-2,1],[0,-1,-2], shape=(L,L-2))
  w = np.ones(L)
  for i in range(niter):
    W = sparse.spdiags(w, 0, L, L)
    #Z = W + lam * D.dot(D.transpose())
    Z = W + lam * np.dot(D,np.transpose(D))
    z = spsolve(Z, w*y)
    w = p * (y > z) + (1-p) * (y < z)
  return z

#There are two parameters: p for asymmetry and λ for smoothness. Both have to be tuned
to the data at hand.
#We found that generally 0.001 ≤ p ≤ 0.1 is a good choice (for a signal with positive p
eaks) and 10^2 ≤ λ ≤ 10^9 ,
#but exceptions may occur. In any case one should vary λ on a grid that is approximatel
y linear for log λ>
```

In [8]:

```
z=baseline_als(Iq[5,:], 1000, 0.1, niter=10)
```

In [9]:

```
plt.figure()
plt.plot(q,Iq[5,:])
x=Iq[5,:]-z

x[x < 0] = 0

plt.plot(q,x) #spectrum with baslane subtracted
plt.xlabel('q (nm^-1)')
plt.ylabel('Intensity')
plt.legend(['Original integrated signal (with amorphous alo)','Signal w/o amorphous al
o'],loc ="upper left")
plt.savefig('XRD_frame5_with_wo_baseline.png')

plt.figure()
plt.plot(q,z)#baseline, amorphous contribution
```

Out[9]:

```
[<matplotlib.lines.Line2D at 0x7fa2c754a160>]
```

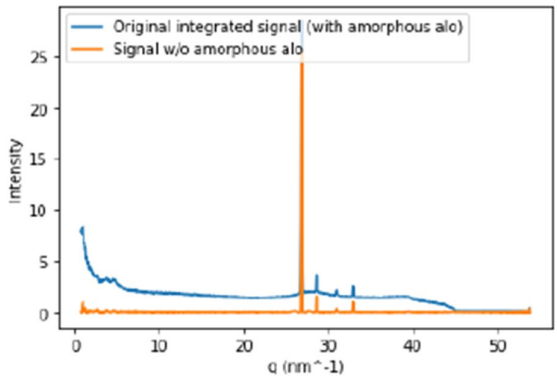

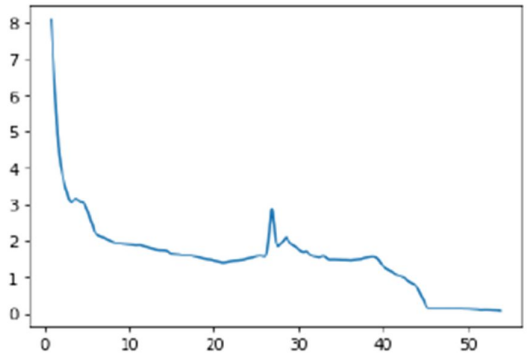

In [10]:

```
#Identify peaks of the first framework with enough signal
max_prominence=np.array(x.max()-x.min())
x_mean=np.array(statistics.mean(x))
peaks, _ = find_peaks(x, prominence=0.4)
q_peaks=q[peaks]
print(x_mean*max_prominence**2/[max_prominence-x_mean**2])
print(q_peaks)
plt.figure()
plt.plot(q,x,'b')
plt.plot(q_peaks,x[peaks], 'xr')
```

```
[1.87382951]
[ 0.90781767  1.25347577 26.83217505 28.56046554 30.92689406 32.94766449
 53.79350673]
```

Out[10]:

```
[<matplotlib.lines.Line2D at 0x7fa2c74c31c0>]
```

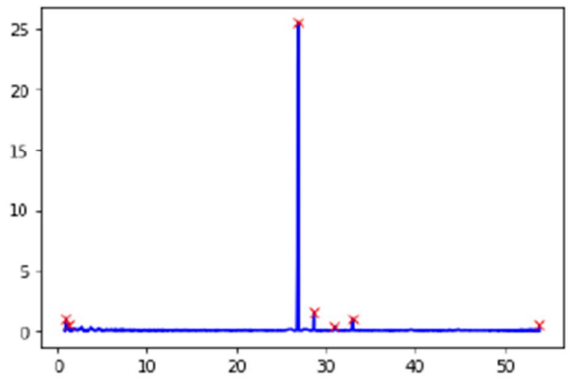

In [15]:

```
# We analise in the following example the peak close to q=32.9 and its shift during fra
mes

# Inital guess to guassian fitting in frame 5
amp1=np.array(0.1,dtype='float64') # the amplitud of the gaussian distribution will be
of the order of 0.1
cen1=np.array(q[peaks[5]],dtype='float64') # the mean position of the peak
sigma1=np.array(0.1,dtype='float64') # a std deviation of 0.1 seems enough for all peak
s

# choosing only the surroundings of the peak
x_array=np.array(q[int(peaks[5])-10:int(peaks[5])+10],dtype='float64')
y_array=np.array(x[int(peaks[5])-10:int(peaks[5])+10],dtype='float64')
```

In [18]:

```
popt_gauss, pcov_gauss = scipy.optimize.curve_fit(_1gaussian, x_array, y_array, p0=[amp
1, cen1, sigma1]) #fitting to gaussian
perr_gauss = np.sqrt(np.diag(pcov_gauss))
print(perr_gauss)
```

```
[0.00131688 0.00057542 0.00057542]
```

In [19]:

```
print(popt_gauss)
amp_peak=popt_gauss[0]
mean_peak=popt_gauss[1]
sigma_peak=popt_gauss[2]
```

```
[ 0.11434192 32.94664066  0.04326845]
```

In [20]:

```
#check good agreement of gaussian fit with experimental signal

x_fit=np.linspace(32.8,33.1, 100)
gauss_fit=_1gaussian(x_fit, amp_peak,mean_peak,sigma_peak)
plt.figure()
plt.plot(q[int(peaks[5])-10:int(peaks[5])+10],x[int(peaks[5])-10:int(peaks[5])+10],'b')
plt.plot(x_fit,_1gaussian(x_fit, amp_peak,mean_peak,sigma_peak), 'xr')
plt.xlabel('q (nm^-1)')
plt.ylabel('Intensity')
plt.legend(['Experimental peak','Gaussian fit'],loc ="upper left")
plt.savefig('peak_fitting_example.png')

print(_1gaussian(mean_peak, amp_peak,mean_peak,sigma_peak))
```

```
1.0542514962000036
```

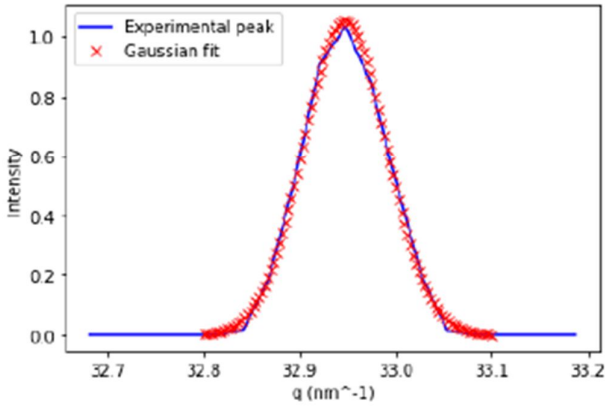

```
# Now we look this peak for the following frames
l=len(Iq[:,0])
print(l)
xx=range(6,l-1,1)


v_peak_position=np.zeros(l)
v_peak_position[5]=mean_peak

v_intensity_peak=np.zeros(l)
v_intensity_peak[5]=_1gaussian(mean_peak, amp_peak,mean_peak,sigma_peak)

v_frame=range(0,l,1)

iteration=1

for ii in xx:
    iteration=iteration+1

    if iteration == 5000 or iteration == 10000 or iteration == 15000 or iteration == 20
000 :
            print(iteration) # it prints some traces to follow the progress of the loop

    #Identify peaks of the following frame
    z=baseline_als(Iq[ii,:], 1000, 0.1, niter=10)
    x=Iq[ii,:]-z
    x[x < 0] = 0

    peaks, _ = find_peaks(x, prominence=0.4)

    q_peaks=q[peaks]


    #look for the peak under study, in this case q=32.9
    #to do so we do the min mean square of the peaks vector of the new frame and the me
an position of the gaussian fit of the
    #previous frame
    if len(peaks) > 1:
        difference=abs(np.array([q_peaks-mean_peak]))

        #select the minimum value as it will be the position of the same peak in the ne
w frame
        jj = np.where(difference == difference.min())

        err_peak=difference.min()

        if  err_peak < 0.1:
            q_peak_new_frame=q_peaks[jj[1]]

            # Inital guess to guassian fitting for the new frame
            amp1=np.array(0.1,dtype='float64')
            cen1=np.array(q[int(peaks[jj[1]])],dtype='float64')
            sigma1=np.array(0.1,dtype='float64')
            # or (i.e. the values of previous gaussian fitting)
            #amp1=amp_peak
            #cen1=mean_peak
            #sigma1=sigma_peak

            # choosing only the surroundings of the peak
            x_array=np.array(q[int(peaks[jj[1]])-10:int(peaks[jj[1]])+10],dtype='float6
4')
```

```
            y_array=np.array(x[int(peaks[jj[1]])-10:int(peaks[jj[1]])+10],dtype='float6
4')

            popt_gauss, pcov_gauss = scipy.optimize.curve_fit(_1gaussian, x_array, y_ar
ray, p0=[amp1, cen1, sigma1])
            perr_gauss = np.sqrt(np.diag(pcov_gauss))


            amp_peak=popt_gauss[0]
            mean_peak=popt_gauss[1]
            sigma_peak=popt_gauss[2]

            v_peak_position[ii]=mean_peak
            v_intensity_peak[ii]=_1gaussian(mean_peak, amp_peak,mean_peak,sigma_peak)
        else: # when the peak selected is far from the one under study we do not consid
er it correct and we skip it
            v_peak_position[ii]=np.nan
            v_intensity_peak[ii]=np.nan
    else:
        err_peak=abs(q_peaks-mean_peak)

        if  err_peak < 0.1:
            q_peak_new_frame=q_peaks

            # Inital guess to guassian fitting for the new frame
            amp1=np.array(0.1,dtype='float64')
            cen1=np.array(q[int(peaks)],dtype='float64')
            sigma1=np.array(0.1,dtype='float64')
            # or (i.e. the values of previous gaussian fitting)
            #amp1=amp_peak
            #cen1=mean_peak
            #sigma1=sigma_peak

            # choosing only the surroundings of the peak
            x_array=np.array(q[int(peaks)-10:int(peaks)+10],dtype='float64')
            y_array=np.array(x[int(peaks)-10:int(peaks)+10],dtype='float64')

            popt_gauss, pcov_gauss = scipy.optimize.curve_fit(_1gaussian, x_array, y_ar
ray, p0=[amp1, cen1, sigma1])
            perr_gauss = np.sqrt(np.diag(pcov_gauss))


            amp_peak=popt_gauss[0]
            mean_peak=popt_gauss[1]
            sigma_peak=popt_gauss[2]

            v_peak_position[ii]=mean_peak
            v_intensity_peak[ii]=_1gaussian(mean_peak, amp_peak,mean_peak,sigma_peak)

        else:
            v_peak_position[ii]=np.nan
            v_intensity_peak[ii]=np.nan


plt.figure()
plt.plot(v_frame,v_peak_position,'b')
```

```
25000


5000
10000
15000
20000
```

Out[21]:

```
[<matplotlib.lines.Line2D at 0x7fa2c7621130>]
```

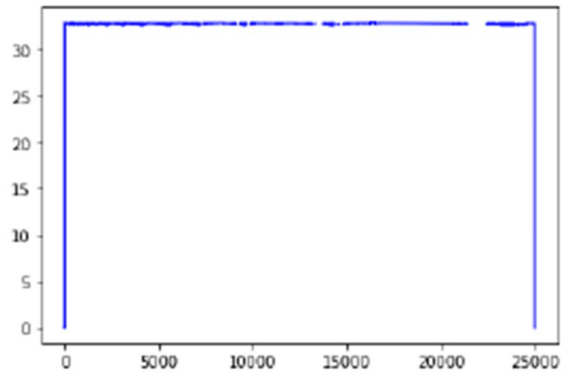

In [22]:

```
file = open('./q_32p9_diff_frames.xlsx', 'w')
file = csv.writer(file)
file.writerow(['Frame', 'q'])
for ii in range(len(v_frame)):
    file.writerow([v_frame[ii],v_peak_position[ii],v_intensity_peak[ii]])

plt.figure()
plt.plot(v_frame,v_peak_position,'b')
plt.ylabel('q (nm^-1)')
plt.xlabel('Frame')

plt.figure()
plt.plot(v_frame,v_intensity_peak,'r')
plt.ylabel('Intensity')
plt.xlabel('Frame')
```

Out[22]:

```
Text(0.5, 0, 'Frame')
```

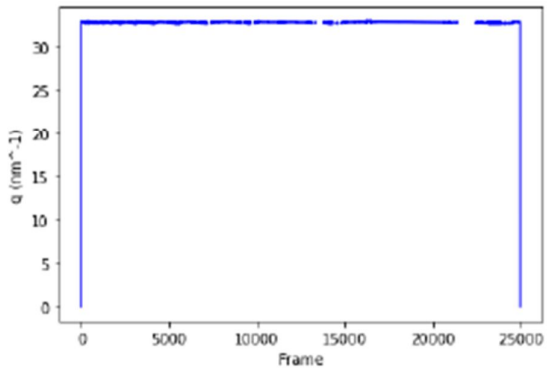

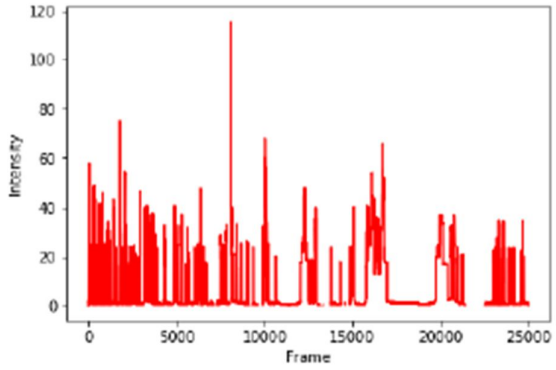

SXRD data analysis and temperature correction (through MATLAB)

```
%% GRAPHS Pt-BMG-CHT
clc;clear all;close all;
% Data of the peaks

v_frame=1:1:25000;
framerate=714;%frames/s
v_time=v_frame/framerate;

data_peak_26p8=readtable('q_26p8_diff_frames.txt');
v_frame1=table2array(data_peak_26p8(:,1));
v_q_peak_26p8=table2array(data_peak_26p8(:,2));
v_intensity_peak_26p8=table2array(data_peak_26p8(:,3));

figure(101)
plot(v_frame,v_q_peak_26p8)
ylabel('q (nm^{-1})')
xlabel('Time')
title('Peak shift around q=26.8')

data_peak_28p5=readtable('q_28p5_diff_frames.txt');
v_q_peak_28p5=table2array(data_peak_28p5(:,2));
v_intensity_peak_28p5=table2array(data_peak_28p5(:,3));

figure(102)
plot(v_frame,v_q_peak_28p5)
ylabel('q (nm^{-1})')
xlabel('Frame')
title('Peak shift around q=28.5')

data_peak_30p9=readtable('q_30p9_diff_frames.txt');
v_q_peak_30p9=table2array(data_peak_30p9(:,2));
v_intensity_peak_30p9=table2array(data_peak_30p9(:,3));

figure(103)
plot(v_frame,v_q_peak_30p9)
ylabel('q (nm^{-1})')
xlabel('Frame')
title('Peak shift around q=30.9')

data_peak_32p9=readtable('q_32p9_diff_frames.txt');
v_q_peak_32p9=table2array(data_peak_32p9(:,2));
v_intensity_peak_32p9=table2array(data_peak_32p9(:,3));

figure(104)
plot(1:1:length(v_q_peak_32p9),v_q_peak_32p9)
ylabel('q (nm^{-1})')
xlabel('Frame')
title('Peak shift around q=32.9')

figure(105)
plot(1:1:length(v_q_peak_32p9),v_q_peak_32p9)
hold on
plot(v_frame,v_q_peak_30p9)
hold on
```

```
plot(v_frame,v_q_peak_28p5)
hold on
plot(v_frame,v_q_peak_26p8)
grid on
ylabel('Wavevector, q')
xlabel('Frame')


%% TEMPERATURE PROFILE FROM THE DSC
%we have 14 cycles in total consisting of: heating + iso2 + cooling + iso2
iso1=1;%first isotherm before the cycles start
iso2=0.1;%isotherm between cooling/heatings
Tmax=700;
Tr=25;
v_HR=[0 0 10 0 -50 0 7.5 0 -50 0 5 0 -50 0 4 0 -50 0 3 0 -50 0 2 0 -50 0 1 0 -50 0↙
...
    0.75 0 -50 0 0.5 0 -50 0 0.4 0 -50 0 0.3 0 -50 0 0.2 0 -50 0 0.1 ...
    0 -50 0 0.05 0 -50 0].*1000;%vector with the sequence of iso Heating/cooling↙
rates
v_time_DSC=zeros(length(v_HR),1);%time at the beginning of eachsegment
v_time_DSC(1:2)=[0,iso1]; %first we have an isotherm before doing the CHT
for ii=3:length(v_HR)
     if v_HR(ii)==0
         v_time_DSC(ii)=v_time_DSC(ii-1)+iso2;
     else
         v_time_DSC(ii)=v_time_DSC(ii-1)+(Tmax-Tr)./abs(v_HR(ii));%heating duration↙
for eachç
     end
end
v_T_DSC=[25 25 700 700 25 25 700 700 25 25 700 700 25 25 700 700 25 25 700 700 25 25↙
700 700 25 25 700 700 25 ...
    25 700 700 25 25 700 700 25 25 700 700 25 25 700 700 25 25 700 700 25 25 ...
    700 700 25 25 700 700 25 25];
figure(201)
plot(v_time_DSC,v_T_DSC)
xlabel('Time (s)')
ylabel('Temperature (°C)')
title('Temperature cycle ex-situ DSC')

% However in the DSC data we see that when we have the Xrays we only start
% to measure heat exchange (peaks or transitions) for reference
% temperatures higher than 300°C. This can be because the photons of the
% synchrotron radiation do not let the sample to cool till the 25°C and
% thus we stay at those 300°C, being the correct temperature cycle in-situ
% those that when the ex-situ is cooling/heating 25-300°C, the in-situ is
% at the isotherm 300°C
v_time_DSC_insitu=zeros(length(v_HR),1);%time at the beginning of eachsegment
v_time_DSC_insitu(1:2)=[0,iso1+(295.21-Tr)/abs(v_HR(3))]; %first we have an isotherm↙
before doing the CHT
for ii=3:length(v_HR)-1

     if v_HR(ii)==0 && v_HR(ii-1)>0
         v_time_DSC_insitu(ii)=v_time_DSC_insitu(ii-1)+iso2;
     elseif v_HR(ii) > 0
```

```
        v_time_DSC_insitu(ii)=v_time_DSC_insitu(ii-1)+(Tmax-295.21)./abs(v_HR↙
(ii));%heating duration for each
    elseif v_HR(ii) < 0
        v_time_DSC_insitu(ii)=v_time_DSC_insitu(ii-1)+(Tmax-295.21)./abs(v_HR↙
(ii));%heating duration for each
    elseif v_HR(ii)==0 && v_HR(ii-1)<0
        v_time_DSC_insitu(ii)=v_time_DSC_insitu(ii-1)+iso2+(295.21-Tr)/abs(v_HR(ii-↙
1))+(295.21-Tr)/abs(v_HR(ii+1));
    end
end
v_T_DSC_insitu=[295.21 295.21 700 700 295.21 295.21 700 700 295.21 295.21 700 700↙
295.21 295.21 700 700 295.21 295.21 700 700 295.21 295.21 700 700 295.21 295.21 700↙
700 295.21 ...
    295.21 700 700 295.21 295.21 700 700 295.21 295.21 700 700 295.21 295.21 700 700↙
295.21 295.21 700 700 295.21 295.21 ...
    700 700 295.21 295.21 700 700 295.21];

figure(202)
plot(v_time_DSC_insitu(1:end-1),v_T_DSC_insitu,'.-.b', 'LineWidth',2)
xlabel('Time (s)')
ylabel('Temperature (°C)')
title('Temperature cycle in-situ DSC')

figure(203)
plot(v_time_DSC_insitu(1:end-1),v_T_DSC_insitu,'.-.b', 'LineWidth',2)
hold on
plot(v_time_DSC,v_T_DSC,'-k')
xlabel('Time (s)')
ylabel('Temperature (°C)')
legend('In-situ','Ex-situ')
title('Temperature cycle ex-, in-situ DSC')



%% TEMPERATURE REFERENCE (FROM PEAK 26.8)

%the real temperature of the sample will be slightly shifted in time
% with respect to the set by the machine due to the exposition time in the detector.
% We know that the temperature cycle start with an isotherm at 25°C during
% 1s (iso1), then a heating at 10000°/s since reaching the 700°C, an iso at 700°C
% during 0.1s (iso2), a cooling at -50000°/s, a new iso2... (see the figure above)
% However due to xray heating the isotherm will be at 296°C and with a
% longer period, i.e. the iso1+(Tr_insitu-Tr)/heatingrate.
iso1=1;
iso2=0.1;
v_heatingrates=[10 7.5 5 4 3 2 1 0.75 0.5 0.4 0.3 0.2 0.1 0.05].*1000;%°/s
coolingrate=50000;%°/s
dt=1/714;
Tmax=700;
Tr=25;
Tr_insitu=295.21;
% To see the shift we can focuse in the start of the cooling ramp in the xrd.
% When the q in the frame range of [290,300] has a value higher than 26.6 we
% consider the start point of the first cooling. Thus the temperature
```

```
% behind it was of 700 during a period of iso, and in from we have the
% cooling ramp of -50000°/s till reaching 25°C
zz=0;
for ii=290:300
    if v_q_peak_26p8(ii) > 26.6 && zz == 0
            frame_coolingstart=v_frame(ii); %identifies the start of the first
cooling

            zz=zz+1; %we will find more data points satisfying the condition after
the cooling starts, so we do not want to store they
    end
end

time_coolingstart_xrd=v_time(frame_coolingstart);

v_T_real=zeros(length(v_frame),1);

%before the first coolingstart, from 700°C
zz=0;
for ii=1:frame_coolingstart

    tx=v_time(ii);

   if tx < ( time_coolingstart_xrd-iso2-(Tmax-Tr_insitu)/v_heatingrates(1) )
       v_T_real(ii)=Tr_insitu;
   end
   if tx < ( time_coolingstart_xrd-iso2 ) && tx >= ( time_coolingstart_xrd-iso2-
(Tmax-Tr_insitu)/v_heatingrates(1) )
       v_T_real(ii) = Tr_insitu + (tx- (time_coolingstart_xrd-iso2-(Tmax-Tr_insitu)
/v_heatingrates(1)) )*v_heatingrates(1);

       if zz==0
       shift_triger=1-( (tx-dt)-(Tr_insitu-Tr)/v_heatingrates(1))
       %shift in time of the XRD measurement with respect the DSC in the first
heating.
       %Where we have substracted the time difference due to the fact that
       %we don't start the heating at 25°c but at 295.21°c
       end
       zz=zz+1;
   end
   if tx <= ( time_coolingstart_xrd ) && tx >= ( time_coolingstart_xrd-iso2 )
       v_T_real(ii)=Tmax;
   end

end


%during first cooling

l_cooling=floor(((Tmax-Tr_insitu)/coolingrate)/dt); %with the dt of the XRD
framerate we have that the coolingstep
%would take 5.712 timesteps, thus we have to truncate. We decide to truncate
%to the lower value because the q measured during 5 and 6th timestep will
%reach the Tr and thus at the 6th we will be in the iso and not cooling
```

```
for ii=frame_coolingstart+1:frame_coolingstart+1+l_cooling
    tx=v_time(ii);
    if Tmax-(tx-time_coolingstart_xrd)*coolingrate > 295
        v_T_real(ii) = Tmax -  (tx-time_coolingstart_xrd)*coolingrate;
    else
        v_T_real(ii) = Tr_insitu;
    end
end

%after the first coolingstart

v_time_extens=(1:26000)./714;
v_T_real_after_COOL1=v_T_real(frame_coolingstart+1+l_cooling:end);
length_cycles_done=0;
for jj=2:length(v_heatingrates)
    HRi=v_heatingrates(jj);
    CR=coolingrate;
    %iso before heating
    v_T_real_after_COOL1( (1:( floor(iso2/dt)+floor((Tr_insitu-Tr)/(dt*HRi)) ) )↙
+length_cycles_done )=Tr_insitu;
    length_cycles_done=length_cycles_done + floor(iso2/dt) +floor((Tr_insitu-Tr)/↙
(dt*HRi));
    %heating
    v_T_real_after_COOL1(1+length_cycles_done:length_cycles_done+floor((Tmax-↙
Tr_insitu)/(dt*HRi)) )=Tr_insitu+(1:floor((Tmax-Tr_insitu)/(dt*HRi)))*dt*HRi;
    length_cycles_done=length_cycles_done + floor((Tmax-Tr_insitu)/(dt*HRi));
    %iso after heating
    v_T_real_after_COOL1( (1:floor(iso2/dt))+length_cycles_done )=Tmax;
    length_cycles_done=length_cycles_done + floor(iso2/dt);
    %cooling
    v_T_real_after_COOL1(1+length_cycles_done:length_cycles_done+floor((Tmax-↙
Tr_insitu)/(dt*CR)))=Tmax-(1:floor((Tmax-Tr_insitu)/(CR*dt)))*dt*CR;
    length_cycles_done=length_cycles_done + floor((Tmax-Tr_insitu)/(dt*CR));

end

v_T_real(frame_coolingstart+1_cooling+(1:length(v_T_real_after_COOL1)))↙
=v_T_real_after_COOL1;

figure(302)
yyaxis left
plot(v_time,v_q_peak_26p8,'-b')
ylabel('Wavevector, q')
xlabel('Time')
ylim([26.5,27])
grid on


yyaxis right
plot(v_time,v_T_real,'-r','LineWidth',1.5)
%hold on
%plot(v_time_DSC-shift_triger,v_T_DSC,'--k')
legend('Wavevector Au <1 1 1>)','Temperature XRD')%,'Temperature program DSC')
ylabel('Temperature(°C)')
```

```
ylim([-20,1100])


figure(303)
yyaxis left
plot(v_time,v_q_peak_26p8,'-b')
ylabel('Wavevector, q')
xlabel('Time')
ylim([26.5,27])
grid on


yyaxis right
plot(v_time_DSC,v_T_DSC,'-r')

legend('Wavevector Pt<111>','Temperature program DSC')
ylabel('Temperature(°C)')
ylim([-20,1100])

%% ANALYSIS OF THE TIME SHIFT
% We will check at each cooling step the difference of time between their
% start in the XRD and the theoretical obtained from the DSC temperature
% sequence

% Let's see the time at which start each cooling in the theoretical
v_starttemp_coolings=[];
v_starttime_coolings=[];
v_index_starttime_coolings=[];


for ii=2:length(v_T_real)
   if v_T_real(ii-1)==700 && v_T_real(ii+1) < 700 && v_T_real(ii)==700
       v_starttime_coolings=[v_starttime_coolings v_time(ii)];
       v_index_starttime_coolings=[v_index_starttime_coolings ii];
       v_starttemp_coolings=[v_starttemp_coolings v_T_real(ii)];
   end
end
figure(401)
plot((1:length(v_T_real))./framerate,v_T_real,'-k')
hold on
plot(v_starttime_coolings,v_starttemp_coolings,'*r')
ylabel('Temperature (°C)')
xlabel('Time (s)')

% Now we do the same for the wavevector. This is more difficult to automise
% due to the noise and the transitions present. We select manually the
% time that start the cooling for each cycle in the wavevector-q plot.
v_starttime_coolings_q=v_time↙
([293,506,753,1024,1338,1726,2357,3143,4260,5603,7356,9901,14840,24567]);
v_startq_coolings_q=v_q_peak_26p8↙
([293,506,753,1024,1338,1726,2357,3143,4260,5603,7356,9901,14840,24567]);
figure(402)
plot(v_time,v_q_peak_26p8,'-k')
hold on
```

```
plot(v_starttime_coolings_q,v_startq_coolings_q,'*r')
xlabel('Time (s)')
ylabel('Temperature (°C)')

% Now let's calculate the time difference:
v_dt_cycles=v_starttime_coolings_q-v_starttime_coolings;
v_cycle=1:14;
figure(403)
plot(v_cycle,v_dt_cycles,'-k')
xlabel('Cooling number')
ylabel('Time shift (q_variation-supposed_T_cycle), °C')



%% THERMAL EXPANSION COEFFICIENTS CALCULATION
q_peak_26p8_T0=26.72;%peak position of <111>Au for the initial temp, T0=300°C
T0=295.21;
%T0=25;
h=6.626e-34;%Plank constant
c=physconst('LightSpeed');%light speed
E=13000*1.602176e-19;%J, XRD photon energy
lambda=(1e9)*h*c/E; %wavelength (nm)

d_hkl_T0=2*pi./q_peak_26p8_T0;
sqrt_hkl=sqrt(1^2+1^2+1^2);%by inspection we agree that this peak correspond to the↙
plane <111> of Pt
%a_111_T0=0.408;%lattice parameter Pt at 25°C
a_111_T0=sqrt_hkl*d_hkl_T0;%lattice parameter in nm at T0=300°C.

v_d_hkl_T=2*pi./v_q_peak_26p8;
v_a_111_T=sqrt_hkl.*v_d_hkl_T;

normalized_lattice_parameter=v_a_111_T./a_111_T0; %a/a0=(1+K*T-T0)

%fitting normalized_lattice_parameter vs v_T_real with curve fitting tool app
T=v_T_real;a_n=normalized_lattice_parameter;
INF_VALUES=isinf(a_n);%identify those values of a_n that are inf
a_n(find(INF_VALUES==1))=[];T(find(INF_VALUES==1))=[];
K0 = 14e-6;

myfittype=fittype('K*(T-T0)+1','dependent','a_n','independent','T',...
    'coefficients',{'K','T0'});
myfit = fit(T,a_n,myfittype,'StartPoint',[K0,T0],'Weight',ones(length(a_n),1))
coefficientValues = coeffvalues(myfit);
K=coefficientValues(1);T0=coefficientValues(2);
figure(501)
plot(T,a_n,'.r')
hold on
plot(T,K.*(T-T0) + 1,'-b')
ylabel('Lattice parameter, 1/q (nm)')
xlabel('Temperature (°C)')
title('Thermal expansion gold chip (peak q=26.8)')
grid on
txt1 = 'K=1.303e-05 K^-1';
```

```
txt2 = 'T_0=296°C';
text(500,1,txt1)
text(500,0.9987,txt2)
legend('Data','Linear Fitting: a/a_0=K(T-T_0) + 1')


%% Derivation of the theoretical Q VARIATION WITH THE THEORETICAL T CYCLE
%(300-700°C) converting it with the thermal expansion coeff above:

T=v_T_real;v_a_fit=a_111_T0.*(1+K.*(T-T0));
v_d_111_fit=v_a_fit./sqrt_hkl;
v_q_111_fit=2*pi./v_d_111_fit;

figure(601)
plot(v_time,v_q_111_fit,'.r')
hold on
plot(v_time,v_q_peak_26p8,'--k')
ylabel('Wavevector q (nm-1)')
xlabel('Time (s)')
legend('Fitted q by therm.coeff','Experimental q')

%% DERIVATION OF THE ACTUAL TEMPERATURE CONVERSING Q TO T WITH THERMAL EXPANSION↙
ABOVE

v_d_hkl_T=2*pi./v_q_peak_26p8;
v_a_norm_111_T=sqrt_hkl.*v_d_hkl_T./a_111_T0;
v_Tref_111_Au=(v_a_norm_111_T-1)./K + T0; %ACTUAL TEMPERATURE OF THE CHIP

figure(502)
plot(v_time,v_Tref_111_Au,'-k')
xlabel('Time (s)')
ylabel('Temperature (°C)')
grid on
title('(actual) Temperature cycle extracted from the Au chip')

%% ANALYSIS OF PEAK INTENSITIES WITH TEMPERATURE-(Calibrated)


figure(801)
yyaxis left
plot(v_time,v_intensity_peak_26p8,'-b')
ylabel('Intensity (counts)')
yyaxis right
plot(v_time,v_T_real,'-r')
hold on
plot(v_frame,v_Tref_111_Au,'.-.r')
ylabel('Temperature (°C)')
title('Intensity of Au<111> peak')
grid on

figure(802)
yyaxis left
plot(v_frame,v_intensity_peak_28p5,'-b')
ylabel('Intensity (counts)')
```

```
yyaxis right
plot(v_frame,v_T_real,'-r')
hold on
plot(v_frame,v_Tref_111_Au,'.-.r')
ylabel('Temperature (°C)')
title('Intensity of Pt<111> peak')
grid on

figure(803)
yyaxis left
plot(v_time,v_intensity_peak_30p9,'-b')
ylabel('Intensity (counts)')
yyaxis right
plot(v_time,v_T_real,'-r')
hold on
plot(v_time,v_Tref_111_Au,'.-.r')
ylabel('Temperature (°C)')
title('Intensity of Au<200> peak')
grid on

figure(804)
yyaxis left
plot(v_time(1:length(v_intensity_peak_32p9)),v_intensity_peak_32p9,'-b')
ylabel('Intensity (counts)')
yyaxis right
plot(v_time(1:length(v_intensity_peak_32p9)),v_T_real(1:length↙
(v_intensity_peak_32p9)),'-r')
hold on
plot(v_time,v_Tref_111_Au,'.-.r')
ylabel('Temperature (°C)')
title('Intensity of Pt<200> peak')
grid on


%% Analysis of appearance/disappearance <111>Pt peak for each heatingrate
%from that one can obtain the crystallisation nose

v_num_frame_appear=↙
[327,528,771,1050,1359,1751,2372,3172,4277,5628,7371,9924,14846];%when cooling
v_Tref_appear=v_Tref_111_Au(v_num_frame_appear);
v_num_frame_disappear=↙
[212,424,665,932,1235,1610,2192,2949,3995,5294,6963,9343,13787];%when heating
v_Tref_disappear=v_Tref_111_Au(v_num_frame_disappear);

v_T_iso_low=[330,340,330,330,330,310,305,305,300,287,290,275,295,300,350];
v_end_frame_iso_low=↙
[193,397,634,893,1171,1515,1999,2699,3615,4823,6339,8387,11878,18861];

v_T_iso_top=[730,720,725,725,730,750,725,760,775,775,780,780,750,760];
v_end_frame_iso_top=↙
[293,506,755,1024,1338,1726,2357,3146,4253,5604,7351,9895,14835,24560];

v_duration_heating=floor(framerate.*(v_T_iso_top-v_T_iso_low(1:end-1)).↙
/v_heatingrates);
```

```
v_duration_cooling=floor(framerate.*(v_T_iso_top-v_T_iso_low(2:end))./coolingrate);

v_trelative_startcooling_appear=(v_num_frame_appear-v_end_frame_iso_top(1:end-1))./framerate;
v_trelative_startheating_disappear=(v_num_frame_disappear(2:end)-v_end_frame_iso_top(1:end-2))./framerate;

figure(901)
semilogx(v_trelative_startcooling_appear,v_Tref_appear,'*r')
hold on
semilogx(v_trelative_startheating_disappear,v_Tref_disappear(2:end),'*b')
grid on
legend('Tx (from cooling)','Tm (from heating)')
ylabel('Temperature (°C)')
xlabel('Time (s)')
title('CHT and CCT Pt-BMG, crystallite Pt<111>')


%% In-situ DSC data
data_dsc_HR_10k=xlsread('^0PtBMG_XENE19_56436_CHT_insitu_HR10k.xlsx');
v_T_HR_10k=data_dsc_HR_10k(:,3);
v_t_HR_10k=data_dsc_HR_10k(:,2);
v_Q_HR_10k=data_dsc_HR_10k(:,4);

data_dsc_HR_7p5k=xlsread('^0PtBMG_XENE19_56436_CHT_insitu_HR7p5k.xlsx');
v_T_HR_7p5k=data_dsc_HR_7p5k(:,3);
v_t_HR_7p5k=data_dsc_HR_7p5k(:,2);
v_Q_HR_7p5k=data_dsc_HR_7p5k(:,4);

data_dsc_HR_5k=xlsread('^0PtBMG_XENE19_56436_CHT_insitu_HR5k.xlsx');
v_T_HR_5k=data_dsc_HR_5k(:,3);
v_t_HR_5k=data_dsc_HR_5k(:,2);
v_Q_HR_5k=data_dsc_HR_5k(:,4);

data_dsc_HR_4k=xlsread('^0PtBMG_XENE19_56436_CHT_insitu_HR4k.xlsx');
v_T_HR_4k=data_dsc_HR_4k(:,3);
v_t_HR_4k=data_dsc_HR_4k(:,2);
v_Q_HR_4k=data_dsc_HR_4k(:,4);

data_dsc_HR_3k=xlsread('^0PtBMG_XENE19_56436_CHT_insitu_HR3k.xlsx');
v_T_HR_3k=data_dsc_HR_3k(:,3);
v_t_HR_3k=data_dsc_HR_3k(:,2);
v_Q_HR_3k=data_dsc_HR_3k(:,4);

data_dsc_HR_2k=xlsread('^0PtBMG_XENE19_56436_CHT_insitu_HR2k.xlsx');
v_T_HR_2k=data_dsc_HR_2k(:,3);
v_t_HR_2k=data_dsc_HR_2k(:,2);
v_Q_HR_2k=data_dsc_HR_2k(:,4);

data_dsc_HR_1k=xlsread('^0PtBMG_XENE19_56436_CHT_insitu_HR1k.xlsx');
v_T_HR_1k=data_dsc_HR_1k(:,3);
v_t_HR_1k=data_dsc_HR_1k(:,2);
v_Q_HR_1k=data_dsc_HR_1k(:,4);
```

```
data_dsc_HR_0p75k=xlsread('^0PtBMG_XENE19_56436_CHT_insitu_HR0p75k.xlsx');
v_T_HR_0p75k=data_dsc_HR_0p75k(:,3);
v_t_HR_0p75k=data_dsc_HR_0p75k(:,2);
v_Q_HR_0p75k=data_dsc_HR_0p75k(:,4);

data_dsc_HR_0p4k=xlsread('^0PtBMG_XENE19_56436_CHT_insitu_HR0p4k.xlsx');
v_T_HR_0p4k=data_dsc_HR_0p4k(:,3);
v_t_HR_0p4k=data_dsc_HR_0p4k(:,2);
v_Q_HR_0p4k=data_dsc_HR_0p4k(:,4);

data_dsc_HR_0p5k=xlsread('^0PtBMG_XENE19_56436_CHT_insitu_HR0p5k.xlsx');
v_T_HR_0p5k=data_dsc_HR_0p5k(:,3);
v_t_HR_0p5k=data_dsc_HR_0p5k(:,2);
v_Q_HR_0p5k=data_dsc_HR_0p5k(:,4);

data_dsc_HR_0p3k=xlsread('^0PtBMG_XENE19_56436_CHT_insitu_HR0p3k.xlsx');
v_T_HR_0p3k=data_dsc_HR_0p3k(:,3);
v_t_HR_0p3k=data_dsc_HR_0p3k(:,2);
v_Q_HR_0p3k=data_dsc_HR_0p3k(:,4);

data_dsc_HR_0p2k=xlsread('^0PtBMG_XENE19_56436_CHT_insitu_HR0p2k.xlsx');
v_T_HR_0p2k=data_dsc_HR_0p2k(:,3);
v_t_HR_0p2k=data_dsc_HR_0p2k(:,2);
v_Q_HR_0p2k=data_dsc_HR_0p2k(:,4);

data_dsc_HR_0p1k=xlsread('^0PtBMG_XENE19_56436_CHT_insitu_HR0p1k.xlsx');
v_T_HR_0p1k=data_dsc_HR_0p1k(:,3);
v_t_HR_0p1k=data_dsc_HR_0p1k(:,2);
v_Q_HR_0p1k=data_dsc_HR_0p1k(:,4);

data_dsc_HR_0p05k=xlsread('^0PtBMG_XENE19_56436_CHT_insitu_HR0p05k.xlsx');
v_T_HR_0p05k=data_dsc_HR_0p05k(:,3);
v_t_HR_0p05k=data_dsc_HR_0p05k(:,2);
v_Q_HR_0p05k=data_dsc_HR_0p05k(:,4);

figure(1001)
plot(v_T_HR_10k,v_Q_HR_10k,'-k','LineWidth',1.5)
hold on
plot(v_T_HR_7p5k,v_Q_HR_7p5k,'-g','LineWidth',1.5)
hold on
plot(v_T_HR_5k,v_Q_HR_5k,'-b','LineWidth',1.5)
hold on
plot(v_T_HR_4k,v_Q_HR_4k,'-r','LineWidth',1.5)
hold on
plot(v_T_HR_3k,v_Q_HR_3k,'-y','LineWidth',1.5)
hold on
plot(v_T_HR_2k,v_Q_HR_2k,'.-.k','LineWidth',1.5)
hold on
plot(v_T_HR_1k,v_Q_HR_1k,'.-.g','LineWidth',1.5)
hold on
plot(v_T_HR_0p75k,v_Q_HR_0p75k,'.-.b','LineWidth',1.5)
hold on
plot(v_T_HR_0p5k,v_Q_HR_0p5k,'.-.r','LineWidth',1.5)
```

```
plot(v_T_HR_0p4k,v_Q_HR_0p4k,'.-.y','LineWidth',1.5)
hold on
plot(v_T_HR_0p3k,v_Q_HR_0p3k,'.k','LineWidth',1.5)
hold on
plot(v_T_HR_0p2k,v_Q_HR_0p2k,'.g','LineWidth',1.5)
hold on
plot(v_T_HR_0p1k,v_Q_HR_0p1k,'.b','LineWidth',1.5)
hold on
plot(v_T_HR_0p05k,v_Q_HR_0p05k,'.r','LineWidth',1.5)
grid on
legend('10k','7.5k','5k','4k','3k','2k','1k','0.75k','0.5k','0.4k','0.3k','0.2↙
k','0.1k','0.05k')
ylabel('Heat (mW) (exo. up)')
xlabel('Temperature (°C)')

data_insitu=xlsread('values_peaks_T_dsc_pt_bmg.xlsx', 'INSITU DSC PARAMETERS');
v_HR_DSC=data_insitu(:,1).*1000; %heating rates, K/s
v_Tx1_DSC=data_insitu(:,3); %starting temp. of first cryst peak, °C
v_Tmax1_DSC=data_insitu(:,4); %temp. of the max. value of first cryst peak, °C
v_Hx1_DSC=data_insitu(:,5).*1e-3; %enthalpy of first cryst peak, x1e-3 mJ
v_Tx2_DSC=data_insitu(:,6); %starting temp. of second cryst peak, °C
v_Tmax2_DSC=data_insitu(:,7); %temp. of the max. value of second cryst peak, °C
v_Hx2_DSC=data_insitu(:,8); %enthalpy of second cryst peak, x1e-3 mJ
v_Tm1_DSC=data_insitu(:,9); %starting temp. of first endothermic peak, °C
v_Tmin1_DSC=data_insitu(:,10); %temp. of the min. value of first endoth peak, °C
v_Tl1_DSC=data_insitu(:,11); %finishing (liquidus) temp. of first endoth peak, °C
v_Hm1_DSC=data_insitu(:,12).*1e-3; %enthalpy of first endoth, peak, x1e-3 mJ
v_Tm2_DSC=data_insitu(:,13); %starting temp. of second endothermic peak, °C
v_Tmin2_DSC=data_insitu(:,14); %temp. of the min. value of second endoth peak, °C
v_Tl2_DSC=data_insitu(:,15); %finishing (liquidus) temp. of second endoth peak, °C
v_Hm2_DSC=data_insitu(:,16); %enthalpy of second endoth, peak, x1e-3 mJ

%with this vectors we now plot the CHT diagram. To do so with the actual
%temperature, the one of the chip, we determine at which time for each
%Heating ramp do we reach in the theoretical cycle the temperature showed
%in the DSC. With this time we can assign the reference temperature.

v_tx1_DSC=zeros(1,length(v_HR_DSC));
v_tmax1_DSC=zeros(1,length(v_HR_DSC));
v_tx2_DSC=zeros(1,length(v_HR_DSC));
v_tmax2_DSC=zeros(1,length(v_HR_DSC));
v_tm1_DSC=zeros(1,length(v_HR_DSC));
v_tmin1_DSC=zeros(1,length(v_HR_DSC));
v_tl1_DSC=zeros(1,length(v_HR_DSC));
v_tm2_DSC=zeros(1,length(v_HR_DSC));
v_tmin2_DSC=zeros(1,length(v_HR_DSC));
v_tl2_DSC=zeros(1,length(v_HR_DSC));

for ii=1:length(v_HR_DSC)
    if ii==1
        v_tx1_DSC(ii)=(v_Tx1_DSC(ii)-25)./v_HR_DSC(ii) ;
        v_tmax1_DSC(ii)=(v_Tmax1_DSC(ii)-25)./v_HR_DSC(ii);
        v_tx2_DSC(ii)=(v_Tx2_DSC(ii)-25)./v_HR_DSC(ii) ;
        v_tmax2_DSC(ii)=(v_Tmax2_DSC(ii)-25)./v_HR_DSC(ii) ;
```

```
        v_tm1_DSC(ii)=(v_Tm1_DSC(ii)-25)./v_HR_DSC(ii);
        v_tmin1_DSC(ii)=(v_Tmin1_DSC(ii)-25)./v_HR_DSC(ii) ;
        v_t11_DSC(ii)=(v_T11_DSC(ii)-25)./v_HR_DSC(ii) ;
        v_tm2_DSC(ii)=(v_Tm2_DSC(ii)-25)./v_HR_DSC(ii) ;
        v_tmin2_DSC(ii)=(v_Tmin2_DSC(ii)-25)./v_HR_DSC(ii) ;
        v_t12_DSC(ii)=(v_T12_DSC(ii)-25)./v_HR_DSC(ii) ;
    else
        v_tx1_DSC(ii)=(v_Tx1_DSC(ii)-25)./v_HR_DSC(ii) + v_dt_cycles(ii-1);
        v_tmax1_DSC(ii)=(v_Tmax1_DSC(ii)-25)./v_HR_DSC(ii) + v_dt_cycles(ii-1);
        v_tx2_DSC(ii)=(v_Tx2_DSC(ii)-25)./v_HR_DSC(ii)+ v_dt_cycles(ii-1);
        v_tmax2_DSC(ii)=(v_Tmax2_DSC(ii)-25)./v_HR_DSC(ii)+ v_dt_cycles(ii-1);
        v_tm1_DSC(ii)=(v_Tm1_DSC(ii)-25)./v_HR_DSC(ii) + v_dt_cycles(ii-1);
        v_tmin1_DSC(ii)=(v_Tmin1_DSC(ii)-25)./v_HR_DSC(ii) + v_dt_cycles(ii-1);
        v_t11_DSC(ii)=(v_T11_DSC(ii)-25)./v_HR_DSC(ii) + v_dt_cycles(ii-1);
        v_tm2_DSC(ii)=(v_Tm2_DSC(ii)-25)./v_HR_DSC(ii)+ v_dt_cycles(ii-1);
        v_tmin2_DSC(ii)=(v_Tmin2_DSC(ii)-25)./v_HR_DSC(ii) + v_dt_cycles(ii-1);
        v_t12_DSC(ii)=(v_T12_DSC(ii)-25)./v_HR_DSC(ii) + v_dt_cycles(ii-1);
    end
end
HR_Tx1_happen=find(isnan(v_tx1_DSC)==0);%vector containing the index of v_HR where↙
the cryst happen
v_num_frame_Tx1_DSC=floor(v_tx1_DSC(HR_Tx1_happen).*framerate);
v_Tx1_ref_DSC=v_Tref_111_Au(v_num_frame_Tx1_DSC);

HR_Tmax1_happen=find(isnan(v_tmax1_DSC)==0);
v_num_frame_Tmax1_DSC=floor(v_tmax1_DSC(HR_Tx1_happen).*framerate);
v_Tmax1_ref_DSC=v_Tref_111_Au(v_num_frame_Tmax1_DSC);

HR_Tx2_happen=find(isnan(v_tx2_DSC)==0);
v_num_frame_Tx2_DSC=floor(v_tx2_DSC(HR_Tx2_happen).*framerate);
v_Tx2_ref_DSC=v_Tref_111_Au(v_num_frame_Tx2_DSC);

HR_Tmax2_happen=find(isnan(v_tmax2_DSC)==0);
v_num_frame_Tmax2_DSC=floor(v_tmax2_DSC(HR_Tmax2_happen).*framerate);
v_Tmax2_ref_DSC=v_Tref_111_Au(v_num_frame_Tmax2_DSC);

HR_Tm1_happen=find(isnan(v_tm1_DSC)==0);
v_num_frame_Tm1_DSC=floor(v_tm1_DSC(HR_Tm1_happen).*framerate);
v_Tm1_ref_DSC=v_Tref_111_Au(v_num_frame_Tm1_DSC);

HR_Tmin1_happen=find(isnan(v_tmin1_DSC)==0);
v_num_frame_Tmin1_DSC=floor(v_tmin1_DSC(HR_Tmin1_happen).*framerate);
v_Tmin1_ref_DSC=v_Tref_111_Au(v_num_frame_Tmin1_DSC);

HR_T11_happen=find(isnan(v_t11_DSC)==0);
v_num_frame_T11_DSC=floor(v_t11_DSC(HR_T11_happen).*framerate);
v_T11_ref_DSC=v_Tref_111_Au(v_num_frame_T11_DSC);

HR_Tm2_happen=find(isnan(v_tm2_DSC)==0);
v_num_frame_Tm2_DSC=floor(v_tm2_DSC(HR_Tm2_happen).*framerate);
v_Tm2_ref_DSC=v_Tref_111_Au(v_num_frame_Tm2_DSC);

HR_Tmin2_happen=find(isnan(v_tmin2_DSC)==0);
v_num_frame_Tmin2_DSC=floor(v_tmin2_DSC(HR_Tmin2_happen).*framerate);
```

```
v_Tmin2_ref_DSC=v_Tref_111_Au(v_num_frame_Tmin2_DSC);

HR_Tl2_happen=find(isnan(v_tl2_DSC)==0);
v_num_frame_Tl2_DSC=floor(v_tl2_DSC(HR_Tl2_happen).*framerate);
v_Tl2_ref_DSC=v_Tref_111_Au(v_num_frame_Tl2_DSC);



figure(1002)
semilogx(v_tx1_DSC(HR_Tx1_happen),v_Tx1_ref_DSC,'<b')
hold on
semilogx(v_tm1_DSC(HR_Tm1_happen),v_Tm1_ref_DSC,'<m')
hold on
semilogx(v_tl1_DSC(HR_Tl1_happen),v_Tl1_ref_DSC,'<r')
hold on
semilogx(v_tm2_DSC(HR_Tm2_happen),v_Tm2_ref_DSC,'^m')
hold on
semilogx(v_tl2_DSC(HR_Tl2_happen),v_Tl2_ref_DSC,'^r')
hold on
semilogx(v_tx2_DSC(HR_Tx2_happen),v_Tx2_ref_DSC,'^b')
grid on
legend('T_x_1','T_m_1','T_l_1','T_m_2','T_l_2','T_x_2')
ylabel('Temperature (°C)')
xlabel('Time (s)')
title('CHT and CCT Pt-BMG')

figure(1003)
semilogx(v_tx2_DSC(HR_Tx2_happen),v_Tx2_ref_DSC,'^b')
hold on
semilogx(v_tm2_DSC(HR_Tm2_happen),v_Tm2_ref_DSC,'^m')
hold on
semilogx(v_trelative_startcooling_appear,v_Tref_appear,'xb')
hold on
semilogx(v_trelative_startheating_disappear,v_Tref_disappear(2:end),'xm')
grid on
legend('Tx (from DSC)','Tm (from DSC)','Tx (from XRD)','Tm (from XRD)')
ylabel('Temperature (°C)')
xlabel('Time (s)')
title('CHT and CCT Pt-BMG, crystallite Pt<111>')
%%
%Activation energy obtention from Kissinger Method: https://doi.org/10.1016/j.↙
polymertesting.2014.08.008
%the slope of the -log(HR/Tmax^2)vs1000/Tmax is -E/R, with E activation
%energy per mole and R the ideal gas constant (8,315 J/K mole)
p_Tmax2_DSC=polyfit(-log(v_heatingrates(1:end-3)'./(v_Tmax2_DSC(1:end-3))),↙
v_Tmax2_DSC(1:end-3),1);
Ea_Tmax2_DSC=-p_Tmax2_DSC(1)*8.315 %Activation energy for first cryst, KJ/mole

p_Tmax1_DSC=polyfit(-log(v_heatingrates(3:7)'./(v_Tmax2_DSC(3:7))),v_Tmax2_DSC(3:7),↙
1);
Ea_Tmax1_DSC=-p_Tmax1_DSC(1)*8.315 %Activation energy for first cryst, KJ/mole

figure(1004)
plot(-log(v_heatingrates(1:end-3)'./(v_Tmax2_DSC(1:end-3))),1000./v_Tmax2_DSC(1:end-↙


3),'-ob')
hold on
plot(-log(v_heatingrates(3:7)'./(v_Tmax1_DSC(3:7))),1000./v_Tmax1_DSC(3:7),'-ob')
grid on
legend('T_x_2','T_x_1')
xlabel('1000/T_{max}')
ylabel('-ln(\Phi/T_{max}^2)')
title('Activation energy for primary crystallization, Insitu')
```